Arterial spin labeling performance in resting-state functional MRI : the effect of scan duration

Corentin Vallée

UNIVERSITÉ DE RENNES 1

THÈSE DE DOCTORAT DE

L'UNIVERSITE DE RENNES 1

ECOLE DOCTORALE N° 601
Mathématiques et Sciences et Technologies de l'Information et de la Communication
Spécialité : Signal, Image, Vision

Par
Corentin Vallée

Arterial spin labeling performance in resting-state functional MRI: the effect of scan duration

Thèse présentée et soutenue à Rennes, le 26/06/2020
Unité de recherche : IRISA

Rapporteurs avant soutenance :

Sophie Achard	Directrice de recherche CNRS	Laboratoire Jean Kuntzmann, Grenoble
Patrícia Figueiredo	Tenured Assistant Professor	Instituto Superior Técnico, Lisboa

Composition du Jury :

Président :	Michel Dojat	Directeur de recherche Inserm	Grenoble-Institut des Neurosciences, Grenoble
Examinateurs :	Sophie Achard	Directrice de recherche CNRS	Laboratoire Jean Kuntzmann, Grenoble
	Patrícia Figueiredo	Tenured Assistant Professor	Instituto Superior Técnico, Lisboa
	Isabelle Corouge	Ingénieure de recherche	Université de Rennes 1, Rennes
Dir. de thèse :	Christian Barillot	Directeur de recherche CNRS	
Co-dir. de thèse :	Pierre Maurel	Maître de conférences Université de Rennes 1	

Acknowledgements

I would like to start by thanking Christian Barillot, Isabelle Corouge and Pierre Maurel for their supervision throughout this period. Their constant availability, support, and kindness have immensely helped me through the ups and downs of the PhD. I will always be thankful for sharing their experiences and advices with me during our animated meetings.
I would like to thank Sophie Achard and Patricia Figueiredo for reading the thesis and reporting on it with insightful remarks. I am also thankful to both of them and Michel Dojat for agreeing to be a part of the jury for the thesis defense. I would like to thank all the jury members again for providing their comments on this work.
I would like to thank Jean-Christophe Ferré and Michel Dojat for their wise feedback during PhD supervision committees.
I would like to thank Elise Bannier and the Neurinfo platform for the help in developing the MRI protocols, and thanks also to the subjects who participated in the study.
I would like to thank Thomas Amand for his help in the organization of the visit in Beijing.
I would like to express my special thanks of gratitude to Pr. Yu for making this visit possible, and his constant support during my stay.
I would also take this opportunity to thank Pr. Sui, Pr. Liu, Pr. Song, Pr. Jiang and their colleagues for their insightful opinions that have helped me identify the scopes for improving my work. Thanks also to Hua Jiaojiao, Han Xinyong, and Dai Rui for making my stay at Beijing a wonderful time.
I would now like to thank Pr. Klein, Pr. Caillau and Florian Brun without whose support motivated me to take up the PhD research.
Thanks also to the members of the Empenn team for making the work and the after-works so enjoyable.
I would finally like to extend a heartfelt thanks and gratitude to Christian Barillot. I would like to dedicate this manuscript to him.

Corentin Vallée

Contents

Résumé

Dans cette section nous proposons un résumé en français du manuscrit. Nous conservons autant que possible la structure du document. Ce travail aborde l'effet de la durée d'acquisition sur les performances de l'arterial spin labeling (ASL) en imagerie par résonance magnétique (MRI) à l'état de repos. Le contexte de ce travail est présenté dans le premier chapitre du manuscrit. Le second chapitre est dédié à l'effet de la durée d'acquisition en resting-state ASL (rsASL), avec une attention toute particulière sur la méthodologie. Le troisième chapitre s'intéresse aux performances du rsASL par rapport à la technique actuelle de référence, le resting-state BOLD (Blood-Oxygen-Level-Dependent). Nous concluons dans le quatrième et dernier chapitre.

Introduction

En imagerie fonctionnelle, l'utilisation du resting-state ASL dans la routine clinique et pour la recherche académique reste limitée par rapport au resting-state BOLD. Cependant, contrairement au BOLD, l'ASL permet de quantifier la perfusion cérébrale. Cette caractéristique de l'ASL pourrait conduire à des applications cliniques importantes à l'échelle du sujet, car l'ASL est de fait une mesure non invasive du débit sanguin cérébral (DSC) : études longitudinales de sujets sains, suivi des maladies avec altération du DSC, etc. Malgré l'implication croissante de tous les acteurs de l'IRM dans l'ASL au cours de la dernière décennie, la question de la durée d'acquisition en rsASL semble n'avoir jamais été abordée dans la littérature, malgré ses fortes conséquences pratiques comme l'implémentation clinique, le maintien de l'état de repos par le sujet et, plus important encore, l'impact de la durée d'acquisition sur l'estimation des réseaux fonctionnels.

Ce manuscrit à trois objectifs principaux. Le premier est de confirmer l'ASL en tant que technique viable pour l'IRM fonctionnelle à l'état de repos. Le deuxième est d'aborder l'effet de la durée d'acquisition sur l'estimation des réseaux fonctionnels. Le troisième est de tester les performances du resting-state ASL par rapport au resting-state BOLD, au regard de l'effet de la durée d'acquisition.

Chapitre I

La section 1 présente un bref contexte historique de l'étude des fonctions cérébrales qui a conduit au siècle dernier au développement rapide de technique d'imagerie fonctionnelle. Nous présentons également dans cette section le concept clé du couplage neurovasculaire. Le couplage neurovasculaire est l'interdépendance biologique qui existe entre l'activité électrique des neurones et le débit sanguin cérébral. Bien que le mécanisme exact du couplage neurovasculaire ne soit pas totalement élucidé, la réponse hémodynamique qui suit une activation neurale a été largement étudiée dans la littérature. Le principal avantage de cette connaissance de la réponse hémodynamique est que la fonction cérébrale peut être explorée non seulement par l'activation neuronale, mais aussi à partir des variations locales du débit sanguin cérébral. Nous terminons cette section en présentant des techniques d'imagerie qui, outre l'IRM, permettent d'étudier la fonction cérébrale, soit par l'activité électrique des neurones, ou bien par la réponse hémodynamique.

La section 2 présente un aperçu des bases de la résonance magnétique nucléaire (RMN). Comme l'IRM est notre technique d'imagerie fonctionnelle d'intérêt, nous présentons comment la RMN conduit à l'IRM. Nous introduisons également dans cette section les techniques d'IRM fonctionnelle, notamment l'IRM dynamique avec injection de produit de contraste (pour la mesure de perfusion cérébrale). Cependant, ce caractère invasif est discutable lorsque l'objectif est d'étudier une cohorte de sujets sains, ou encore dans le cadre d'une étude longitudinale.

La section 3 présente une dernière technique d'IRM fonctionnelle : l'imagerie de perfusion par marquage de spins du sang artériel, l'arterial spin labeling (ASL). Non invasive comme le BOLD, mais permettant la quantification du débit sanguin cérébral contrairement au BOLD, l'ASL est une technique d'IRM prometteuse qui malheureusement souffre d'une exposition limitée hors de la recherche académique.

Nous finissons par présenter avantages et limites de l'ASL en imagerie fonctionnelle, en particulier par rapport à la technique de référence qu'est le BOLD.

La section 4 présente l'IRM fonctionnelle au repos (rsfMRI). Au repos, le cerveau demeure actif : de nombreuses activations spontanées des neurones se produisent. La connectivité fonctionnelle est définie comme la concomitance de ces activations neuronales spontanées. Les zones dédiées à la même fonction montrent une forte connectivité fonctionnelle, comme l'a illustré la toute première expérience d'IRM fonctionnelle à l'état de repos avec l'aire motrice. L'étude de la connectivité fonctionnelle permet de subdiviser le cerveau en petites unités fonctionnellement cohérentes, appelées réseaux fonctionnels, et de montrer comment leur architecture globale a la propriété de graphe petit-monde chez le sujet sain. Dans cette section, nous définissons tout d'abord la connectivité fonctionnelle et présentons l'IRM de repos. Dans un second temps, nous présentons le prétraitement des données de rsfMRI ainsi que différents modèles de connectivité fonctionnelle qui permettent la reconstruction de réseaux fonctionnels. Enfin, nous introduisons brièvement la théorie des graphes, qui est un outil particulièrement adapté à la compréhension de l'organisation fonctionnelle du cerveau. Au-delà de la compréhension des fonctions cérébrales, l'IRMf au repos trouve également des applications cliniques. En effet, la neuropathologie peut affecter la disposition des réseaux fonctionnels et défaire l'organisation petit-monde des réseaux, à l'échelle du graphe. La section consacrée à l'IRM de repos se termine par une discussion qui guidera notre modélisation dans la partie suivante du manuscrit et permettra également de commenter les résultats obtenus.

Chapitre II

La section 5 motive nos premières contributions. La durée d'acquisition est un paramètre pratique essentiel dans une étude rsfMRI. Quelques articles ont déjà étudié directement ou indirectement l'influence de la durée en resting-state BOLD [Anderson et al., 2011; Birn et al., 2013; Bouix et al., 2017; Laumann et al., 2015; Termenon et al., 2016; Van Dijk et al., 2010]. Cependant, à notre connaissance, la question n'a pas encore été abordée en rsASL. Dans la deuxième partie de ce manuscrit, nous abordons donc l'influence de la durée d'acquisition en resting-state ASL. Afin de confirmer la viabilité de l'ASL comme technique d'IRM au repos, nous insistons également sur la faisabilité de la détection des réseaux fonctionnels cérébraux avec l'ASL. La plupart des études actuelles sur le resting-state ASL proposent une durée de 8 à 13 minutes et un TR de 3 à 4 s (soit 120 à 260 volumes). Intuitivement, on pourrait supposer que plus la durée est longue, plus l'échantillonnage de la corrélation des signaux (ou de toute autre mesure sur les signaux) dans le cerveau est bon et donc meilleure est l'acquisition. Toutefois, cela nécessite de définir ce que signifie réellement une "meilleure" acquisition, et cela ne tient pas compte des conditions cliniques et de maintien de l'état de repos du sujet.

La section 6 présente les paramètres d'acquisitions et le prétraitement des données utilisé. Nous nous efforçons de rester aussi proches que possible de ce qu'un chercheur en resting-state ASL pourrait classiquement expérimenter, en mettant en œuvre une séquence ASL habituelle et un prétraitement des données typique. Comme nous voulons

confirmer la faisabilité de l'ASL en tant que technique de rsfMRI, nous nous concentrons sur une étude à l'échelle du sujet.

La section 7 décrit les méthodes utilisées pour détecter les réseaux fonctionnels et modéliser leur évolution en fonction de la durée d'acquisition. Pour la modélisation de la connectivité fonctionnelle, nous nous appuyons sur une analyse de type « seed-based analysis » (SBA) qui facilite la comparaison directe entre les sujets. Afin d'évaluer l'effet de la durée d'acquisition sur la qualité des réseaux détectés par resting-state ASL, nous imitons le comportement d'une inspection visuelle des données. Un investigateur confirmerait qu'un réseau estimé est valide si l'estimation est proche d'une définition consensuelle du réseau attendu. Nous modélisons l'énoncé "proche d'une définition consensuelle" en associant un score au recouvrement entre un réseau fonctionnel estimé et un réseau de référence correspondant, provenant d'un atlas de rsfMRI, l'atlas Multi-Subject Dictionary Learning (MSDL) [Varoquaux et al., 2011]. Nous utilisons la régression locale LOESS pour modéliser l'évolution des scores en fonction de la durée d'acquisition.

La section 8 est axée sur les résultats. Une analyse approfondie du réseau du mode par défaut (DMN) est présentée afin d'illustrer l'évolution des scores sur le réseau le plus typique de la rsfMRI. Pour tous les sujets, l'indice de Jaccard et l'aire sous la courbe (AUC) se stabilisent après une durée d'acquisition similaire, en adéquation avec l'interprétation de l'inspection visuelle. Comme tous les réseaux fonctionnels sont détectés à l'échelle du sujet, nos résultats confirment la faisabilité de L'ASL comme technique de resting-state MRI. En outre, nos résultats montrent une stabilisation de la qualité de l'estimation après un certain nombre de volumes/une certaine durée pour chaque réseau fonctionnel d'intérêt.

La section 9 discute les résultats et conclut ce chapitre du manuscrit. Comme la qualité des réseaux fonctionnels se stabilise après une certaine durée pour toutes les graines (seeds), la durée optimale peut donc être définie par le début de la stabilisation, interprétée comme un compromis entre la mise en œuvre clinique (la durée la plus courte possible) et les meilleures estimations de réseaux (couverte par des durées très longues). En suivant cette proposition, nous pouvons suggérer, pour notre ensemble de paramètres d'acquisition et de prétraitement, un nombre optimal de volumes de 240, correspondant à une durée optimale de 14 min. Comme nous avons utilisé un prétraitement basique, toute méthode qui améliore la détection des réseaux fonctionnels est susceptible de fournir un début de stabilisation plus précoce, c'est-à-dire un nombre de volumes plus faible et une durée optimale plus courte. Notre suggestion de 240 volumes devrait ainsi suffire pour fournir la meilleure estimation possible des réseaux pour la plupart des utilisations de resting-state ASL.

Chapitre III

La section 10 introduit la comparaison entre le resting-state ASL et le resting-state BOLD. Nous soulignons dans cette section quelques considérations méthodologiques avant de passer à la comparaison. Bien que distinctes dans l'approche, les deux techniques d'IRM mesurent indirectement une activation neurale, et ainsi les prétraitements sont presque interchangeables entre les deux modalités. Cependant, en ce qui concerne l'effet de la durée d'acquisition, la question est plus subtile. En effet, comme le signal est traité

numériquement, on ne peut pas simplement faire la comparaison par rapport à une durée : le nombre d'éléments de l'échantillon utilisé pour estimer une carte fonctionnelle n'est pas une durée en minutes, mais correspond en fait au nombre de volumes. Ainsi, en comparant les cartes fonctionnelles par rapport au nombre de volumes, si une carte est meilleure qu'une autre, ce n'est pas parce qu'elle a été estimée avec une taille d'échantillon plus importante.

La section 11 détaille la comparaison entre ASL et BOLD en appliquant tout d'abord aux données resting-state BOLD le cadre d'évaluation que nous avons utilisé pour le resting-state ASL. Première étape, le prétraitement : il est commun entre le resting-state BOLD et le resting-state ASL, mis à part l'étape de soustraction inter-volume propre à l'ASL. Deuxièmement, la seed-based analysis est également directement applicable : nous utilisons les mêmes graines. Troisièmement, la modélisation et les scores ne dépendent pas de la technique d'acquisition utilisée. Par conséquent, dans cette section, les données rsBOLD sont analysées en suivant la même méthodologie que celle proposée pour les données ASL, puis les résultats sont comparés à ceux obtenus en rsASL dans la partie précédente. Dans l'ensemble, la détection des réseaux semble plus facile en BOLD car plus de graines parviennent à fournir des estimations satisfaisantes des réseaux fonctionnels. Les deux scores de recouvrement par rapport aux références MSDL (indice de Jaccard et AUC) sont légèrement meilleurs en BOLD qu'en ASL. Une stabilisation peut également être observée en BOLD. Cependant, la variance intra-sujet et inter-sujets est beaucoup plus importante en BOLD qu'en ASL : les courbes de régression LOESS sont moins corrélées entre les sujets mais surtout moins corrélées entre les scores. Par conséquent, il est plus difficile en BOLD de définir avec précision un début de stabilisation car l'AUC suggère clairement un nombre plus élevé de volumes, quelle que soit la définition de la stabilisation considérée. Si l'on utilise les mêmes considérations qu'en ASL, c'est-à-dire un compromis entre la durée la plus courte possible pour l'implémentation clinique et la plus longue pour garantir avec le plus de certitude possible la stabilisation, la fourchette de valeurs optimales se situe pour le BOLD entre 250 et 290 volumes (contre 240 en ASL).

La section 12 présente des méthodes alternatives pour comparer l'ASL et le BOLD en resting-state, toujours en fonction du nombre de volumes. En effet, dans la section précédente, la comparaison est effectuée par le biais d'un atlas tiers : le MSDL. En étudiant une technique seule, l'impact de l'utilisation d'un atlas est limité, car il a un impact sur la hauteur des scores, mais pas sur le phénomène de stabilisation. Cependant, comme le MSDL dérive de données BOLD, le BOLD est très probablement avantagé. Dans cette section, nous comparons directement les cartes fonctionnelles obtenues par resting-state ASL et resting-state BOLD à travers quatre mesures. Tout d'abord, nous présentons le nombre de voxels actifs. Il s'agit simplement d'une mesure de la taille des réseaux fonctionnels correspondants. Nous montrons que quel que soit le nombre de volumes, les réseaux fonctionnels BOLD sont toujours 2 à 3 fois plus grands que les réseaux fonctionnels ASL correspondants. Ensuite, nous étudions la distribution tissulaire des réseaux fonctionnels estimés. En effet, nos réseaux fonctionnels d'intérêt devraient avoir la plupart de leurs voxels situés dans la matière grise, un peu dans la matière blanche, et aucun dans le liquide céphalorachidien. Malgré la grande différence de taille,

la distribution tissulaire des réseaux fonctionnels estimés est en fait extrêmement homogène entre l'ASL et le BOLD. Peu importe la graine, le sujet, le nombre de volumes, la technique IRM, la distribution tissulaire est pour presque chaque réseau estimé comme suit : 55-60% dans la matière grise, 25-30% dans la matière blanche, 10-15% dans le liquide céphalorachidien. En d'autres termes, étant donné une distribution tissulaire, il n'est pas possible de prédire à quelle technique d'acquisition elle correspond : la distribution tissulaire n'a pas de pouvoir discriminant. Troisièmement, nous étudions la connectivité fonctionnelle intrinsèque des réseaux fonctionnels estimés. Interprétée comme le résultat d'une classification statistique (clustering), on souhaite qu'une estimation d'un réseau fonctionnel, c'est-à-dire d'un cluster, ait une variance intra minimale, c'est-à-dire une connectivité fonctionnelle intrinsèque maximale. Nous montrons que peu importe les graines, les réseaux fonctionnels estimés avec succès ont une bien meilleure connectivité fonctionnelle intrinsèque en rsASL qu'en rsBOLD. Nous terminons la section en étudiant la corrélation spatiale entre l'estimation en rsASL et en rsBOLD. En ce qui concerne le nombre de voxels actifs, nous utilisons les informations préalables pour ne considérer que les graines qui sont capables de détecter efficacement un réseau fonctionnel. Pour chaque graine, la corrélation spatiale se comporte comme la LOESS lui correspondant dans la modélisation précédente : un faible nombre de volumes est associé à une faible corrélation spatiale, et il est intéressant de noter qu'après un nombre de volumes proche de la fourchette où nous avons détecté la stabilité avec le MSDL, la corrélation spatiale entre les cartes fonctionnelles rsASL et rsBOLD atteint ses valeurs les plus élevées et reste stable avec un plus grand nombre de volumes. Cela confirme que l'impact de l'utilisation d'un atlas est extrêmement limité dans l'apparition du phénomène de stabilisation. En effet, on aurait pu objecter que l'estimation des réseaux fonctionnels peut osciller autour de sa référence, et qu'une stabilisation du score ne traduit pas totalement une stabilisation de la disposition spatiale. Cependant, le cas où une estimation de réseau fonctionnel oscille autour d'une référence MSDL par rapport à l'indice de Jaccard, et oscille également autour de la référence par rapport à la AUC est déjà très difficilement réalisable. Avec ces informations auxiliaires, la stabilisation de la corrélation spatiale confirme la stabilisation de l'agencement spatial des réseaux fonctionels en rsASL et en rsBOLD après une certaine durée.

Chapitre IV

La dernière partie du manuscrit synthétise les résultats du travail effectué au cours de cette thèse et propose quelques perspectives. Dans ce manuscrit, nous nous sommes concentrés principalement sur les considérations méthodologiques de cette évaluation. L'IRM fonctionnelle étant un champ de recherche extrêmement vaste, les facteurs qui pourraient affecter le nombre optimal de volumes à utiliser sont nombreux. Heureusement, beaucoup de ces paramètres disposent de leur propre littérature. De plus, nous avons essayé de mettre en place des séquences et des traitements suffisamment généraux de tel sorte que le nombre de volumes que nous proposons couvre presque tous les usages de la rsASL. Les séquences et traitements appliqués sont aussi suffisamment standards afin de montrer que la rsASL est parfaitement viable en tant que technique de rsfMRI. À notre avis, une meilleure compréhension de l'effet de la durée d'acquisition est à chercher du côté de deux paramètres de la séquence : le temps de

répétition (TR) et le délai post-marquage (PLD). Nous souhaiterions en effet fournir une durée optimale d'acquisition en rsASL en minutes, et non en nombre de volumes, notamment pour la mise en œuvre clinique. Comme le temps de répétition lie les deux, il semble que son rôle spécifique soit le sujet naturel de recherche à approfondir. Le PLD peut également jouer un rôle décisif : un PLD plus long favorise une meilleure estimation du débit sanguin cérébral tandis qu'un PLD plus court favorise une meilleure estimation des réseaux fonctionnels. Comme il n'y a pas de meilleure option à choisir entre les deux, nous avons conservé un PLD long car le principal avantage de l'ASL par rapport au BOLD, est la possibilité de quantifier le débit sanguin cérébral. Par conséquent, l'effet du PLD sur le phénomène de stabilisation des réseaux fonctionnels semble extrêmement intéressant à étudier pour le resting-state ASL.

Introduction

Understanding the brain function has been an important area of research for millennia. The recent fast development of neuroscience in the last century, and in particular the emergence of neuroimaging techniques, has opened the field for in vivo investigations of the cerebral activity. In particular, Functional Magnetic Resonance Imaging (fMRI), thanks to its non-invasiveness and good spatial resolution, has been widely used to assess brain function, through two techniques: task-based fMRI and resting-state fMRI. Task-based fMRI confronts the subject to particular stimuli, which are expected to activate a corresponding specific functional area. In resting-state fMRI (rsfMRI), the subject does not perform any task nor is confronted to any stimuli. However, the similarities in the pattern of spontaneous neural activations at rest provide valuable information on brain function and define the functional connectivity of the brain. Indeed, brain regions can be structurally remote yet have strong a strong functional connectivity, forming what is called a functional network. RsfMRI provides a better understanding of the brain function and especially the organization of the brain into functional networks. RsfMRI has also found numerous clinical applications, as healthy subjects and patients show differences in functional connectivity, in common pathologies like Alzheimer's disease, multiple sclerosis and schizophrenia.

In resting-state functional MRI the gold-standard technique is the Blood-Oxygen-Level-Dependent (BOLD) fMRI. However, due to the multifactorial nature of the BOLD signal, its measure of neural activation is indirect and relative. Arterial Spin Labeling (ASL) is an MRI technique which uses magnetically labeled arterial water protons as an endogenous tracer. An inversion pulse labels the inflowing blood and after a delay called post-labeling delay, a labeled image of the volume of interest is acquired. The subtraction of the labeled image from a control image, i.e., non-labeled, reflects the quantity of spins that have perfused the imaged volume, producing what is commonly called a perfusion-weighted (PW) image. The brain perfusion is the biological process that insures the delivery of oxygen and nutrients to the cerebral tissues by means of microcirculation. The

PW map can be used to quantify the cerebral blood flow (CBF) under some assumptions. The quantification of CBF is the main advantage of ASL over BOLD. The absence of injection and the possibility to employ this imaging technique to brain function or basal perfusion is very attractive. This could lead to significant clinical subject scaled application as ASL is a non-invasive measurement of CBF. Even though the principle of ASL were introduced around the same time of BOLD fMRI, resting-state ASL (rsASL) research has a limited exposure in clinical routine and academic research compared to resting-state BOLD (rsBOLD). The main explanation is probably the lower signal-to-noise ratio of ASL compare to BOLD and its harder practical implementation. Despite the increasing involvement of all MRI stakeholders in ASL over the past decade, much still needs to be done to provide standardized implementation and processing. In particular, the question of the acquisition duration in rsASL seems to have never been addressed in the literature despite its strong practical consequences: clinical implementation, resting-state upholding by the subject, and more importantly, the impact of acquisition duration on the estimation of functional networks.

This manuscript has three main objectives. The first one is to confirm ASL as a viable resting-state fMRI technique. The second one is to address the effect of scan duration on the functional networks estimation. The third one is to test rsASL performance against rsBOLD with respect to the scan duration.

Plan

Chapter I – *Context*

Section 1 presents an historical background of investigation of the brain functions that led in the last century to the rapid development of functional imaging. We also present in this section the key concept of the neurovascular coupling and the imaging techniques that, besides MRI, allow the investigation of brain function.

Section 2 presents an overview of the basics in nuclear magnetic resonance (NMR) and how NMR leads to MRI. We also introduce in this section functional MRI techniques, particularly the gold-standard of functional MRI technique: the blood-oxygen-level dependent (BOLD) functional MRI.

Section 3 presents the technique of interest of this manuscript: arterial spin labeling (ASL). Non-invasive as BOLD, but allowing the computation of CBF unlike BOLD, ASL is a promising MRI technique for clinical application.

Section 4 reviews the resting-state functional MRI (rsfMRI). We first define functional connectivity and present preprocessing of rsfMRI data, different modeling of the functional connectivity that allow the reconstruction of functional networks, and lastly, we briefly introduce the graph theory that provides practical insight into the understanding of brain functional organization. This rsfMRI section ends with a discussion of the definitions and methods, that guides our modeling in the following parts of the manuscript and also help to discuss the results afterwards.

Chapter II – *The effect of scan duration in resting-state ASL*

Section 5 motivates our first contributions on the effect of scan duration in resting-state ASL (rsASL) and the feasibility of rsASL.

Section 6 presents material and preprocessing used in the second chapter of the manuscript. We remain as close as what a typical investigator of rsASL might experience, by implementing a usual ASL sequence and typical rsfMRI preprocessing and focusing on a subject-scaled study, as estimating network on a subject is harder than on a group.

Section 7 describes the methods. For the modeling of functional connectivity, we rely on seed-based analysis (SBA). In order to assess a trend in the duration influence on rsASL detected networks quality, we score the overlap between an estimated functional network and a corresponding reference network from an atlas of rsfMRI.

Section 8 focuses on results. After describing the scores used and the modeling of their evolution over time using a LOESS, an in-depth analysis for the Default-Mode Network (DMN) is presented in order to illustrate scores evolution on the most typical resting-state network. For all subjects, scores stabilize after a similar scan duration, in adequation with visual inspection. Finally, we show results for five additional typical functional networks. As all functional networks are detected at a subject scale, our results confirm the feasibility of rsASL. Furthermore, our results show a stabilization after a certain number of volume/duration for every functional network of interest.

Section 9 discusses the results and concludes this part of the manuscript. We suggest 240 volumes / 14 min for rsASL as a sufficient amount of data to obtain stabilized and best estimation of functional networks.

Chapter III – *Resting-state ASL performance compared to resting-state BOLD*

Section 10 introduces the comparison between rsASL and rsBOLD. As rsBOLD technique is the gold-standard for rsfMRI, the performance of rsASL should be compared to rsBOLD. We point out in this section some methodological considerations in the comparison.

Section 11 details the comparison using the methodological framework we used for rsASL. Overall, the detection of networks seems easier in BOLD. Overlap scores are slightly better in BOLD than in ASL. A stabilization stage can also be observed with BOLD. If we use the same considerations as in rsASL that lead to suggest 240 volumes, the range of suggested values for BOLD is between 250 and 290 volumes.

Section 12 presents alternative methods for comparing rsASL and rsBOLD with respect to the number of volumes. In the previous section, the comparison is actually made through a third-party atlas. In this section, we directly compare rsASL and rsBOLD functional maps through four different measures: the number of active voxels, the tissue distribution, the intrinsic functional connectivity and the spatial correlation.

Conclusion

The last part of the manuscript gathers the results of the work done in the manuscript and suggest area for future investigation.

Chapter I.
Context

Section 1. Functional imaging

In this section we introduced an historical background of investigation of the brain functions and the concept of neurovascular coupling that leads in the last century to the rapid development of functional imaging.

1.1 A brief history

Brain depictions could already be found in ancient Egypt, as Figure 1.1 illustrates. Since that age, the brain anatomy secrets have been continuously discovered with the increasing accuracy of tools, procedures and also accuracy of investigators. However, brain functions in the human body have resist the physicians for several millennia. Before the recent fast development of neuroscience in the last century, brain functions were unfortunately discovered through trauma, like aphasia resulting from a head injury already reported in Egyptians papyrus. While eminent thinkers like Aristotle conceived the brain as a blood cooling mechanism, the antic philosopher Alcmeon of Croton (5th century B.C.) made the first ever reported true assumption about brain functions: "*The seat of sensations is in the brain. This contains the governing faculty. All the senses are connected in some way with the brain; consequently, they are incapable of action if the brain is disturbed*" [Gross, 1987]. In order to find a first evidence of Alcmeon hypothesis, we need to wait more than two millennia before Legallois's experiment in 1811. A few years after the discovery of the role of electricity in the nervous system, Legallois's point was to show that a tiny lesion in a specific area in the brain could totally block the respiratory system [Bruce Fye, 1995]. Legallois corollary showed for the first time that a specific cerebral area is used in a specific physiological function. In the end of the same

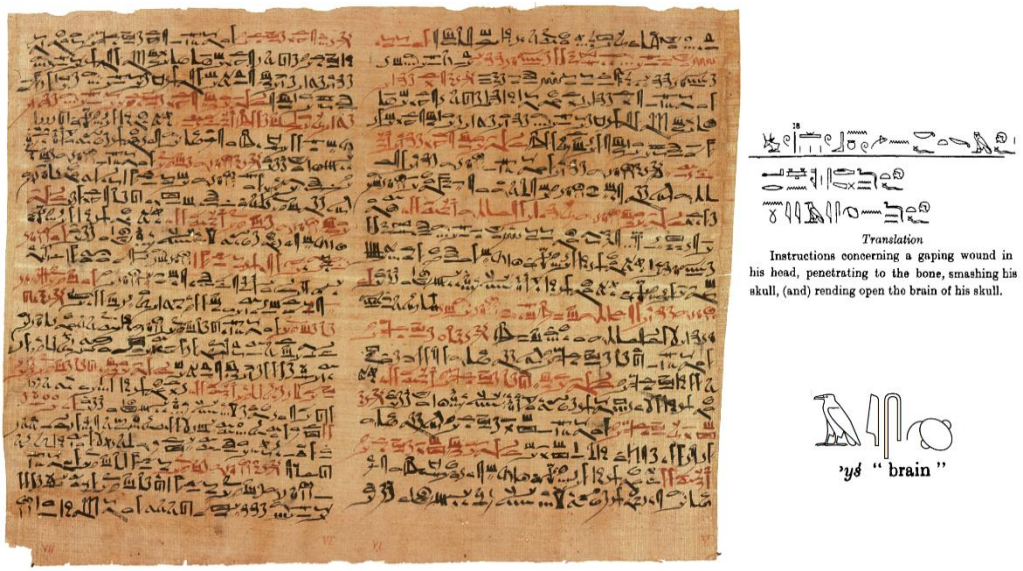

Figure 1.1: The Edwin Smith surgical papyrus (-1700 B.C.) and a partial translation

The partial translation comes from [Breasted, 1930]. As Breasted state, the hieroglyphs evoke "organic substance of a viscous or semifluid consistency". While enigmatic alone, its rare occurrences are most often followed by "of his skull", giving no doubt on his meaning. This is the eldest designation of the brain in mankind history.

century, in 1881, a capital experiment was made by Mosso, who managed to exhibit a link between a cognitive task and variations in blood-flow [Raichle and Shepherd, 2014].

These historical elements give main objectives of functional imaging: measuring cerebral activity, associating areas of the brain with physiological roles, called functions, investigating how these areas interact, through the measurement of the electric activity of the brain or the cerebral blood supply. By extension, functional imaging is also about investigating numerous pathologies since alterations in the brain energy supply or electrical activity can lead to physiological impairment.

1.2 Neurovascular coupling

In the early 20th century, the rapid development of tools to investigate microanatomy (histology), biochemistry and microbiology led to a better understanding of the brain energy supply through blood. However, as soon as in 1890, Roy and Sherrington described a key principle of functional imaging: the *neurovascular coupling* [Roy and Sherrington, 1890]. Neurovascular coupling is the biological interdependence that exists between the neurons electrical activity and the cerebral blood flow (CBF). Figure 1.2 illustrates this relationship. While the relationship between neural activation, local metabolism and CBF increase is factual, the exact underlying mechanism behind the coupling is still an active field of research [Huneau et al., 2015]. Numerous functional imaging techniques benefit from this coupling. Indeed, they can hence infer variations in cerebral activity not only through neuron electrical activity, but also through the investigation of the cerebral hemodynamic variations.

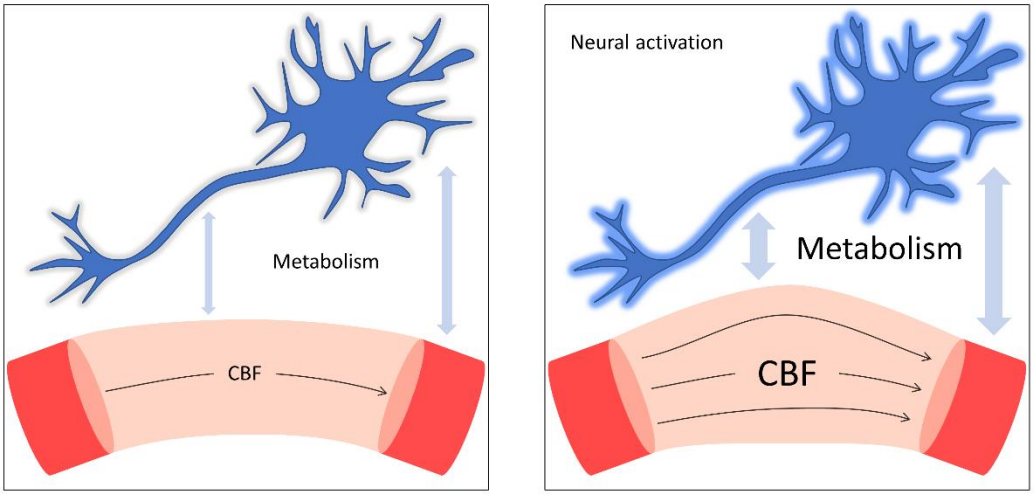

Figure 1.2: Neural activation and neurovascular coupling

When confronted to a stimulation, a neuron releases an electrical signal. The electro-chemical activity of the neurons increases the local metabolism. Since the metabolism is fueled by the blood of the surrounding capillaries, the neuron activation also requires a local increase of the cerebral blood flow.

1.2.1 *Hemodynamic response*

The hemodynamic response function (HRF) represents the expected variation in cerebral blood flow (CBF) as a function of time following a neuronal activation. This standard (canonical) model admits a high variability according to individuals, spots/stimuli and sequences, see [Aguirre et al., 1998; Silvestre et al., 2010] for advanced modeling of the HRF. Figure 1.3 shows a generic model of the hemodynamic response. The initial dip detected by Buxton [Buxton, 2001], that occurs within the first two seconds after the stimulus is generally ignored in models [Poldrack et al., 2011]. Its negative intensity is low compared to the maximum hemodynamic response, so it is rarely observed in practice.

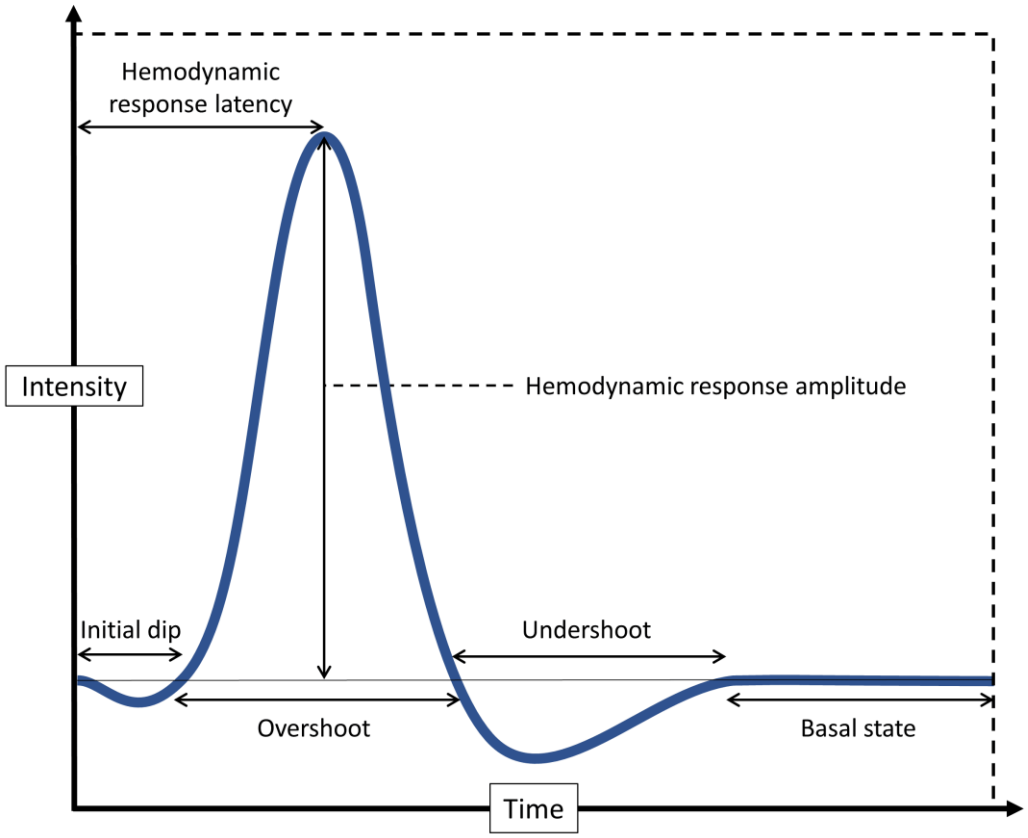

Figure 1.3: Canonical shape of the hemodynamic response function

Abscissa unit is arbitrary. After a neural activation, it takes approximatively twenty seconds before the comeback of the basal state.

1.2.2 Linear time invariant property

An important assumed property of the hemodynamic response is its linear relationship with the neural activation. This assumption is called the linear time invariant (LTI), and greatly simplifies the modeling and interpretation of neuroimaging investigation. Overall, the LTI assumption appears to be fairly accurate in most cases [Dale and Buckner, 1997; Logothetis et al., 2001]. It shows some limitations when the subject is stressed by the stimuli, i.e. when stimuli frequency becomes too high [Wager et al., 2005]. In this case, neural responses can saturate, while the cerebral blood flow keeps increasing [Sheth et al., 2004]. On the opposite, too short and/or too small neural activations are not associated with a CBF increase [Sheth et al., 2004]. The stimuli type can also thwart the linearity, like auditive stimuli [Harms and Melcher, 2002]. Nonetheless, the range of investigations where the LTI is satisfied is wide. Figure 1.4 illustrates the LTI property.

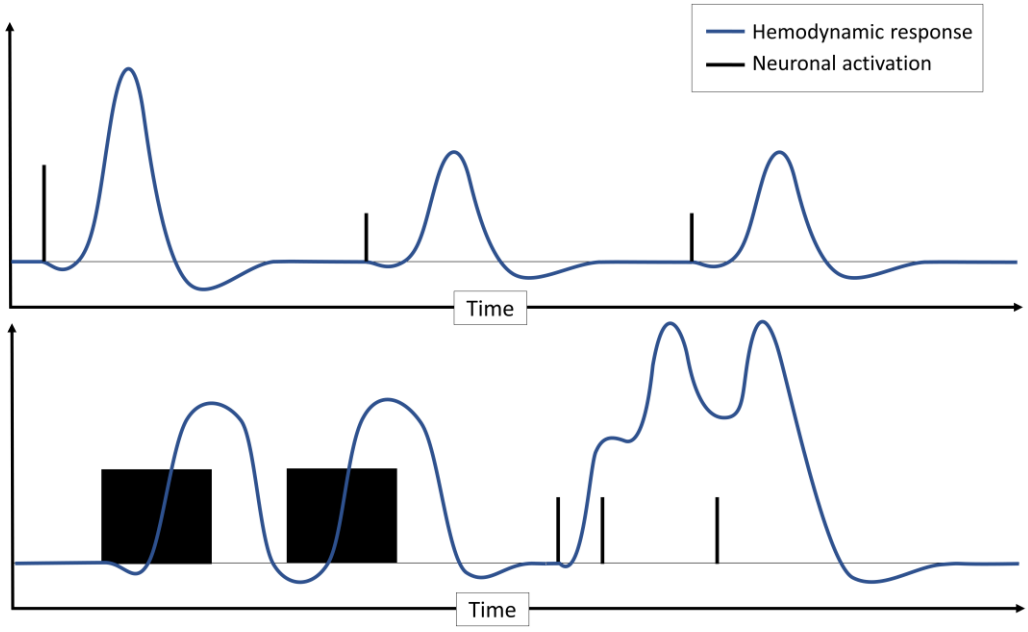

Figure 1.4: Illustration of the linear time invariant property of the HRF

The top graph shows how the HRF amplitude depends linearly on the neuron activation intensity: halving the activation intensity also halves the hemodynamic response, and two identic activations produced two identic responses (from basal state). The bottom graph shows more sophisticated neuronal activations and their associated responses. Since we assume the linearity, the expected HRF is simply the convolution between the canonical HRF and the function that describe the neural activation with respect to time. This computation is the core of task-based functional MRI, which is addressed in section 2.3.

1.3 Imaging techniques

In this section, we briefly describe some common functional imaging techniques. Thanks to the neurovascular coupling, these techniques can measure directly or indirectly either the electrical activity of the neurons or associated hemodynamic response parameters.

1.3.1 Electroencephalography (EEG)

The communication between the brain neurons is made through synapses with electro-chemical reactions. One of the most natural way to investigate brain activity is to measure this electrical activity. EEG uses electrodes placed on the patient scalp to record the variation in voltage between these electrodes resulting from the chemical reaction between synapses [Henry, 2006]. Compared to other brain imaging techniques, EEG is one of the cheapest, easiest to implement and less invasive methods (apart from its intracranial counterpart), which perfectly suits the study of large cohort of healthy (or not) subjects. Furthermore, EEG has one of the best temporal resolution with the order of the millisecond. The major EEG downside is its poor spatial resolution which does not allow an accurate localization of the brain functional activity. However, the increasing development of multimodal brain imaging allows to use EEG in combination with a more spatially accurate method, typically MRI, to overcome EEG poor spatial source localization [Abreu et al., 2018; Bießmann et al., 2011]

1.3.2 Magnetoencephalography (MEG)

Magnetoencephalography is the magnetic equivalent of the EEG: instead of recording voltages, it uses magnetometers to record the magnetic field induced by the brain electric activity [Hämäläinen et al., 1993]. MEG and EEG are similar regarding their imaging properties. MEG is can also be used in combination with other brain imaging technique, and often with EEG as recording both at the same time is quite straightforward [Lopes da Silva, 2013].

1.3.3 Near-infrared spectroscopy (NIRS)

Widely use in chemistry to identify organic molecules, NIRS assess brain activity by recording optical transmittance variation caused by the variation in blood hemoglobin concentration, in the near-infrared spectrum. Indeed, a neural activation requires energy which is drawn from the oxygen stored in the blood hemoglobin, locally modifying its concentration [Butler et al., 2017]. As EEG, NIRS is cheap and non-invasive. However, NIRS records indirectly the brain activity and only through the cortical surface, which hinders its interpretation.

1.3.4 Positron emission tomography (PET)

We briefly mentioned in the NIRS section that a neural activation requires chemical energy, which is brought to the neurons through the vascular system. Hence, tracing this chemical supply would provide direct exhibition of the neural activity, which is the exact concept of PET. PET consists in injecting a radioactive component, like ^{15}O (called radiotracer), and investigating its spreading and accumulation in the brain by tracing its radioactivity with a gamma camera [Vaquero and Kinahan, 2015]. The major advantage of PET is that it allows to quantify the cerebral blood flow, depending on the radiotracer

used. As neural activity is directly related to the oxygen consumption, and oxygen consumption to cerebral blood flow (cf. neurovascular coupling in section 1.2), PET scan allows a quantitative measurement of the neural activity as well as the investigation of disease that have an impairment of cerebral blood flow as biomarker, such as Alzheimer's disease [Marcus et al., 2014]. PET major limitation is the injection of radioactive components, which usage is arguable when investigating healthy subjects.

1.3.5 Computed tomography (CT)

The CT cast series of X-rays on the subject in different direction. Since each organic component has its own level of X-ray absorption, and also because the body absorption is not high enough to totally cancel the penetrating ability of X-rays, CT is able to rebuild the head as a three-dimensional volume and also differentiating tissues inside it [Ter-Pogossian, 1984]. In order to quantify perfusion, an intravenous contrast agent with known pharmacokinetic is injected to the subjects. The high contrast of CT, its faster and less constraining implementation compared to MRI, has made the technique of choice in emergency case and for pathologies related to head trauma However, CT has a major downside. The X-rays are energetic enough to interfere with molecular structure, and are prone to increase the risk of cancer. Consequently, CT is not suitable for longitudinal studies, especially for research purpose on healthy subjects where the benefits of examination are highly arguable.

Note that even though computed tomography usually refers to specifically X-rays, tomography is actually every technique that (re-)build a three-dimensional volume from a sample of two-dimensional sections. For instance, MRI can somehow be understood as a nuclear magnetic resonance tomography. Functional MRI is detailed in next chapter.

Section 2. Functional magnetic resonance imaging

The phenomenon of nuclear magnetic resonance has been discovered simultaneously in 1946 by the respective teams of F. Bloch's in Stanford and E. Purcell at Harvard, and both were awarded the Nobel Prize in 1952. Currently, the phenomenon is mainly known for its use in the medical field as magnetic resonance imaging (MRI). Beside the detection of structural brain abnormalities such as tumors or lesions, the MRI saw in the 1990s the development of a new application, so-called functional MRI (fMRI).

2.1 Introduction to Nuclear Magnetic Resonance

This section overviews the basic principle of nuclear magnetic resonance imaging (NMR) that allows imaging to be made.

2.1.1 Quantum model

The human body consists of roughly two third of hydrogen atoms $^1\mathrm{H}$. In NMR, we usually assimilate the proton $^1\mathrm{H}^+$ with the hydrogen atom. A proton is a positively charged elementary particle that rotates on itself along a free axis, whose guiding vector $\vec{S}$ represents the spin of the particle.

Let us give a strong magnetic field $\vec{\mathrm{B}}_0$ of the order of several Tesla: 0.5T to 22T in general, less than 11.5T for the medical environment (4.10^{-5}T for the earth magnetic field as a comparison). Let this field be oriented according to Oz, in the canonical coordinate system of $\mathbb{R}^3$, without any loss of generality. The protons spins evolving in this magnetic field will align on $\vec{\mathrm{B}}_0$, either in parallel or in antiparallel direction. The quantum mechanics guarantees that there will always be slightly more protons in the same direction as $\vec{\mathrm{B}}_0$, around two parts-per-million in standard condition for temperature and pressure for 0.5T field. This may seem like a small amount, but as a reminder, one gram of hydrogen (i.e. one gram of proton) represents one mole of hydrogen, i.e. 6.02×10^{23} atoms. This difference of "excess" protons induces a macroscopic magnetization of the protons represented by a vector $\vec{\mathrm{M}} = \vec{\mathrm{M}}_{z_0}$ along the Oz axis. For a family of N protons indexed by i we have:

- Without $\vec{\mathrm{B}}_0$: $\sum_{i=1}^{\mathrm{N}} \vec{\mathrm{S}}_i = \vec{0}$
- Under $\vec{\mathrm{B}}_0$: $\left(\forall i \leq \mathrm{N}, \vec{\mathrm{S}}_i = \pm\vec{\mathrm{S}}\right) : \sum_{i=1}^{N} \vec{\mathrm{S}}_i \cong \frac{\mathrm{N}}{2}.\vec{\mathrm{S}} - \frac{\mathrm{N}}{2}.\vec{\mathrm{S}} + 2.10^{-6}.\mathrm{N}.\vec{\mathrm{S}} = \vec{\mathrm{M}}_{z_0}$

2.1.2 Electromagnetic pulse

Precession

So far, we have considered the protons spins as perfectly aligned with the field $\vec{\mathrm{B}}_0$. In fact, this is not exactly true, the axis carried by every spin $\vec{\mathrm{S}}_i$ rotates around $\vec{\mathrm{B}}_0$ at a fixed angle with a frequency ω_0. This phenomenon is called the precession. This is exactly the exact same phenomenon that can be observed when disturbing the rotation of a spinning top. The proton revolves around $\vec{\mathrm{S}}_i$ and $\vec{\mathrm{S}}_i$ revolves around $\vec{\mathrm{B}}_0$.

Resonance

A new field $\vec{\mathrm{B}}_1$, orthogonal to $\vec{\mathrm{B}}_0$ and called a radio-frequency pulse (RF), is applied. It rotates in the xOy plane, at a frequency ω. When the frequency ω reaches ω_0, called in

this context Larmor frequency, the field $\vec{B}_1$ resonates with the precession of the protons. This field will force the protons to orient themselves in antiparallel with $\vec{B}_0$. The protons perform this movement with the same phase, which will gradually make the longitudinal component $\vec{M}_z$ disappear in favour of a transverse component $\vec{M}_{xy}$. When half of the "excess" protons have turned around, the longitudinal component has disappeared, and $\|\vec{M}_{xy}\|$ is maximum (90° RF Pulse). If the RF wave continues to be applied, all the spins in excess are turned around, $\|\vec{M}_{xy}\| = 0$ and $\vec{M}_z = -\vec{M}_{z_0}$ (180° RF pulse).

Relaxation

The state of the protons spin caused by the field $\vec{B}_1$ is unstable, hence when the RF pulse stops, the protons tend to return to the initial state, without a transverse component $\|\vec{M}_{xy}\|$ and with: $\vec{M} = \vec{M}_z = \vec{M}_{z_0}$. For an RF pulse of 90°, two characteristic times will interest us:

- T1 characterizing the longitudinal relaxation, when $\|\vec{M}_z\| = \frac{63}{100}\|\vec{M}_{z_0}\|$
- T2 characterizing the transversal relaxation, when $\|\vec{M}_{xy}\| = \frac{37}{100}\|\vec{M}_{xy_0}\|$

For each hydrogen atom, its proton spin relaxation is impacted by the neighborhood molecular layout. Indeed, constraining structures (like in solids, e.g. bones) or extremely unrestrictive composition (like in free water, e.g. CSF) will be prone to increase the longitudinal relaxation T1 a lot. On the opposite, in-between structure like fat or white matter will foster shorter T1.

2.1.3 Acquisition and contrast weighting

Proton Density

A critical organic tissue property is its own hydrogen atoms density ρ. Indeed, different density ρ imply different number of spins in excess for the region considered. On a mesoscopic scale, this means that each tissue under $\vec{B}_0$ has its own magnetization vector $\vec{M}_{z_0}$ according to its density ρ. Hence, the density ρ has also a discriminative power.

Repetition time

Over time, the excitation/relaxation phases are sequenced according to a certain period, called the repetition time (TR). With a short TR, protons in tissues with a longer longitudinal relaxation time T1 will not have enough time to relax to their initial position. Consequently, every measurement of this tissue will provide a weaker signal. By corollary, protons in shorter T1 regions will be able to get a higher transversal magnetization with the next excitation, thus providing a higher signal.

Spin echo

As the field $\vec{B}_0$ is considered fixed, so are its intrinsic inhomogeneities. Because of these magnetic flaws, the spins will have different precession frequencies. As soon as in 1950, Hahn described the phenomenon of spin echo which allow to cope with magnetic field inhomogeneities [Hahn, 1950] by simply using a 180° RF pulse after the orthogonal excitation. Figure 2.1 below shows the process of spin echo, and its parameter the echo time (TE).

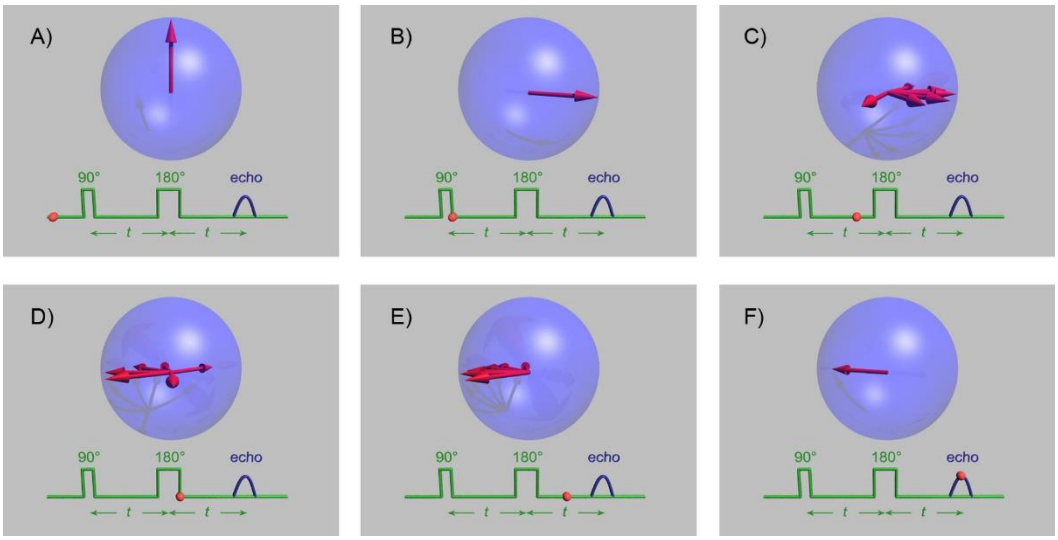

Figure 2.1: Spin echo

A. The spins are first aligned in $\vec{B}_0$
B. The 90° RF pulse aligns spins in the xOy plane
C. Because of the field inhomogeneities, spins precess with different speeds.
D. After a duration t, a 180° pulse is applied, reversing the spins order
E. Because the slower spins are now the first, the fastest ones catch them up
F. After a duration $2t$, called echo time, spins are realigned in the xOy plane.

Image from Wikipedia: https://en.wikipedia.org/wiki/Spin_echo

Contrast

The choice of TR and TE directly influences the acquisition by the operator, this is called weighting. There are three principal types of weights:

- Short TR (~500ms) and short TE (~20ms): this is the T1 weighting
- Long TR (~2000ms) and long TE (~120ms): this is the T2 weighting
- Long TR (~2000ms) and short TE (~20ms): this is the ρ weighting

Each weighting modifies the contrasts of the brain components, a summary of which is provided in the following Table 2.1 and illustrated in Figure 2.2

	T1 weighting	T2 weighting	ρ weighting
White matter	White	Dark grey	Dark grey
Grey matter	Grey	Light grey	Light grey
Cerebrospinal fluid	Black	White	Darker grey
Contrast	WM>GM>CSF	CSF>GM>WM	GM>WM>CSF

Table 2.1 Contrast of T1, T2, ρ weighting

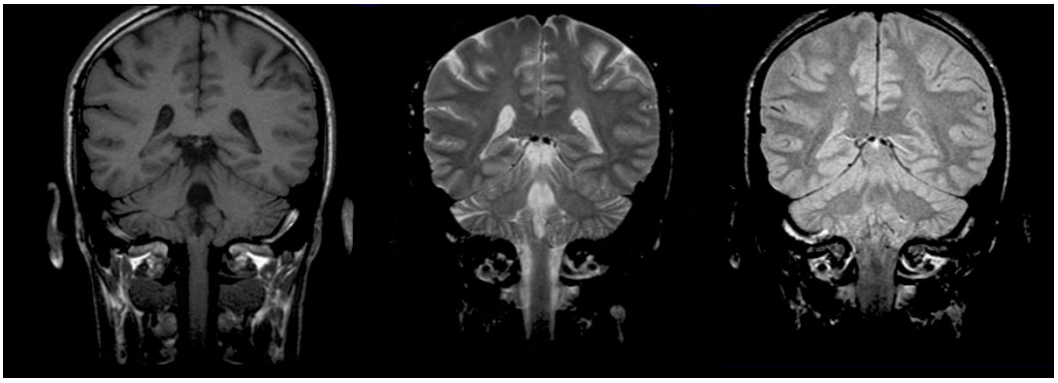

Figure 2.2: Illustration of the T1, T2 and ρ weighting

2.2 Functional MRI techniques

In this section, we present three of the four main fMRI techniques. The fourth we will introduce is Arterial Spin Labeling (ASL). Since ASL is the core technique of this manuscript, it has its own dedicated chapter afterwards.

2.2.1 Dynamic susceptibility contrast imaging (DSC MRI)

DSC MRI relies on a gadolinium based chelate injected in the subject blood stream. Since the gadolinium compound is paramagnetic, its spreading through the vasculature causes local drops of the signal in T2 (and T2*) weighting with respect to its concentration. Thanks to the kinetic of the gadolinium contrast agent, DSC MRI unlocks the computation of the cerebral blood volume and cerebral blood flow [Østergaard, 2005]. DSC MRI has benefited from a long-time investment of MRI stakeholders, and is currently widely available and easy to use for clinical investigation of the brain perfusion. Less invasive than PET scan, DSC may struggle to compute CBF accurately close to physiological artifact, whether they are pathological or not [Essig et al., 2013]. Note that DSC MRI is the eldest published functional MRI technique [Belliveau et al., 1991].

2.2.2 Dynamic contrast-enhanced MR perfusion (DCE MRI)

Very similar to DSC MRI, DCE MRI also uses gadolinium chelate as contrast agent. However, it uses T1 contrast instead of T2 weighting. In this way DCE MRI can access to some of the microvasculature structure properties like the blood-brain barrier and the vessel permeability. These fine measures of the local perfusion make DCE MRI very effective in the investigation of tumors [Gordon et al., 2014]. Principal downside, DCE MRI implementation and modeling is complex compared to DSC MRI.

2.2.3 Blood-oxygen-level dependent functional MRI

Neural activation leads to a strong local increase in blood flow and an increase in oxygen consumption as discussed in section 1.2. However, the increase in cerebral blood flow is proportionally much higher than the increase in oxygen consumption. The local concentrations of the competing molecules of oxyhemoglobin and deoxyhemoglobin are therefore unbalanced in favor of the oxyhemoglobin. When deprived of its oxygen atoms, hemoglobin possesses "free" iron atoms, whose paramagnetic properties locally induce an increase in the signal (for T2* weighting) due to their decreasing number. It is this small variation (roughly 4% in explained variance) in the signal caused by the disruption of balance that BOLD fMRI tries to capture [Kim and Ugurbil, 1997]. By nature, BOLD fMRI shows its major advantage: it is non-invasive. By allowing therefore the longitudinal investigation of large cohorts of healthy subjects, BOLD fMRI has become and remains the gold-standard for functional MRI. Note that the first human BOLD fMRI experiment was reported just one year after DSC MRI [Ogawa et al., 1992]. However, BOLD fMRI shows an important downside. Indeed, the signal variation captured by BOLD fMRI is multifactorial: it relies on the interaction between the local oxygen concentration, the cerebral blood flow and the cerebral blood volume. Consequently, BOLD fMRI does not report directly the cerebral activity, nor does it allow the computation of the brain perfusion.

2.3 Application: task-based functional MRI

Thanks to the neurovascular coupling, MRI is able to assess neural activity through the hemodynamic response. In the first chapter, we introduced the association between area of the brain and function as one of the functional imaging problematics. In task-based fMRI, the subject is confronted to particular stimuli and/or asked to perform particular tasks, which are called the paradigm in this context. Each stimulus is expected to activate a (or some) corresponding functional area to its nature. For instance, a common task is when the subject is asked to tap a finger from his right hand. In this case, a neural activation in area associated with motor function is expected.

2.3.1 Defining a functional area

Thanks to the linear time invariant property (section 1.3), the variation in signal induced by the stimuli is a priori known, as it is illustrated in Figure 2.3. In order to locate the area of neural activation, task-based fMRI usually models the signal in each voxel as a linear combination of the expected activation signal plus some signals of interference [Poldrack et al., 2011]. By regression, if the linear component associated with the paradigm explains a statistically significant part of the signal variance in the voxel, then the voxel can be assumed to be located in the cerebral area which manage the function corresponding to the paradigm. Note that numerous models have been developed from and beside the widely used linear regression. However, they all involve the expected signal at some point, either to define or to identify the functional area that the paradigm tries to detect.

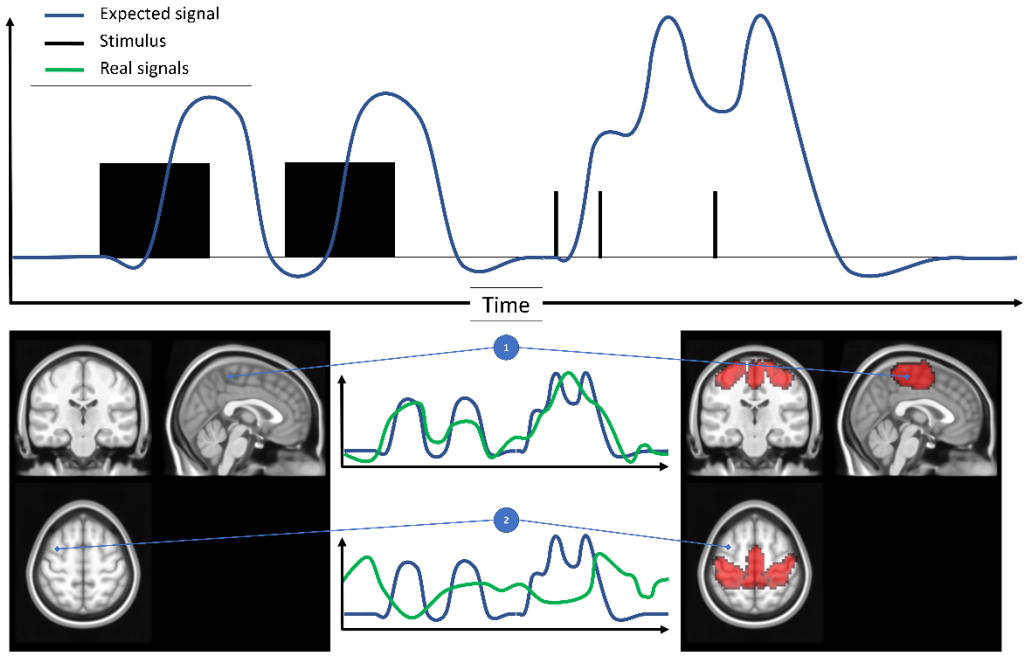

Figure 2.3: Task-based MRI principle – Illustration with motor area

A subject is exposed to motor stimulus following the black pattern shown in top graph. Thanks to the LTI property, the expected signal in blue is computed from the convolution between the paradigm and canonical HRF. In case 1, the voxel signal in green matches well with the expected signal. It will be considered as belonging to the motor area (in red), unlike the voxel in case 2.

Section 3. Arterial Spin Labeling

Introduced in 1992 [Detre et al., 1992], Arterial spin labeling (ASL) is the technique of interest of this manuscript. Instead of injecting a radioactive tracer as PET, ASL uses magnetically labelled protons of blood water as an endogenous contrast agent. In this section, we detail some technical aspect on ASL image acquisition and also the cerebral blood flow quantification.

3.1 General principle and declinations of ASL

Arterial Spin Labeling is an MRI perfusion technique which uses magnetically labeled arterial water protons as an endogenous tracer. An inversion pulse labels the inflowing blood and after a certain delay, a labeled image of the volume of interest is acquired. The subtraction of the labeled image from a control image, i.e., non-labeled, reflects the quantity of spins that have perfused the imaged volume, producing what is commonly called a perfusion-weighted (PW) image. The PW map can be used to quantify the cerebral blood flow (CBF) under some assumptions [Borogovac and Asllani, 2012; Wang et al., 2012]. Figure 3.1 illustrates these steps in a general framework of an ASL image acquisition. The construction of a label lasts the same duration as the construction of a control, which is called the repetition time (TR)[1]. The label and control steps are repeated in order to get numerous PW maps. Depending on the MRI field of investigation, there is two options on how to use the PW maps. On the one hand, one can build an average of the PW maps, which is the topic of *basal* ASL. As basal ASL builds the average perfusion of the brain map, it focuses more on detection of CBF abnormalities. On the other hand, PW maps can be left as they are, and the investigation can focus on the evolution over time. This declination of ASL, our topic of interest, is called *functional* ASL. The next sections describe technical aspects of ASL. Functional ASL (fASL), and more generally functional MRI, is also split into two research fields: task-based as we see in in section 3.3. The other research field, resting-state fMRI, is addressed in next section Section 4.

[1] Some authors consider the TR as the duration of a label *plus* a control. The description of the sequence parameters is almost always self-explanatory about how TR is defined by authors.

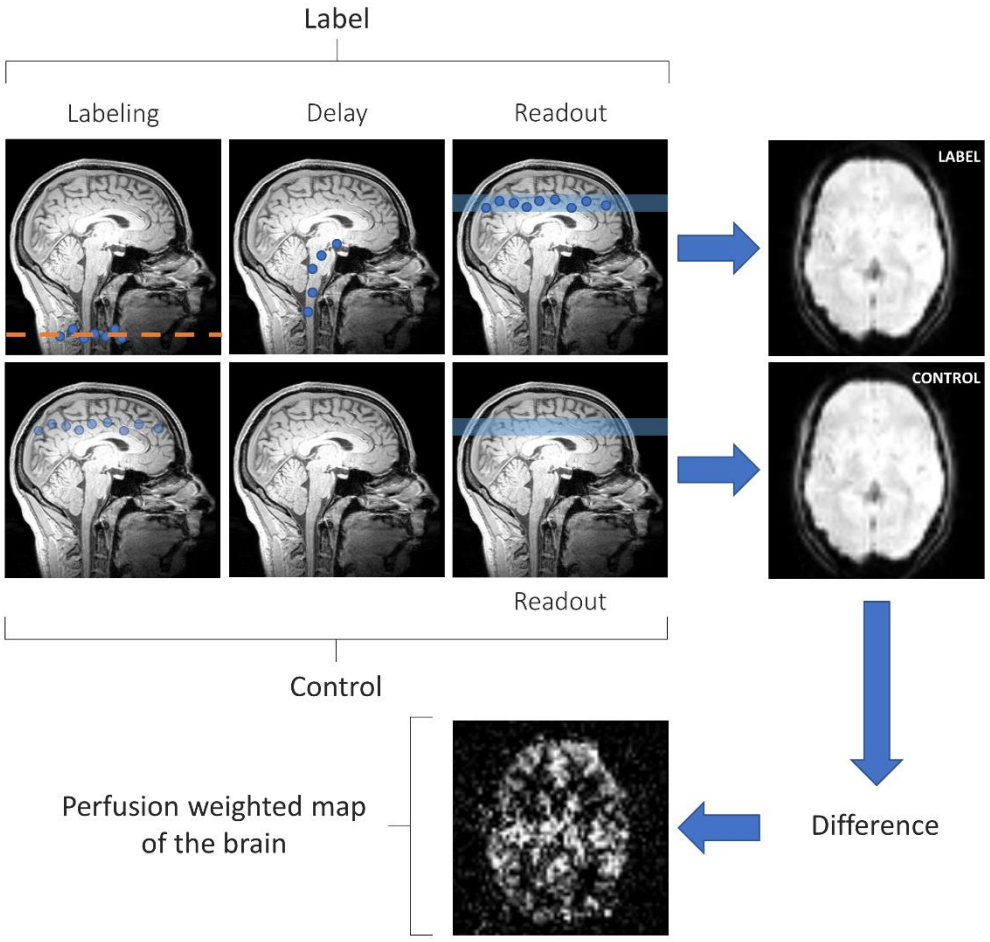

Figure 3.1: Arterial Spin Labeling generic scheme for image acquisition

Image acquisition is split in two parts: “label” and “control”. In the label part, a RF pulse first aligns the spins of arterial blood water protons in the neck. The labelled protons perfuse then through the brain. After a certain duration called the post-labeling delay, an image is acquired. The signal in label image come from the labelled protons plus the background signal. In the control part, an image is acquitted without labelled protons. Hence, the difference between the labelled image and the control (approximately) remove the background signal. Because the protons spreading is ruled by the cerebral blood flow, the resulting image of the difference is called perfusion weighted image of the brain.

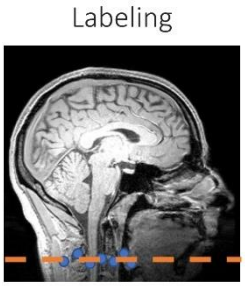

3.1.1 Spin labeling strategy

The labeling consists in sending a RF pulse on the subject neck. It inverts every proton spin in its area of effect. As protons in arterial blood water will perfuse through the brain, they will act hereafter as contrast agent. Mastering this bolus of labelled protons totally relies on the labelling strategy.

Continuous ASL

The oldest method [Williams et al., 1993], the continuous ASL (CASL) strategy consists in the labeling of a thin strip of tissue (1 cm) for a significant period of time, between around 2 s and 4 s. CASL offers a higher covered volume than the other techniques as it is mimicking a real bolus injection of contrast agent which is send to the brain through the vasculature. CASL estimated signal-to-noise ratio is also better than pulsed ASL [Wang et al., 2002], it shows a better resistance to relaxation of spins during the arterial transit time [Parkes and Detre, 2003]. Two major downsides are currently leading to give CASL up for its alternatives. Firstly, the high magnetization transfer of the bolus and its corollary misestimation of the brain perfusion. The second issue is practical: not every MRI device is able to provide such a long labeling radio-frequency pulse.

Pulsed ASL

The pulsed ASL (PASL) instead labels a wide strip of tissue (10 cm) but for a short period duration, around 5 ms. The PASL suffers less from magnetization transfer at the cost of lower estimated signal-to-noise ratio compared to CASL [Wong, 2005]. Plenty of PASL sequences declination and sub-declinations are available depending on which aspect the MRI investigation wants to strengthen: less magnetization transfer (TILT [Golay et al., 1999]), better estimation of axial brain perfusion (PICORE [Jahng et al., 2003]), less sensitivity to arterial transit time (QUIPPS [Wong et al., 1998]).

Pseudo-continuous ASL

In order to combine advantages of PASL and CASL, pseudo-continuous ASL (pCASL) seeks to mimic a CASL labeling by applying a train of rapid radio-frequency pulses [Dai et al., 2008; Silva and Kim, 1999]. Implementable on most MRI devices unlike CASL, pCASL also benefits from a higher signal-to-noise ratio than PASL. Even though the choice of the ASL labeling method can depend strongly on the context, especially when trying to detect activation zones [Borogovac and Asllani, 2012], pCASL is the currently recommended labeling strategy by the “white paper” [Alsop et al., 2015].

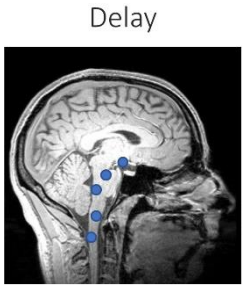

3.1.2 Time-related parameters

Timing is critical for ASL image acquisition. Indeed, as Figure 3.2 shows, readout should happen close to the maximum of ASL signal, where SNR is the best. The period of time between the start of labelling and the readout is called inversion time (TI) and is equal to the labeling duration (LD) plus the post-labelling delay (PLD) for the pCASL. However, arterial transit time is not consistent throughout the brain [Tsujikawa et al., 2016], for many reasons: arterial distance from the labeling area, disease, age, etc.. The general recommendations tend to favor long PLD (1500-2000 ms) in order to have the full bolus perfuse through all brain tissues, and thus, better CBF quantification [Alsop et al., 2015]. Depending on the topic of investigation and population studied, PLD is adapted [Gai and Butman, 2019].

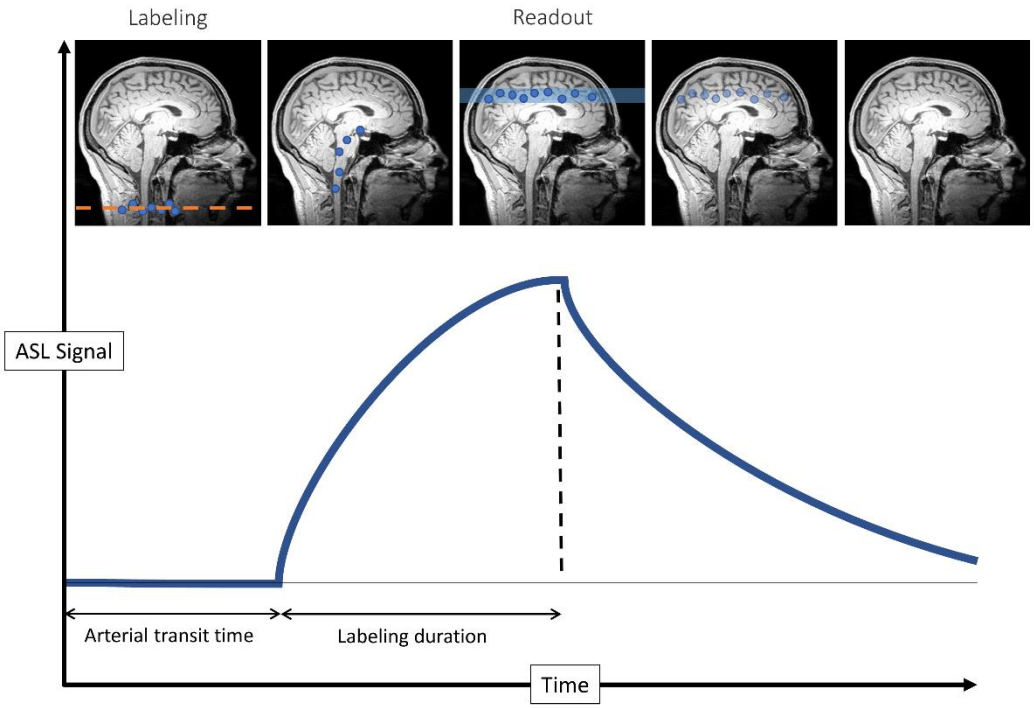

Figure 3.2: Standard model of ASL signal variation during image acquisition

We position in a slice of interest where the readout will be made. First, we consider the labeling starts exactly at time zero. The next step is the travel of the labelled protons toward the slice of interest. The duration between the labeling and the arrival of the first labelled proton is called the arterial transit time. During this moment the ASL signal is null. When the first labelled proton enters the slice of interest, the ASL signal starts increasing. It reaches its maximum directly depending on the bolus width, which itself depends on the labeling duration. In order to have the best image by maximizing the SNR, the readout should happen close to the maximum. The duration between the end of the labeling and the readout is called post-labeling delay (PLD) in pCASL, and inversion time (TI) in PASL. Once the whole bolus has reached the area of interest, the signal starts decreasing as no additional labelled protons are coming and because of the T_1 relaxation of the spins.

Readout

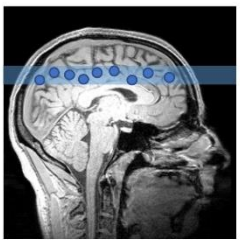

3.1.3 Readout method

Regarding the readout techniques, the main question is to acquire the image slice by slice (2D sequences) or as an entire volume (3D sequences). As the slices in 2D are time shifted from a non-negligible duration, each slice actually has its own PLD. 3D sequences cope with this issue by definition. The most common 3D sequences, such as multi-echo (RARE), fast-spin echo (FSE), gradient and spin echo (GRASE), also provide higher SNR than the typical 2D echo-planar (EPI) sequence. Despite more blurring, more distortion, and more sensitivity to motion artifacts compared to 2D EPI, 3D sequences are likely to become the technique of choice [Alsop et al., 2015; Vidorreta et al., 2013]. However, as for CASL, not all MRI devices allow implementation of 3D sequences. Since typical ASL 2D EPI readout is very similar to BOLD readout, it is hence available on most devices. Considered as a viable alternative to 3D readout [Alsop et al., 2015], 2D EPI is still widely used.

3.1.4 Subtraction

In order to get rid of the background BOLD signal and obtain the perfusion-weighted map, the label images need to be subtracted from the control images. Three main variants of subtraction have been suggested in the literature: pairwise, surround and sinc interpolation[1] subtraction.

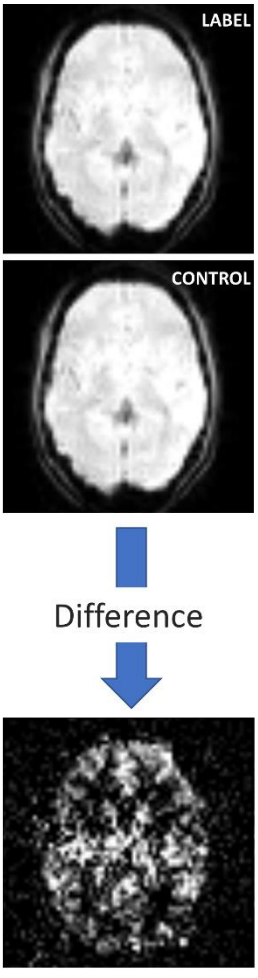

Let $(P_i)_{i\leq n}, (R_i)_{i\leq 2n}$ be respectively the PW maps, and the native control and label images. Without any loss of generality, let us consider that ASL acquisition starts with a control, i.e. each odd readout is a control image. The pairwise subtraction is the natural subtraction of a label image from the preceding (or following) control image:

$$P_i \coloneqq R_{2i-1} - R_{2i}$$

The surround subtraction linearly interpolates to the label i (control i) its two surrounding controls (labels), i.e. estimate the control (label) with the same readout time as the label i (control i). This way, the surround subtraction twice the temporal resolution to $2n$ compared to pairwise subtraction as it builds a PW maps at each TR. With respect to the parity of i, we have:

$$P_{i_{odd/control}} \coloneqq R_i - \frac{1}{2}(R_{i-1} + R_{i+1})$$
$$P_{i_{even/label}} \coloneqq \frac{1}{2}(R_{i-1} + R_{i+1}) - R_i$$

Equation 3.1: The surround subtraction of ASL

Finally, the sinc interpolation subtraction build a new family of controls from the original family. Using sinc interpolation, it estimates the controls at the

[1] Formally the Whittaker-Shannon interpolation, which uses a cardinal sinus, hence the name.

readout time of the labels, and proceed to pairwise subtraction between the labels and the interpolated controls.

Ideally, we would like to know the BOLD background signal exactly at the same time as the label readout. In task-based functional MRI, where timing is most crucial because of the external stimuli, the three methods provide very similar CBF estimation compared to a PET scan reference [Warnock et al., 2018]. However, with pairwise subtraction the control is shifted temporally of one TR from its corresponding label image. Because of this conceptual flaw of pairwise subtraction [Wong et al., 1997], surround and sinc interpolation are preferred [Liu and Wong, 2005].

PW map

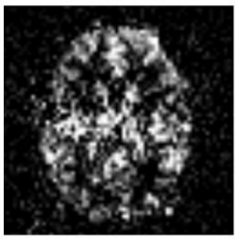

3.2 CBF quantification

Once the label subtracted from the control, the PW map obtained unlock an interesting feature of ASL: the quantification of the CBF. However, the computation that leads to CBF values involves some assumptions to be made. The following sections give an overview of the theoretical construction of the customary model that links ASL signal with the CBF.

3.2.1 The general kinetic model

The core concept of CBF computation is a model proposed by Buxton et al. in 1998 called the *general kinetic model* [Buxton et al., 1998]. It states that the ASL perfusion signal, ΔM, results from the combination of three main effects:

1. The delivery function: $C : t \mapsto C(t)$
   It is the concentration of labeled water entering a given voxel at time t.

2. The residue function: $\tilde{R} : (t_0, t_1) \mapsto \tilde{R}(t_0, t_1)$
   At a time t_1, in a given voxel, it is the fraction of labeled water that arrived at time t_0 and remains in the voxel at the time t_1.

3. The relaxation function: $\widetilde{M} : (t_0, t_1) \mapsto \widetilde{M}(t_0, t_1)$
   It describes the magnetization relaxation between the times t_0 and t_1 in a given voxel.

If the tissue is assumed to keep its physiological state, the residue and relaxation functions can be written such as for all t_0 and for all t_1: $\tilde{R}(t_0, t_1) = R(t) = R(t_1 - t_0)$ and $\widetilde{M}(t_0, t_1) = M(t) = M(t_1 - t_0)$. Let M_0 be the equilibrium magnetization of arterial blood. Let $\alpha \in [0, 1]$ be the labeling efficiency factor. The general kinetic model of ASL proposes to model the signal at time t with respect to the CBF as follows:

$$\Delta M(t) \coloneqq 2M_0 \alpha . CBF . \int_0^t C(t) . R(t - t_0) . M(t - t_0) . dt_0$$

Equation 3.2: Equation of the general kinetic model in ASL

3.2.2 The standard kinetic model

In the previous section, we describe with Figure 3.2 the general evolution of ASL signal with respect to time during an image acquisition. This shape actually results from a specific definition of C, R and M which is known as the *standard kinetic model*. This model adds three assumptions [Alsop et al., 2015; Buxton, 2005], one related to each function, in order to explicitly define them:

1. The labeled blood flow in a particular voxel is assumed to be uniform. Let $\mathrm{T1_b}$ ATT, LD be respectively the blood longitudinal relaxation time, the arterial transit time and the labeling duration. The delivery function can thus be expressed as:

$$C(t) \coloneqq \begin{cases} 0 & \text{if } \ 0 \leq t < \mathrm{ATT} \\ \exp\left(-\dfrac{t}{\mathrm{T1_b}}\right) & \text{if } \ \mathrm{ATT} \leq t < \mathrm{ATT} + \mathrm{LD} \\ 0 & \text{if } \ \mathrm{ATT} + \mathrm{LD} < t \end{cases}$$

Equation 3.3: The delivery function

2. The water exchange between tissue and blood is described by single-compartment kinetics. In particular, the labelled water is assumed to exchange between blood and tissues rapidly compared to ATT, and also without any outflow. Hence, ATT and tissue transit time can be considered as equal. Moreover, the ratio of labelled water concentration between venous and brain is then considered as constant, which is rather true [Zhou et al., 2001]. Let be λ the brain-blood partition coefficient of water, the residue function R is expressed as:

$$R(t) \coloneqq \exp\left(-\frac{t.\mathrm{CBF}}{\lambda}\right)$$

Equation 3.4: The residue function

3. The labelled water spins relaxation has the same longitudinal relaxation as blood before reaching the tissue, and the same relaxation $\mathrm{T1}$ as the tissue once the labelled water has reached it. While not strictly true, the difference have a limited impact [Alsop et al., 2015]. Under this assumption, the relaxation function simply becomes:

$$\mathrm{M}(t) \coloneqq \exp\left(-\frac{t}{\mathrm{T1}}\right)$$

Equation 3.5: The relaxation function

Once included in the general kinetic model, the expressions of the ASL signal ΔM with respect to time and depending on the sequence become:

$$\frac{\Delta M_{PASL}(t)}{q_1(t)} = \begin{cases} 0 & \text{if } 0 \le t < ATT \\ 2\alpha . M_0 . CBF . \exp\left(-\frac{t}{T1_b}\right) . (t - ATT) & \text{if } ATT \le t < ATT + LD \\ 2\alpha . M_0 . CBF . \exp\left(-\frac{t}{T1_b}\right) . LD & \text{if } ATT + LD < t \end{cases}$$

Equation 3.6: Pulsed ASL standard kinetic model

$$\frac{\Delta M_{pCASL}(t)}{q_2(t)} = \begin{cases} 0 & \text{if } 0 \le t < ATT \\ 2\alpha . M_0 . CBF . \exp\left(-\frac{ATT}{T1_b}\right)\left(1 - \exp\left(-\frac{t - ATT}{T1_b}\right)\right) & \text{if } ATT \le t < ATT + LD \\ 2\alpha . M_0 . CBF . \exp\left(-\frac{t - LD}{T1_b}\right)\left(1 - \exp\left(-\frac{LD}{T1_b}\right)\right) & \text{if } ATT + LD < t \end{cases}$$

Equation 3.7: Continuous and pseudo-continuous ASL standard kinetic model

The denominators $q_1(t)$ and $q_2(t)$ gather relaxation times and venous clearance parameters. Both $q_1(t)$ and $q_2(t)$ are close to 1 in typical pASL and pCASL implementation and are thus usually ignored [Buxton et al., 1998].

Both equations provide an evolution of signal close to the one presented in Figure 3.2. Given these equations, the extraction of CBF is explicit. A priori, every parameter in these equations are given or known, expect the arterial transit time. In consequence, in order to determine the CBF, we preferably want to refer to the third equality in the equations. This is for this very reason that long PLD/TI are recommended as we mentioned in section 3.1.2 [Alsop et al., 2015].

3.2.3 Advanced modelling

Multiple adjustment and alternatives have been proposed to the standard kinetic model. Firstly, we assume that a single PLD/TI method is used. If the hardware allows multiple PLD/TI acquisition, then the ATT can also be estimated [Francis et al., 2008]. Consequently, a readout can be safely made in the ascending part of the signal, and hence closer to the optimal SNR of ASL signal. Secondly, the standard kinetic model second hypothesis (see 3.2.2), assume that the labelled blood water exchange rapidly with brain tissues without any outflow. Parkes and Tofts proposed a two compartments model that allows to get rid of these two assumptions [Parkes and Tofts, 2002]. However, as the white paper states, alternative modelling techniques while appealing are more demanding in scan time and expertise, where the standard kinetic model shines by its robustness and simplicity.

3.3 ASL pro and cons

3.3.1 Advantages

Non-invasiveness

Contrary to DSC MRI, DCE MRI, and PET, ASL is not invasive. The absence of contrast agent injection makes ASL well suited particularly for pediatric population or more generally for population with poor venous access or contrast agent contraindication. Moreover, the non-invasiveness of ASL allow longitudinal studies of healthy subjects, where repeated agent injection is arguably questionable.

White noise

The PW map voxels signals, obtained after subtraction of label and control images, has an estimated noise that can be regarded as white [Wang et al., 2003]. Numerous processes of MRI data benefit from the whiteness of the noise of the ASL signal. Whether it is for statistical purpose or image preprocessing, plenty typical models assume the noise to be white (e.g. linear regression).

CBF quantification

As shown in section 3.2, ASL allows a quantitative measurement of the CBF under some assumption, unlike BOLD.

A proximity to neural activity

Since ASL signal relies on CBF variation, ASL is a more direct measurement of neural activity (through neurovascular coupling) compared to BOLD, whose signal variation results from complex interaction between CBF, cerebral blood volume, and local oxygen concentration.

A fine localization of functional activity

Since BOLD fMRI signal is prone to venous contamination, fASL is able to provide a better localization of the foci of activation [Duong et al., 2001; Luh et al., 2000; Tjandra et al., 2005]. Along with this idea, ASL is also read to be more specific than BOLD [Barker et al., 2013].

3.3.2 Drawbacks

Lower estimated signal-to-noise ratio

The main drawback of ASL is its lower signal-to-noise ratio compared to BOLD fMRI in particular and other perfusion methods in general. Indeed, the perfusion signal associated with neural activation obtained after volumes subtraction is estimated to explain 1% of the total variance of the total signal.

Lower spatial and temporal resolution

ASL spatial resolution is on average 2-3 times smaller than BOLD. In addition, technical timing constraints like the post-labeling delay (see section 3.2.2), ASL TR is also usually 2-3 times longer than BOLD [Liu and Brown, 2007].

Impracticability for very long arterial transit times

If in a damaged cerebral area where the ATT become too long, for example in acute stroke, the spin label vanishes before the full bolus is able to perfuse. Indeed, the ATT in this case is close or higher to the blood T1. ASL is hence impractical in this case with traditional approach [Kim and Bandettini, 2006].

Sequence variability

ASL can be implemented through numerous MRI sequences and meta-analyses can be difficult to set up, for ASL shows a high sequence parameter dependency [Grade et al., 2015; Mutsaerts et al., 2015]. The quantification of CBF also depends on the precision of the parameters used for the quantification [Parkes and Tofts, 2002]. Nevertheless, consensus seems to emerge with years, like for instance the white paper [Alsop et al., 2015].

Limited exposure

Due to the latter ASL flaws mentioned above, BOLD is predominant in clinical usage and in academic research, and is therefore considered as the standard technique in fMRI. Consequently, ASL has been mostly used for research purposes. However, the recent increasing involvement of all MRI stakeholders is highly beneficial in order to further develop ASL usage: guide for clinical practitioners [Grade et al., 2015], consensus [Alsop et al., 2015], feasibility and viability [Chen et al., 2015].

3.3.3 Application in clinical research

Brain function

First, fASL is naturally able to assess neural activity and detect functional areas [Borogovac and Asllani, 2012; Chen et al., 2015; Steketee et al., 2015]. Compared to BOLD, the test-retest ability of fASL seems better, whether in inter-subject variance or in inter-session variance [Luh et al., 2000]. Some direct comparisons with BOLD can be found in the literature, from which we have report overall conclusion in these sections on ASL aptitudes. Some focus on specific area like motor [Pimentel et al., 2013; Raoult et al., 2011], speech [Kemeny et al., 2005] or visual [Leontiev and Buxton, 2007] but also on a more general comparison [Detre and Wang, 2002; Liu and Brown, 2007; Zhu et al., 2013].

Pre-neurosurgical mapping

Some potential application to tasked-based fASL in clinical practice, the mapping of specific functional before neurosurgical intervention area, that helps surgeon to avoid damaging patient capacity [Hirsch, 2012; Paya et al., 2018].

Brain dysfunction

As it provides quantification of CBF, fASL can be a serious contender to BOLD when it comes to pathologies evaluation, whether it is for diagnostic or longitudinal follow-up. The general idea of the study of cerebral dysfunctions through fASL (or functional imaging in general) is to compare functional areas of control subjects with those of diseased patients. For instance, fASL can be effective for Alzheimer's disease [Alsop et al., 2010; Wolk and Detre, 2012; Zhang et al., 2016], where CBF may be a biomarker at early stage of the disease. We can also find some fASL studies for schizophrenia [Kindler et al., 2015], multiple sclerosis [D'haeseleer et al., 2011] and drug studies [Nordin et al., 2013; Wang

et al., 2011]. FASL is also able to investigate a specific set of pathologies with CBF impairment, such as acute stroke [Wang et al., 2012] or chronic fatigue syndrome [Boissoneault et al., 2016].

Section 4. Resting-state functional MRI

4.1 Introduction

4.1.1 Tasked-based fMRI limitations

The brain is a complex network of neurons structurally interconnected, roughly organized in units dedicated to specific functions. One main objective of functional imaging is to identify these functional units and their roles. We briefly introduce how task-based fMRI tackles this problematic by instructing the subject to perform particular tasks. Under controlled experimental conditions, task-based fMRI is expected to exhibit the cerebral areas implicated in the task, thanks to the neurovascular coupling. One can imagine numerous experimental designs and paradigms in order to target explicit functions, e.g. motor, language, vision, memory or audition. However, it is difficult to assume that task-based fMRI can explore numerous brain functionalities. For practical reasons first, as the implementation of the task is limited by the MRI device itself. Moreover, some brain functions could be too complex to allow a paradigm design to ever exhibit it. Second, task-based fMRI can only target one or few functions at a time, and does not inform on how the functional areas are working together, where brain can actually combine numerous functions at the same time. Task-based fMRI display eventually a fragmented information of brain organization.

In this chapter, we present the second way to explore brain function with MRI without exposing the subject to a stimulus. Even at rest, i.e. without performing any particular physical or cognitive task, the brain does not enter an idle state: the neural spontaneous activity remains intense. This is illustrated by energy consumption: the metabolic activity induced by a task consume only 0.5% to 1% of the brain total energy, whereas the resting-state spontaneous neuronal activity represents 60% to 80% of the energy consumption [Raichle and Mintun, 2006]. Communication between brain regions is therefore likely to play a key role in the brain's control over physical and cognitive processes, the question is now how to explore it.

4.1.2 Functional connectivity

The functional areas in task-based fMRI are constructed by exhibiting voxels that have a signal matching an expected signal regarding the paradigm. Corollary, this set of voxels are likely to have a similar signal to each other, as they are all similar with the expected signal. These signals match because, in these voxels, the neurons activate at the same moments, defined by the task. Another interpretation of a functional area in this case is that the neurons belong to the same functional area because they activate at the same time. In other words, a functional area can be constructed by aggregating voxels with similar signals. This relationship between neurons (voxels) is the core concept of resting-state fMRI: functional connectivity. Exploring functional connectivity in resting-state copes with the task-based fMRI issues mentioned above. Indeed, resting-state fMRI (rsfMRI) is a global assessment of brain organization, as it can gather every voxel in different functional areas through their functional connectivity. On a higher scale, by investigating the relationship in terms of functional connectivity of these new functional areas, rsfMRI depicts the architecture and the interaction between the functional units

of the brain. Eventually, the examination of functional connectivity in the brain can be of considerable importance, providing valuable new insights in the core organization of the brain.

Functional connectivity is defined by the temporal interdependence of neural activity throughout the brain [Aertsen et al., 1989]. In the context of rsfMRI, functional connectivity is investigated by networking voxels which provide a similar signal, in other words, by gathering locations that share similar neuronal activation patterns. In the case of anatomically separated cerebral areas, the functional connectivity reflects the existence of an underlying functional communication between regions. The term connectivity can be somewhat misleading: we are talking about similar behaviors, not spatial connections. While a spatial connection mandatorily underlies any functional connection, functional connectivity cannot be extrapolated from connectome, and rsfMRI does not explore this correspondence between function and structure.

4.1.3 Spontaneous activation and resting-state fMRI

In 1995, Biswal and colleagues conducted a study in which they first estimated the whole motor area of a cohort of subjects, with tasked-based fMRI. They observed that when the subjects were at resting-state, i.e. without performing any task, signals from voxels in the right and left regions of the estimated motor area were highly correlated [Biswal et al., 1995]. Resting-state fMRI was born. Indeed, they both show that, even at rest, the signal/activation pattern of a functional area remains homogeneous, and also that left and right motor area, while distant, suggest a functional connectivity relationship, forming the motor network. From this pioneering study, numerous studies have reproduced this result in the motor network [De Luca et al., 2005] and have extended it to different functional networks like auditory, language, visual or even subtle functions such as salience [Cordes et al., 2002; Damoiseaux et al., 2006; De Luca et al., 2006; Fox and Raichle, 2007; Greicius et al., 2009; Lowe et al., 1998]. As resting-state fMRI globally investigates activation patterns, the whole brain can be functionally partitioned into atlases of networks at different scales [Fan et al., 2016; Varoquaux et al., 2011]. The construction of resting-state functional networks is addressed in section 4.3 and following.

Once the functional networks estimated, the next step is to investigate their interactions. The functional connectivity at the functional networks scale depicts how these networks interact. The key concept is to consider the brain as a unique integrative network of the estimated functional networks, assimilated with the mathematical structure of a graph [Van den Heuvel and Hulshoff Pol, 2010; Wang et al., 2010]. The graph properties model the functional architecture: each node corresponds with a functional network, and edges configuration depicts how they interdepends.

In a nutshell, resting-state fMRI is all about measuring similarities between the signals from different voxels. By gathering voxels that share similar signal, it exhibits functional networks, i.e. brain region that share similar activation patterns. At a group of voxels scale, it models the communication channels between the functional networks, and hence, the brain functional architecture.

4.2 Preprocessing resting-state fMRI data

In this section, we address the generic preprocessing of resting-state fMRI data. While identifying the best preprocessing is still an open topic in rsfMRI [Gargouri et al., 2018], a general routine can be discerned in the literature. Fortunately, most preprocessing steps of rsfMRI are shared with task-based fMRI [Cole et al., 2010].

Slice timing correction

Regardless of the MRI sequence, a whole volume is never instantaneously acquired. For instance, with the standard 2D EPI sequence (see section 3.1.3), the 3D volume is reconstructed from 2D slices acquired at different times. Also known as temporal realignment, slice timing correction is the preprocessing step that aims to correct the differences in acquisition times [Henson et al., 1999]. The slice-timing correction is implemented by temporal interpolation of available data [Parker et al., 2017]. The slice-timing correction benefice seems limited in rsfMRI [Gargouri et al., 2018]. However, the recent paper from Parker and Razlighi show that even if contribution of slice-timing alone is difficult to exhibit, it is beneficial when considering the crossed factorial influence of multiple preprocessing steps [Parker and Razlighi, 2019].

Motion correction

Also known as spatial realignment, the motion correction is the step that corrects the unavoidable motion artifacts caused by subject movements during a fMRI acquisition. The inconsistencies caused by motion between consecutive volumes hinder the estimation of functional area made after the preprocessing [Muraskin et al., 2013; Power et al., 2012]. The usual practice to cope with motion issue is simply to perform a rigid registration of every volumes on one volume of reference.

Registration - Normalization

In order to compare subjects with each other, the images need to be registered to ensure that the structural architecture corresponds. For a cohort of subjects, the registration of all subjects on the same reference is called spatial normalization [Friston et al., 1995]. The reference is usually made on a brain template like the Montreal Neurosciences Institute template MNI152 [Brett et al., 2002]. However, spatial resolution of fMRI images is poor compared to MRI anatomical template, especially fASL images for which direct registration to template can easily fail. The standard practice is to use a subject high-resolution anatomical image as a buffer in the registration of the functional image to the template space. The functional image is registered to its corresponding anatomical image, then the anatomical image is registered to the template. Last, the two transformations are composed to construct the one that registers the functional image to the template. The comprehensive review by Gholipour and colleagues details the aspects of functional data registration [Gholipour et al., 2007], from which we have extracted Figure 4.1.

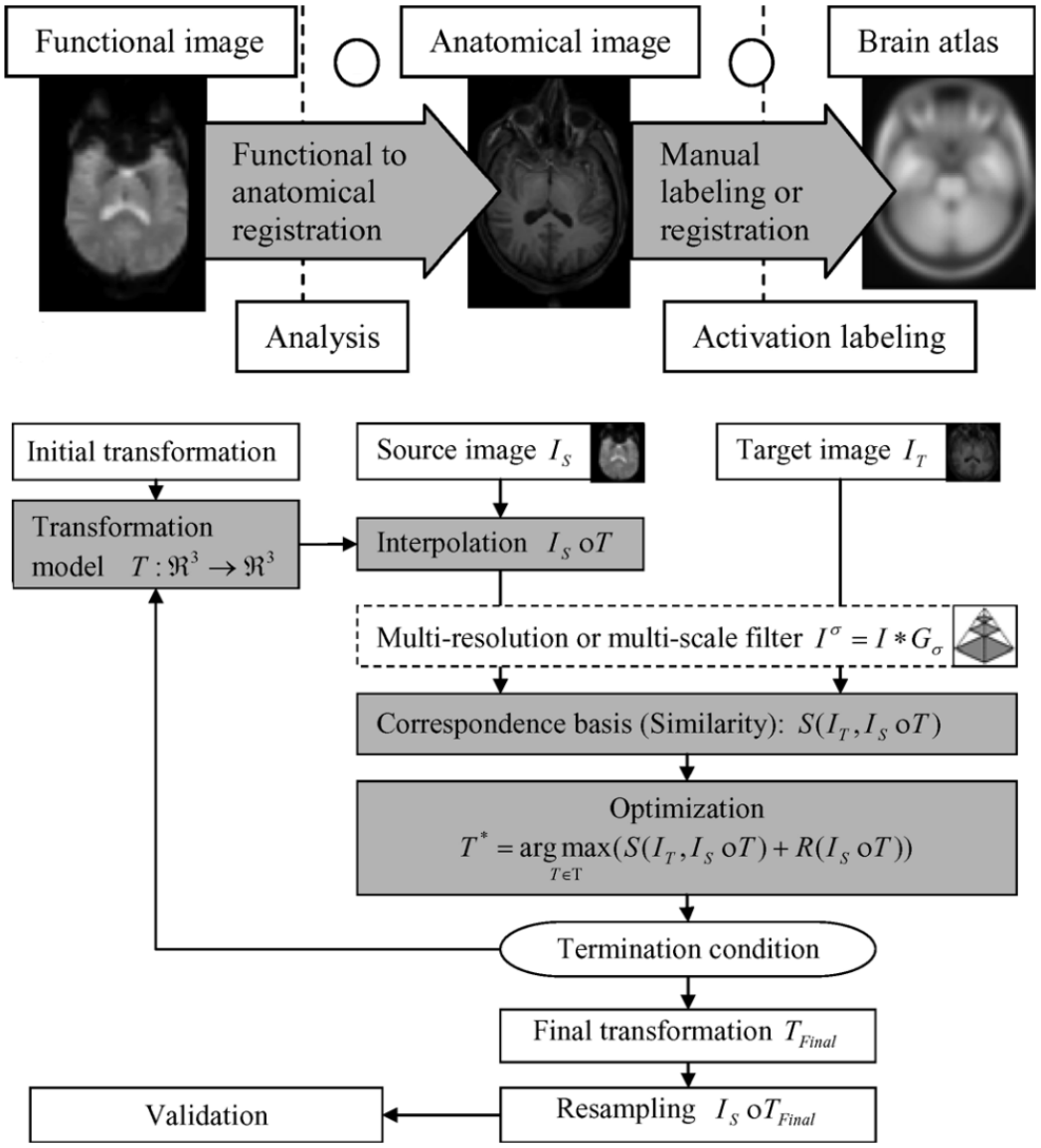

Figure 4.1: Generic registration of a functional image

Illustration and algorithm are from [Gholipour et al., 2007]. First step is usually to register subject functional acquisition to subject anatomical acquisition. Then the anatomical image is registered on the template, and the transformations are composed to register functional image on the template. The algorithm describes the usual four steps of a registration: transformation, interpolation, correspondence and optimization. The very last step is usually a resampling in the template resolution.

Spatial smoothing

Registration and normalization of functional images can produce small errors. Most if not all studies use a spatial smoothing as a correcting procedure. Specifically, the spatial smoothing is made through filtering signal in each voxel with gaussian kernel density estimation. The smoothing is parametrized by the Gaussian standard-deviation, with higher variance giving increased smoothness. Full width at half maximum radius are in a range from 3 to 12 mm in rsfMRI, and most of the time between 5 and 6 mm, [Alakörkkö et al., 2017].

Temporal filtering

In task-based MRI, the frequency of the stimuli and this way the expected neural activation of interest are controlled. Hence, the signal interfering with neural activity self-signal, such as respiratory or cardiovascular signal, can be removed by the implementation of a high-pass/low-pass filter [Birn et al., 2008; Van Dijk et al., 2010]. In resting-state, the functional networks are estimated through spontaneous random activations that occur mostly at a frequency between 0.01 – 0.1 Hz [Biswal et al., 1995; Damoiseaux et al., 2006]. More precisely, this is the frequency range where spontaneous fluctuation are easier to detect, whether it is for ASL or BOLD [Aguirre et al., 2002]. Indeed, recent studies manage to perform the extraction of resting-state signal at higher frequency [Chen and Glover, 2015; H. L. Lee et al., 2013; Trapp et al., 2018]. Regarding lower frequency (<0.01 Hz), they are discarded mostly because of the difficult extraction of the signal of interest [Tong et al., 2019], especially in BOLD and less in ASL [Dai et al., 2016]. There is no consensus in ASL and BOLD on the range of frequency to filter, as a narrow filter discards signal of interest [Liang et al., 2012] while larger filter include more physiological noise [Gargouri et al., 2018].

Additional denoising

Other sources of physiological noise can also be removed from the time series. For instance, respiratory and cardiovascular signal can easily be monitored in MRI device. Their signals used as regressors in a (linear) model to explain signal in the voxels allow a posteriori to subtract them from the original time-series. The widespread algorithm RETROICOR [Glover et al., 2000] is an example of this regression, and it is effective in both BOLD and ASL [Restom et al., 2006]. Some voxels display a signal that is most likely to have no or barely no functional signal, like the voxels outside the brain, in bones, in CSF or in white matter. Beside masking them for further analysis with grey matter map, their signals can be accounted in order to denoise images. For instance, the algorithm COMPCOR [Behzadi et al., 2007] uses principal component analysis (PCA) on a set of voxels that have a high partial volume in CSF or WM. The first components (in terms of variance) of the PCA are then used as confound regressors in a linear model to explain the signal in voxels of interest. Finally, COMPCOR subtracts the confound regressors from the original signal a posteriori.

4.3 Detecting functional networks with Seed-Based Analysis

In the introduction we presented functional connectivity as similarities in neural spontaneous fluctuations that can be investigated by measuring similarities between voxels time-course. A natural investigation is then to directly compare the linear correlation between pairs of voxels to assess their functional connectivity. This is the most classic implementation of seed-based analysis (SBA), and the very first method to be used [Biswal et al., 1995]. Actually, seed-based analysis is an extremely polymorphic method, for which we present below a general step-by-step heuristic.

Selecting the seeds

Seeds are a set of subsets of voxels from which we investigate functional connectivity and build associated functional networks. The subsets of voxels can be singletons, i.e. single voxels, spheres of voxels, ROI given by structural atlas (like Brodmann's) or also tasked-based functional area that are called localizer in this context. ROI are generally used when the study is made directly on the graph structure.

Modeling the functional connectivity

In parallel with the seed, a measure of similarity between voxels signal that models the functional connectivity has to be set. The satisfactory measures of functional connectivity are numerous: linear correlation which is the most common one, Spearman's correlation which allows to get rid of signal normality assumption, mutual information which translates statistical (in)dependence, spectral coherence that considers the signal from the frequency space point-of-view, etc. Most measure of similarity can be directly used on single voxels to establish functional connectivity. However, if seed are region-sized, the score needs to be adapted into a new variable of interest: for instance, through a mean, a weighted mean, an eigen vector, whether it is on signals or scores values. Even on singleton, the measure of similarity can also be adapted to extend the definition of functional connectivity. The correlation, for example, can be lagged in order to take into account of time shifts between neural activation, and this way has found applications in rsfMRI [Mitra et al., 2014].

Thresholding

Scores do not lead directly to a qualitative assessment of functional networks, but rather to a score map that requires a threshold to delimit the spatial layout of functional networks. At this point, a statistical test is usually made, depending on the score used, and with an adapted implementation/correction (e.g. multiple comparisons). The figure below from [Van den Heuvel and Hulshoff Pol, 2010] illustrates the heuristic.

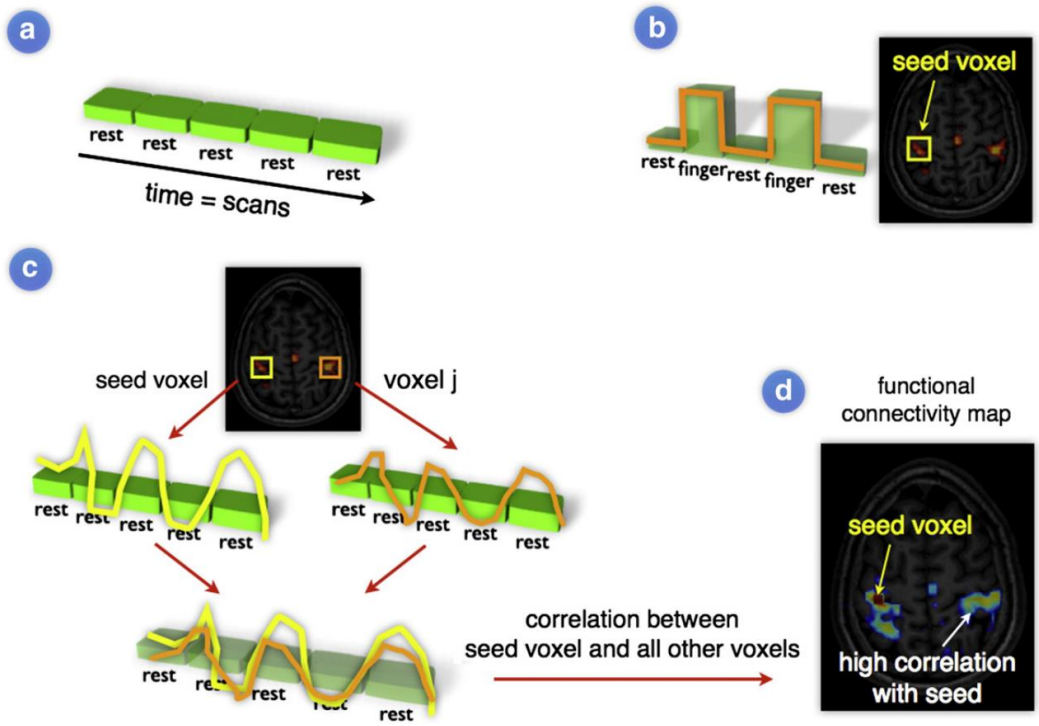

Figure 4.2: Detection of the motor area with Seed-based analysis

Figure comes from [Van den Heuvel and Hulshoff Pol, 2010] and illustrate the first rsfMRI experiment of [Biswal et al., 1995]. Resting-state MRI paradigm, from task-based MRI point-of-view is identically null (A). By using tasked-based MRI (B), where task was alternance of finger-tapping and rest, Biswal and colleagues first delineate a task-based motor area, that provide the voxel that will be used as seeds. From this motor area they compare voxels signal from the left and right motor area (C) using linear correlation. In (D), the voxels that have high correlation with the seed, i.e. that are considered to show functional connectivity, i.e. that have similar activation pattern, are part of the same functional network: the motor area. It follows the heuristic of SBA: defining seeds, defining a measure of similarity that models functional connectivity, selecting a threshold (underlying here).

4.4 Detecting functional networks with Independent Component Analysis

The name reminds the Principal Component Analysis (PCA) and this is deliberate: Independent Component Analysis (ICA) is also a factor analysis method that builds a new basis of variables. However, while PCA expresses the set of observations with variables that capture the maximum variance in decreasing order, and also that are decorrelated. The objective of ICA is to build a set of statistically independent variables.

4.4.1 Problematic

A general formulation of the problem can be constructed as follows: let Y be a known vector (outputs) of size $n \in \mathbb{N}$, X an unknown vector of independent sources of size $p \in \mathbb{N}$, and a function M such as: $Y = M(X)$. Let also I be, a measure of the statistical dependence. ICA builds a pair $(\hat{X}, \hat{S})$ with $\hat{X}$ a best estimation of X with respect to I, and $\hat{S}$ a source separation function, such as:

$$\hat{X} \coloneqq \hat{S}(Y), \text{ with } \hat{S} \coloneqq \underset{\tilde{S}}{\operatorname{argmin}}\, I(\tilde{S}(Y))$$

Equation 4.1: General formulation of Independent Component Analysis problematic

4.4.2 Additional hypotheses

In order to propose resolution algorithms for such problems we must formulate some hypotheses.

Linearity

Remember that along with the estimation of the source $\hat{X}$, we are looking for a function $\hat{S}$ that best estimates S, with: $S \circ M = I_d$. However, the existence of such a function S is not guaranteed, and even if S exists, there is no general resolution method in this case. [Jutten and Karhunen, 2004] address the generic case issue. In order to overcome the well-definition issue, we will therefore assume that the dependence of the output signal on the sources is linear, i.e. we are looking for a pair $(\hat{X}, \hat{S})$ such as we can write the ICA ansatz with matrices:

$$\hat{X} \coloneqq \hat{S}.Y, \text{ with } \hat{S} \coloneqq \underset{\tilde{S}}{\operatorname{argmin}}\, I(\tilde{S}.Y)$$

Equation 4.2: Linear formulation of Independent Component Analysis problematic

Under the linearity hypothesis, the model requires two additional assumptions to be identifiable [Comon, 1994]:

1. A traditional assumption of factor analysis method on dimension: the rank of the separation matrix S must be equal to the number of sources, which requires having as many or more output signals as there are sources to find. This allow to generally well-define an inverse for $\hat{S}$, which is the mixing function $\widehat{M}$.
2. At most one source can follow a normal distribution [Hyvärinen, 1999a]. The formal demonstration would probably be superfluous here. The key idea lies on

the fact that according to the central limit theorem, the sum of independent and identically distributed random variables tends to have its average distribution getting closer to a Gaussian. Consequently, multiple gaussian sources, or close to gaussian sources thwart ICA resolution heuristic, under previous assumptions.

Indeterminacies: amplitude and order

Since we are looking for the separation matrix and the vector of the independent components at the same time, it is possible to multiply a component (one of the estimated sources) by a scalar and also the corresponding column in the separation matrix by the same scalar. This results in an indeterminacy on the amplitude of the components. In practice, ICA resolution algorithms overcome this issue by setting the source variances to 1, i.e.: $\forall i : Var(\hat{X}_i) = 1$. The last remaining indeterminacy is the same as in PCA, which is on the sign of the components, since: $\forall i : Var(\hat{X}_i) = Var(-\hat{X}_i)$.

However, unlike PCA, ICA does not give an order to the components. Indeed, if P is a permutation matrix, then under the previous assumptions:

$$X = S.Y \Leftrightarrow Y = M.X = M.P.P^{-1}.X = \dot{M}.\dot{X}$$

Where $(\dot{M}, \dot{X})$ are also a pair of feasible solutions and permutations of M and X.

4.4.3 Implementation

In the previous section, we did not specify the measure of statistical independence. The implementation of independent component analysis in functional MRI is not unique, and it is precisely the choice of the measure that will define the family of the subsequent algorithms. The choice of the algorithm is usually adapted to the study being carried out, e.g. a subject-scaled study [Calhoun et al., 2001] or a group study [Varoquaux et al., 2010]. The subsequent algorithms are numerous. For instance, the Matlab toolbox GIFT with its addon ICASSO offers 17 different algorithms [Himberg and Hyvärinen, 2003]. These algorithms can be split into two family depending the measure of independence they use in their implementation. The minimization of mutual information represents a first class of algorithms for ICA, of which the oldest and most famous representative is the Infomax algorithm [Sejnowski and Bell, 1995]. Algorithms maximizing negentropy form the second class of the most used in ICA. Its most famous representative is the FastICA algorithm [Hyvärinen, 1999b].

Construction of the functional networks

Once accomplished, ICA provide a set of signals as independent as possible. In order to estimate the functional networks, remember that ICA assumes the voxels signal to be a linear combination of the independent signals. As for every statistical linear model, one can test if the variance explained by each of the variable (independent component) is significantly not null. Hence, each voxel that verifies this hypothesis has a significant part of its variance explained by the corresponding independent component. Consequently, they all share a similar neural activation pattern, in other words, they belong to the same functional networks. Note that, depending on the algorithm used, the method used to reconstruct the functional networks varies, and we have mentioned the generic case.

4.5 Alternative modeling methods

Some alternative factor analysis methods to ICA are reported in reviews [Cole et al., 2010; Fox and Raichle, 2007; Van den Heuvel and Hulshoff Pol, 2010]. For instance, Principal Component Analysis [Friston et al., 1993] as well as Singular Value Decomposition [Hirsch, 2006] can be used to identify functional networks . These two techniques for changing the basis of representation are, however, rarely implemented in the in practice, with the ICA being widely preferred.

Statistical clustering techniques form another family of methods for resting-state MRI. Indeed, they seem to be natural investigation techniques if we consider that a functional network is a cluster of voxels gathered according to certain conditions of similarity. It should be recalled that, in the context of fMRI, only unsupervised classification methods make sense, otherwise the fMRI topic would be solved. Typical clustering methods can be used in resting-state MRI, such as hierarchical classification (HAC) [Cordes et al., 2002; Salvador et al., 2005], and to a much lesser extent, the K-means [M. Lee et al., 2013]. With regard to the HAC, the overlap with the ICA and the SBA is satisfactory for the classical networks [Raichle et al., 2001], and the HAC overcomes the difficulty of interpreting the ICA components. Although being theoretically a global method unlike the SBA, the two-by-two comparisons between voxels are not computed directly in practice, the data are previously filtered [Cordes et al., 2002] and/or the classification operates directly on regions of interest [Salvador et al., 2005]. In addition, the HAC shows limited results for intra-group comparisons [Van den Heuvel et al., 2008], even though HAC naturally provides an interpretation at different scales of functional connectivity.

4.6 Organization of the resting-state networks

Whatever modeling technique has been used to estimate the functional networks, we can now examine their overall organization, using graph theory. We present graph theory in introduction, as a welcome theoretical framework to describe the brain function architecture. A graph G is a pair $G \coloneqq (V, E)$, where V is the set of nodes identifying the functional networks, and E the edges characterizing their interactions, as Figure 4.3 shows. The nodes (resting-state networks) are not necessarily defined through a previous rsfMRI experiment, and are sometimes defined through task-based MRI or atlas of subcortical region. A graph is identical to its adjacency matrix, which tabulates the (weighted) connections between functional networks. A natural association can be made between the adjacency matrix and a correlation matrix between signals representative of each nodes. More generally, any covariance related matrix fits as adjacency matrix [Horwitz et al., 1995; Varoquaux and Craddock, 2013].

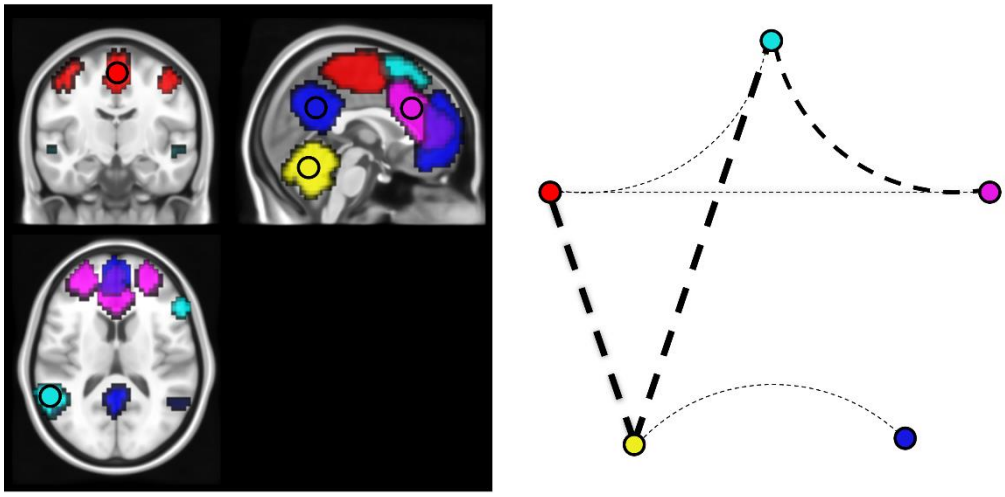

Figure 4.3: Construction of a graphs from functional networks

Left figure shows a simplified case where only five functional networks are considered to build the corresponding graph on the right. The edges thickness translates the strength of the functional connectivity, as the construction of the edges is made quantitatively, e.g. with linear correlation.

Once constructed, the graph topology will provide in-depth insight of the global brain functional organization. Here are some properties of interest [Bassett and Bullmore, 2017; van den Heuvel et al., 2008]:

- Node degree: the number of edges connected to a node. The higher the degree the more the node corresponding cerebral area is likely to be involved in different function.

- Nodes distance: the comparison of the anatomical distance (in mm) with distance in number of edge between two nodes informs on the relation between structure and function [Salvador et al., 2005].

- Centrality of a node k: number of distinct pair of nodes (i, j), such as the shortest path from i to j is through k. A high centrality indicates the nodes act as a hub in functional communication. A drop of centrality can characterizes pathologies like Alzheimer's disease [Sanz-Arigita et al., 2010].

- Clustering coefficient of a node k: the ratio of the number of edges between the nodes connected to k divided by the number of edges that could possibly exist in the complete graph formed by k and its neighbors. It illustrates how neighbors are interconnected.

- Characteristic path length: the average distance (in number of edges) between each pair of nodes. A small characteristic length translates a functional communication efficiency, and it is fostered by nodes with high centrality.

While all of these scores provide useful insight of functional organization [Bullmore and Sporns, 2009; Stam et al., 2016], the two last properties have qualified the brain functional architecture. A healthy brain shows a high average clustering coefficient combined with a short characteristic path length, which is called a *small world* network [Barrat and Weigt, 2000]. The small world architecture has been exhibited for both BOLD [Hayasaka and Laurienti, 2011; M. Lee et al., 2013; Salvador et al., 2005; Wang et al., 2010] and ASL [Liang et al., 2014, 2013]. Numerous explicit illustrations of small world organization are found in human social organization [Leskovec and Horvitz, 2008]. For instance, the "six degrees of separation" conjecture states that people are six or less social connections away to each other, as a consequence of mankind's small world social organization.

4.7 Resting-state fMRI applications

As the other functional imaging techniques, rsfMRI provides a better understanding of the brain function and especially the organization of the functional areas of the brain. Resting-state fMRI already benefits from the MRI advantages: good spatial resolution and non-invasiveness. It differs from task-based fMRI by its ability to estimate numerous networks at once, to depict a global functional organization of the brain. Resting-state fMRI is also more inclusive, as the resting-state is easier to achieve compared to tasks, especially for pediatric and elderly population, but also for cognitive impaired patients.

For these reasons, rsfMRI has found some niche clinical applications in pathologies investigation, particularly when cognitive impairments are involved. For instance, functional connectivity is altered in disease like schizophrenia [Kindler et al., 2015; Lynall et al., 2010], major depression [Mulders et al., 2015], Alzheimer's disease [Agosta et al., 2012; Sanz-Arigita et al., 2010]. Resting-state fMRI, as a global investigation of function, is also adapted for neurodegenerative disease like multiple sclerosis [Cruz-Gómez et al., 2014; Faivre et al., 2012; Filippi et al., 2013] or amyotrophic lateral sclerosis [Mohammadi et al., 2009; Trojsi et al., 2017].

Despite its lower SNR, but thanks to its closer proximity to neural activation and CBF quantification, resting-state ASL has proven to be a serious contender to resting-state BOLD in schizophrenia [Zhu et al., 2015] and Alzheimer's disease [Alsop et al., 2010; Zhang et al., 2017]. Resting-state ASL has also found its own clinical applications with investigation of chronic fatigue syndrome [Boissoneault et al., 2016] and catatonia [Walther et al., 2016].

4.8 Discussion

4.8.1 The resting-state and the default mode network

The resting-state is usually defined by the absence of cognitive activity of subject. While easier to achieve in general than task-based fMRI conditions, it is also harder to control. Table 4.1 shows the instructions given to the subjects to achieve resting-state. The instructions differ from authors to authors, and for instance, the "eyes" condition, open, closed or fixed, induces small changes in networks estimation [Patriat et al., 2013].

Another potential characterization of the resting-state is in the detection of a specific network, called the *default-mode network* (DMN). The DMN owes its "default" attribution, by the fact that it was first associated as a set of regions with an increased neural activity when the subject does not perform any task [Raichle et al., 2001]. In other word, studies investigating task-based activations found that the neural activation of the so called default-mode were anticorrelated with the task paradigm [Broyd et al., 2009]. However, posterior research in task-based fMRI found that actually, DMN is related to subject self-projection in imaginary situation [Buckner and Carroll, 2007]. This illustrate an issue with rsfMRI: without any auxiliary information, rsfMRI cannot qualify to which function a set a functional network is dedicate. This shows also how rsfMRI and task-based fMRI are complementary methods: rsfMRI investigate functions globally without qualification, where task-based fMRI qualifies functions, but one at a time.

Instructions	Eyes	Sleep	Movement	Cognitive
[Chuang et al., 2009]	Closed	Keep awake	Lie still	Nothing specific
[Jann et al., 2015]	Fixed	?	Lie still	?
[Varoquaux et al., 2011]	Closed	?	?	?
[Braun et al., 2012]	Closed	?	?	Relax
[Dai et al., 2016]	Closed	Try not to	?	?
[Wang et al., 2009]	Closed	?	Motionless	Relax
[Storti et al., 2013]	Open	?	?	Relax
[Olafsson et al., 2015]	Fixed	?	Lie still	Nothing specific
[Iraji et al., 2016]	Closed	Avoid	Lie still	Relax
[Smith et al., 2013]	Fixed	Try not to	?	Nothing specific
[Pruim et al., 2015]	Open	?	?	Relax
[Li et al., 2012]	Closed	?	Lie still	Relax
[Kindler et al., 2015]	Closed	Stay awake	?	?
[Zhu et al., 2013]	Open	?	Lie still	Rest
[Greicius et al., 2009]	Closed	?	Lie still	?
[De Luca et al., 2006]	Closed	Do not fall	?	Rest
[Sanz-Arigita et al., 2010]	Closed	Do not fall	Lie still	Nothing specific

Table 4.1: Instructions to achieve resting-state in literature

We gathered instructions given to subjects in randomly selected paper that perform rsfMRI experiment. We split them into four type. Subject can be either ask to close his eyes, keep them open or to fix a reticle. Question marks indicate when authors did not report instruction regarding the sleep, movements, or cognitive state.

4.8.2 Preprocessing

From a statistical point of view, the number of variables that can explain variability in the resting-state functional architecture are numerous. The subject gender [Tian et al., 2011], age [Achard and Bullmore, 2007], mental state [Greicius, 2008], the number of subjects in the study [Termenon et al., 2016], are among many others, source of variability. Some of these factors of influence are however interesting, in that sense they can allow to discriminate healthy and diseased subject. Besides subject induced variability, the preprocessing is also a great source of variability.

Let us start with a simple but key example. We mention that Gaussian smoothing is used to reduces registration and normalization errors. A consequence sometimes beneficial of the spatial smoothing, is that the smoothed voxels signal can only be closer to a Gaussian distribution, thanks to the central limit theorem (by definition a smoothed signal is the weighted average of itself with its neighbors' signal). While assuming Gaussian distribution often allows the use of methods with more statistical power (e.g. linear regression in task-based fMRI), we also mentioned that ICA is more efficient with the absence of Gaussian distribution, which can question the smoothing. By spreading voxels signal, specifically activation signal, spatial smoothing is also prone to trade specificity for sensitivity, at best [Bennett and Miller, 2010; Pajula and Tohka, 2014]. At worst, the Gaussian smoothing trade specificity for an increasing number of false positive, which seems to be the case in numerous fMRI studies that do not take this into account in their statistical analysis [Eklund et al., 2016]. While smoothing radius strongly affects the spatial layout of functional networks as Figure 4.4 shows, its influence at the graph scale does not impair small world property [van den Heuvel et al., 2008; Zalesky et al., 2012], besides an overestimation of nodes centrality [Alakörkkö et al., 2017]. We see that even for Gaussian smoothing that has only one parameter, the functional area estimation shows strong variability, with no obvious values to advise for general usage.

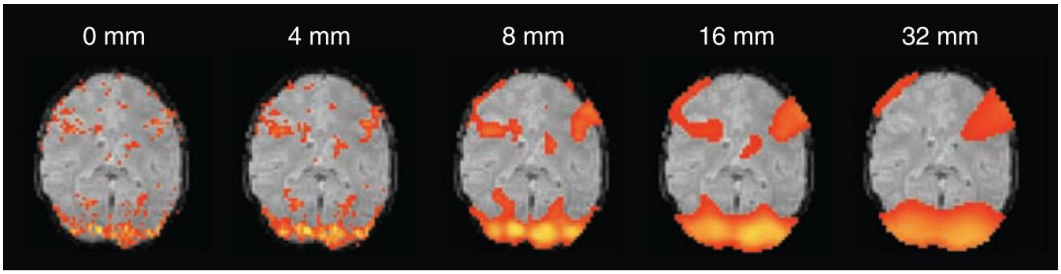

Figure 4.4: Effect of the Gaussian smoothing radius (FWHM)

Illustration comes from [Poldrack et al., 2011]. With no smoothing (radius=0mm), there are many microclusters, and it is difficult to distinguish between those that correspond to noise and those that correspond to a real functional area. On the opposite, at 32 mm, the clusters are consistent, but because of the high radius, foci of activation are blurred. Furthermore, the top left part of the functional area, which looks relevant between 4 mm and 16 mm, has been eroded.

Since there is no truth functional area in rsfMRI in particular and in fMRI in general, finding the best preprocessing is a very challenging topic [Aurich et al., 2015; Bennett and Miller, 2010; Gargouri et al., 2018]. Indeed, notwithstanding the numerous fMRI sequence and data analysis, even the simplest preprocessing that allow the detection of functional networks already include several different modeling, which can each have numerous parameters, that each can induce variability in the functional network estimation process.

4.8.3 Functional connectivity modeling

Functional connectivity has a simple definition: similarity in neural activation patterns. However, in literature, the functional connectivity is often confused with how it is modeled. In SBA, plenty of similarity measures can be used (see section 4.3). Let us focus on the most typical one: linear correlation. Hence, functional connectivity is modeled through linear correlation between signals. In ICA, as the name states, this is statistical dependence that models functional connectivity. While these two modeling correspond well to the actual definition of similarity in neural activation patterns they do not lead to the same estimation of neural networks in essence. However, as Varoquaux and Craddock stated in [Varoquaux and Craddock, 2013], there is no universally better parcellation method, the most important is to keep in mind this methodological nuance when analyzing rsfMRI data.

4.8.4 Seed-based analysis and ICA

Seed-based analysis strength is that it provides a straightforward approach and simple interpretability in the functional connectivity modeling. However, SBA requires an a priori in the selection of the seeds, whether it is single voxels or a ROI. As SBA cannot be performed on every voxel, the selection of the seeds is never naïve and relies on auxiliary information: task-based functional area, expected location, area with unknown functionality. This raises a question about the robustness of SBA. Indeed, the seeds selection has an influence on the networks estimation as shown in Figure 4.5. Indeed, even close seeds do not share the exact same noise, and the measure of similarity always capture a part of this noise. Nonetheless, the SBA is considered as having an average to high reliability [Shehzad et al., 2009].

ICA copes with this issue by definition, as it focuses on reconstructing a set of independent signals without prior spatial assumptions. Moreover, the independent component can exhibit some non-stochastic signal of interference, which can be used to denoise the data [Pruim et al., 2015; Salimi-Khorshidi et al., 2014]. ICA seems also less sensitive to noise that SBA [Birn et al., 2008] and is efficient in the construction of group scaled functional networks [Cole et al., 2010]. However, ICA absence of spatial assumption is also a drawback. Indeed, once the functional networks is reconstructed, it can be difficult to determine which one corresponds to actual functional networks [McKeown et al., 2003]. As a corollary, ICA struggles with comparison between subjects [Van den Heuvel and Hulshoff Pol, 2010].

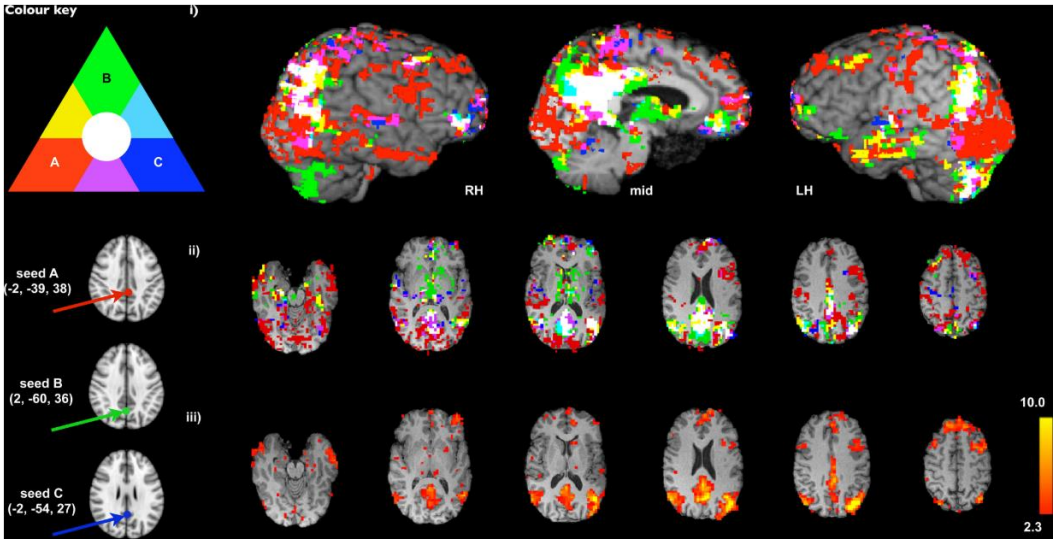

Figure 4.5: SBA robustness – Seed selection

Illustration is from [Cole et al., 2010]. Three different seeds from literature are used to estimate the default mode network, each one providing with either a red, blue or green map. The addition of colors exhibits the overlap between the estimation. Bottom line shows an ICA estimation. The difference in overlap shows limitation of SBA robustness. However, the three seeds provide satisfying detection of the DMN. As there is no truth is fMRI, it is difficult to confirm a seed as the best one.

4.8.5 Scaling - Number of functional networks

By cross-referencing the issues related to the qualification of functions, the number of ICA components, and the use of auxiliary information to select the seeds in SBA, a question is raised regarding the brain parcellation scaling in functional networks. The usual scale for the functional networks in rsfMRI is close to task-based fMRI functional areas. However, with ICA for instance, the number of estimated functional networks can either be set arbitrarily or be decided by a goodness of fit criterion (AIC, BIC, MDL…). Even with the same goodness of fit criterion, a cohort of subjects can have a wide range of estimated functional networks. On the one hand, too large/few functional networks would be prone to have a poor consistency, and on the other hand, too tiny/many functional networks would lead to computational complexity and poor functional discrimination [Cole et al., 2010; Kiviniemi et al., 2003; Varoquaux and Craddock, 2013]. In statistical terms, it is a matter of balancing with the dimensionality of the model (the size of functional networks) the within variance of functional networks, i.e. their intrinsic functional connectivity, and the between variance, which models their functional discrimination. The choice is illustrated below in Figure 4.6. Most typical networks are actually composed of distant but functionally connected areas, like for instance Broca's and Wernicke's area in language or left and right motor areas. It shows there is no optimal parcellation, because, regarding the functionality, networks can be composed of specialized subnetworks, even the DMN [Kernbach et al., 2018].

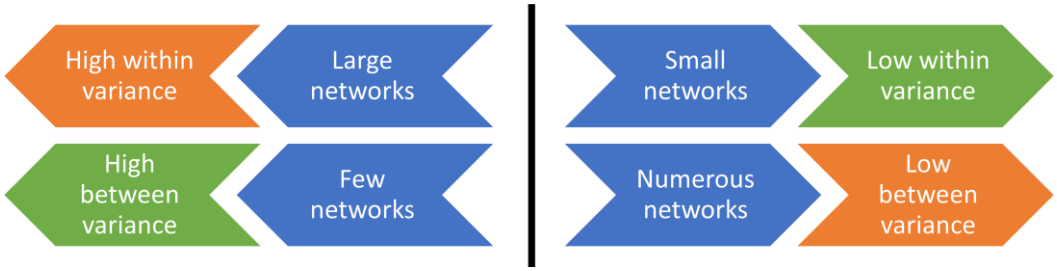

Figure 4.6: Model dimensionality balance

A low dimensionality (left) leads most likely to large and few networks. On the opposite high dimensionality leads to numerous small networks. As every model looks for low within variance and high between variance, a balance has to be found.

Chapter II.
The effect of scan duration in resting-state ASL

Section 5. Motivations

As discussed in Section 4 resting-state fMRI is an extremely rich topic to investigate. Sequences, denoising, registration, functional networks estimation, graph estimation, are all still open and active research fields. Regardless the field, the confidence given in a result usually increases with the amount of data confirming it. Adding subjects to a rsfMRI study is an intuitive way to increase the data volume. From a data analysis perspective, the amount of data can also be increased through the sample size of the observed population. In rsfMRI, which revolves around modeling the functional connectivity, one can consider the observed population is actually not directly the subjects, but instead the time courses of the voxels signals, on which correlations are estimated, ICA is implemented, etc. Hence, increasing the amount of data, i.e. the sample size, can also be increasing the number of time points in the signal, i.e. the *number of volumes*. For a given sequence, the number of volumes is proportional to the *acquisition duration*.

The acquisition duration is an essential practical parameter in a rsfMRI study. Most current rsASL studies operate with a duration from 8 min to 13 min and a TR from 3 s to 4 s (i.e. 120 to 260 images). Intuitively, one would assume the longer the duration, the better the sampling of the signal correlation (or any measure on signal) across the brain and thus the better the acquisition. But this requires to define what "better" acquisition actually means for rsfMRI and does not consider the practical questions of clinical implementation and subject resting-state upholding. Some papers already studied, directly or indirectly, the influence of duration in rsBOLD [Anderson et al., 2011; Birn et al., 2013; Bouix et al., 2017; Laumann et al., 2015; Termenon et al., 2016; Van Dijk et al., 2010]. However, it seems that in rsASL the question has not been addressed, at the time this manuscript is written.

In the second chapter, we address the effect of acquisition duration on the estimation of functional networks in resting-state ASL. We also focus on the feasibility of detecting functionally connected regions of the brain with rsASL. Indeed, ASL remains mostly an academic research field, and the contrast in resting-state between BOLD and ASL is even stronger. We remain as close as what a typical investigator of rsASL would experience, by implementing a usual sequence, typical processing and simple method for functional networks detection. We then assess a trend over the influence of duration on rsASL detected networks quality. We do not directly assess whether an acquisition is good at a given time, but rather how it evolves with longer durations. After describing the scores used and the modeling approach, an in-depth analysis for the Default-Mode Network (DMN) is presented in order to illustrate the scores evolution on the most typical resting-state network. Finally, we show results for all the functional networks under consideration and discuss an optimal acquisition duration for rsASL.

Section 6. Material

6.1 Subjects

Seven healthy male right-handed subjects aged from 21 to 28 years (23.5 ± 2.5) were involved in this study. All subjects gave informed written consent before participating in the study. We have maintained the homogeneity of the population in order to limit the influence of factors such as gender or age.

6.2 MR Acquisition

The subjects were scanned on a 3.0 T whole body Siemens MR scanner (Magnetom Verio, Siemens Healthcare, Erlangen, Germany) with a 32-channel head coil. MRI data acquisition was supported by the Neurinfo MRI research facility from the University of Rennes I. A 3D anatomical T1-weighted MP2RAGE image was acquired for each subject. Subjects were asked to keep their eyes closed, to relax (mind-wandering), to lie still and to not fall asleep[1].

Resting-state ASL sequence

The resting-state ASL imaging was performed using a 2D EPI pseudo-continuous (pCASL) sequence. As we mention in section 3.1.3, while 3D GRASE tends to outperform 2D acquisition, most investigator can only use 2D EPI as it is available on most MR device unlike 3D sequence [Alsop et al., 2015]. We try to stay in line with the literature for sequence parameters: FoV = 224 x 224 mm^2, TE = 12 ms, LD = 1500 ms, PLD = 1250 ms at the first slice. Volumes were made of 24 slices of 64x64 voxels, with 5 mm slice thickness and 20% gap for a total resolution of 3.5x3.5x6 mm^3. The MRI sequence is given in full in appendix. The number of volumes is 420 with TR = 3500 ms, for a total duration of 24 min 30 s.

For the PLD, the duration given for the first slice corresponds to 1712.5ms at the median slice. Shorter PLD, like 600 ms, seems to give a better functional representation [Liang et al., 2014, 2012; Viviani et al., 2011]. We kept the PLD quite long, close to the 1800 ms at the median slice, which is recommended by the white paper for best estimation of CBF [Alsop et al., 2015]. Indeed, the main advantage of ASL is ultimately to compute CBF although we will focus on functional areas representation in this paper.

[1] "Close your eyes, try your best to lie still, relax, do not think of something in particular, and do not fall asleep" – "Fermez les yeux, essayez au mieux de ne pas bouger, détendez-vous, ne pensez à rien en particulier, et ne vous endormez pas"

6.3 Data preprocessing

For each subject, the raw pCASL series is divided into 46 sub-series. The duration of these sub-series ranges from the closest possible to 2 min (34 volumes) to 24 min 30 s (420 volumes) with a time step of 30 s. For the sake of simplicity, we will only mention rounded durations hereafter. All these subdivisions are made before any preprocessing: the preprocessing is done independently on each sub-series. For the preprocessing steps and their parameters, we chose the most common ones found in bibliography. All steps are shown in Figure 6.1. For the preprocessing steps we used Matlab CONN toolbox[1] [Whitfield-Gabrieli and Nieto-Castanon, 2012].

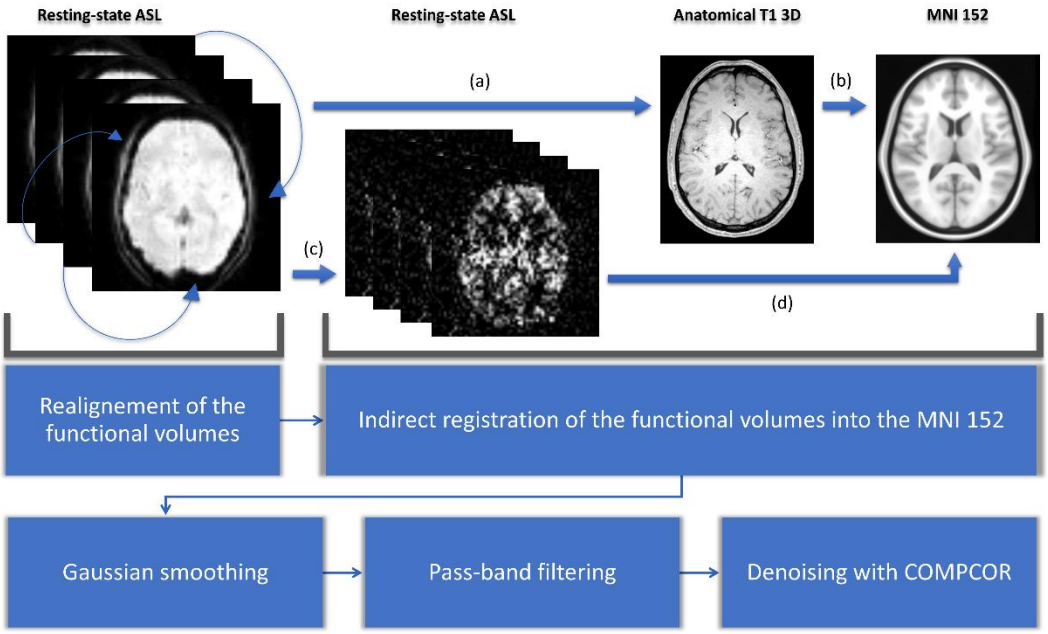

Figure 6.1: Preprocessing steps of the rsASL images

Preprocessing starts with the realignment of the perfusion weighted-map. All the functional volumes are registered with the first one. Second step is the indirect normalization of the functional volumes. It starts with registration of the functional data on the anatomical 3D T1 (a). Then the anatomical image is registered on the MNI 152 template (b). After a surround subtraction (c), transformations of (a) and (b) are composed to register functional data on the MNI template (d). We then used Gaussian smoothing with a typical 6 mm FWHM radius and pass-band filtering with a range from 0.005 Hz to 0.1 Hz. Final denoising was made with COMPCOR, using 5 regressors from WM, 5 for CSF and the 12 from the realignment [Behzadi et al., 2007].

[1] www.nitrc.org/projects/conn

Section 7. Modeling

7.1 Detecting networks with Seed-Based Analysis

To obtain the mapping of individual functional networks, we rely on seed-based analysis (SBA) [Van den Heuvel and Hulshoff Pol, 2010]. As we have seen in section 4.3, SBA is a very polymorphic modeling method, we will use its most common form in our work. Hence, we consider linear correlation as the similarity measure and use a set of 20 single voxels as seeds. Seeds are spread in the expected location of six usual functional networks: DMN, Sensori-motor, Language, Salience, Visual and Cerebellum. The exact positions of the seeds in the MNI152 space are provided in the appendix section and were suggested by the CONN toolbox. To build a functional map for each seed, we statistically test whether the signal between the seed and a candidate voxel is positively correlated with a risk of 1 % with FWER correction of Bonferroni. This is a tough conservative testing compared to most of rsASL (even fMRI in general) studies, but we agree with the recommendation of [Eklund et al., 2016] on false positive underestimation in fMRI literature, as we detail later in section 10.2.

7.2 Evaluation scores

The resting-state BOLD literature suggests extremely different best acquisition durations: 6 min [Van Dijk et al., 2010], 10 min [Bouix et al., 2017], 12 min [Birn et al., 2013], 25 min [Anderson et al., 2011], and even 100 min [Laumann et al., 2015]. [Termenon et al., 2016] focus on the tradeoff that can be made between duration and number of subjects in a group study. They give as reliable configuration from 14 min for 40 subjects to 7 min with 100 subjects. The main reason of their apparent discrepancy is the modeling. Indeed, there is many ways to properly define a model to assess the role of acquisition duration (a fortiori how much duration is enough), even if they lead to different conclusions.

As a pioneer work on rsASL, we want our modeling to reflect an investigator experience with the impact of acquisition duration on functional network estimation. Figure 7.1 illustrates the investigation of acquisition duration we will model. The DMN estimation is validated after 14 min on Figure 7.1 because it matches with how the functional network is expected to look like. In modeling terms, it is basically assessing the overlap of the estimated network with a reference network.

In order to investigate a trend afterwards and decide which acquisition duration is enough, the individual functional maps will be compared to a reference, like process described in Figure 7.1. For that purpose, we rely on the Multi-Subjects Dictionary Learning atlas (MSDL) by [Varoquaux et al., 2011]. MSDL is an atlas of 17 resting-state functional networks containing our 6 networks of interest, and from which our seeds are independent. The key idea is to have functional maps close to what an expert would expect to observe when looking for the typical functional areas investigated here. To study the quality of the detected networks as a function of the acquisition duration, we evaluate the overlap between the SBA estimated functional maps and the MSDL references (simply called "reference" hereafter) through two measures: the Jaccard's index and the area under curve (AUC).

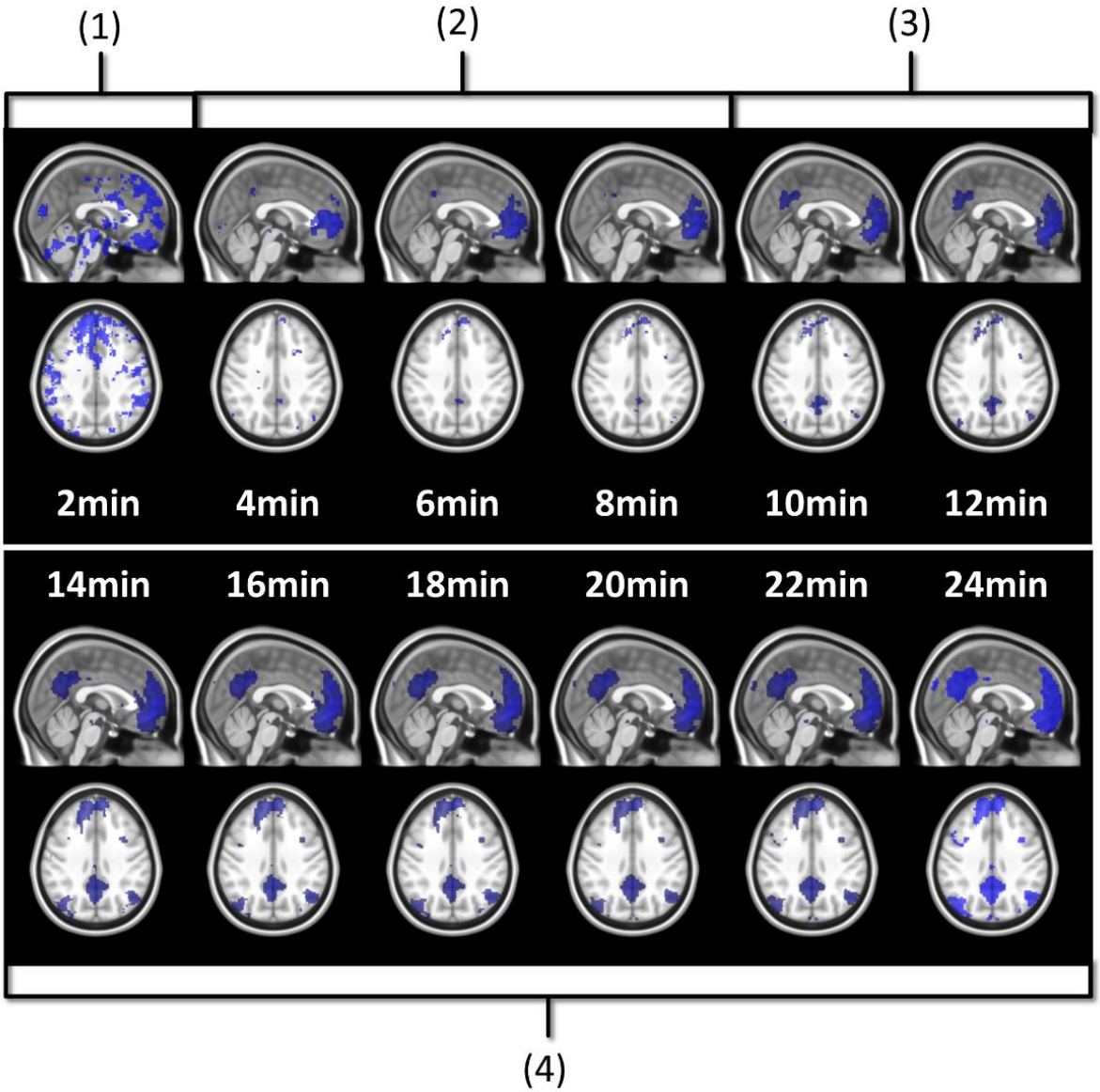

Figure 7.1: Seed-based estimation of the DMN with prefrontal seed

Four stages can be identified. At 2 min (1), the map shows only false positive noise detection. Between 4 min and 8 min (2), the false positive noise has disappeared while the frontal component of the DMN starts growing and the posterior starts being detected. Between 10 min and 12 min (3), the frontal component is well detected, the posterior grows and the lateral components are barely being detected. At 14 min and after (4), DMN detection is good and interestingly, stable.

Let $\mathbb{E}$ be a set, let $(v_i)_{i\leq k\in\mathbb{N}}$ be observations in $\mathbb{E}$ and $(M_1; M_2) \in \{0;1\}^{\mathbb{E}} \times \{0;1\}^{\mathbb{E}}$ binary categorical variables. Let A, B, C, D be four sets with respective cardinals a, b, c, d defined by:

$$\begin{cases} A \coloneqq \{v_i \mid M_1(v_i) = 1, M_2(v_i) = 1\} \\ B \coloneqq \{v_i \mid M_1(v_i) = 1, M_2(v_i) = 0\} \\ C \coloneqq \{v_i \mid M_1(v_i) = 0, M_2(v_i) = 1\} \\ D \coloneqq \{v_i \mid M_1(v_i) = 0, M_2(v_i) = 0\} \end{cases}$$

Almost all common similarity measures (Sokal's measures family, Sørenson-Dice, correlation etc.) can be defined with a, b, c, d. If one of the binary categorical variables can be considered as the truth, let's say M_2, therefore a becomes the number of *True Positives*, b of *False Positives*, c of *False Negatives* and d of *True Negatives*. We also trivially have the *Sensitivity*: $a/(a+c)$, *Specificity*: $d/(d+b)$, and the *Positive Predicted Value* (PPV): $a/(a+b)$. In fMRI, the v_i are the voxels (and not the subjects) and the variables M_1, M_2 are the functional maps to be compared. Note we defined the variable to as binary here, but the definition can easily be extended to probabilistic one.

7.2.1 Jaccard's index

When comparing two spatially distributed data, one of the most obvious measure is the Jaccard's index: the ratio between the size of their intersection and their union. It is defined by $J = a/(a+b+c)$ in our notation system. It provides intuitive and visual information about the overlap between one tested correlation map and one reference. It is also test-dependent: changing the risk or the multiple comparisons correction at the detection step will also change the shape and extent of the functional area, generally modifying Jaccard's index. This may be considered as a drawback but in fact, a statistical test is usually used at some point when investigating functional data.

7.2.2 Receiver operating characteristic analysis

In this section, we assume that the binary categorical variables are parameterized by at least one parameter. For example, in our case, it could be the risk for the statistical test of correlation α.

Let r be our parameter, a_r, b_r, c_r and d_r the previously defined cardinals now parametrized by r, and let define a set $\{(x(r), y(r)), r \in [-1;1]\} \subset [0;1]^2$ by:

$$\begin{cases} x(r) = 1 - \dfrac{d_r}{d_r + b_r} \\ y(r) = \dfrac{a_r}{a_r + c_r} \end{cases}$$

The implicitly defined function $f: x \longmapsto y$ is called the *Receiver operating characteristic curve* (ROC-curve) and its integral $\int_0^1 f(x)dx$ is simply called the Area Under Curve (AUC). In the case where M_2 is considered to be the truth, f is just very informally:

$$f: 1 - \text{Specificity} \longmapsto \text{Sensitivity}$$

The AUC has the interesting property to not be test-dependent, as it covers all possible values of the threshold parameter (i.e. risk/correlation). It illustrates how a functional map *can* be close to the reference by considering *all* values of the considered parameter, while the Jaccard's index reflects how it *is* close to the reference by considering *one* value of the given parameter. Hence AUC is a better way to assess the trend of interest from a *theoretical* point of view. However, it is further away from the *practical* proximity of the Jaccard's index modeling offers. We will eventually consider both scores.

7.3 Modeling trend with respect to the duration

Both Jaccard's index and AUC are computed for each subject, each seed, each duration and each functional network reference from MSDL. The next step is to model the trend of these two scores evolution according to the acquisition duration for all subjects and for each combination between one seed and one reference. Let us first check assumptions to select a suitable model. Assuming the rsASL sequence lasts long enough to cover all usage, extrapolation for a duration longer than 24 min 30 s seems superfluous. There is no theoretical model, even in BOLD, on the dependence between acquisition duration and quality of functional networks detection: we do not need an explicit formula. Even if the sub-acquisitions are processed independently, neighboring within-subject time-points estimated functional maps have a strong dependency as they come from the same acquisition. Under these conditions, a local non-parametric regression is very well-suited. We chose to use the LOESS[1] method. LOESS is a local polynomial regression on a subset of the whole dataset, the subset being defined by a weighted K-nearest neighbors' algorithm. For a more comprehensive description, see [Cleveland and Devlin, 1988]. We used second degree polynomial functions with a 0.8 span.

[1] The original name "Loess", is not an acronym but a reference to a geological structure [Cleveland and Devlin, 1988]. The acronym LOESS that stands for "locally estimated scatterplot smoothing", is however common. We use capital letters for easier reading.

Section 8. Results

8.1 How long is enough for the Default Mode Network?

In this section, we present an in-depth analysis of the DMN. In the set of 20 seeds we used, many should not be inspected when used in combination with MSDL DMN. The main reason is that most of the combinations has no objective basis for detecting the DMN. Otherwise, the seed may have failed to detect precisely the networks it was meant to detect, which is expected with very short acquisition duration. A simple way to get an idea of the quality of the overlap between the functional maps associated with a seed and a reference for all durations is to check the boxplots of the Jaccard's index as in Figure 8.1. Boxplots give an overview of the results for rsASL: hopefully for the DMN reference, Jaccard's indices have higher values for the seeds placed in order to detect it. Prefrontal and posterior seeds seem to work well while lateral DMN seeds provide lower scores but still higher than any other seeds. Figure 7.1 shows the evolution of the estimated DMN with the prefrontal seed and corresponding scores for one subject. The depiction made by the scores of the overlap between the estimation of the DMN and the MSDL reference match with the four stages identified in Figure 7.1 shows the Jaccard's index, AUC, Sensitivity and Predicted Positive Value (PPV), for each subject and at each acquisition duration. LOESS on Jaccard's index, as well as on AUC, models quite well what can be observed by looking directly at the functional map. Jaccard's index seems to stabilize after 12-13 min and AUC at an earlier acquisition duration around 9-10 min. We could have expected sensitivity and PPV to follow the same trend. Actually, sensitivity just grows over time, but more slowly for longer durations. Interestingly, PPV reaches a peak in the second stage mentioned above. The seven subjects show different level of response but good correlations (except for the subject 2 with AUC), i.e. the trend is the same among subjects, rather than an average effect induced by the LOESS. Moreover, results observed for the DMN, can be generalized for almost every combination of seeds and references as we will see.

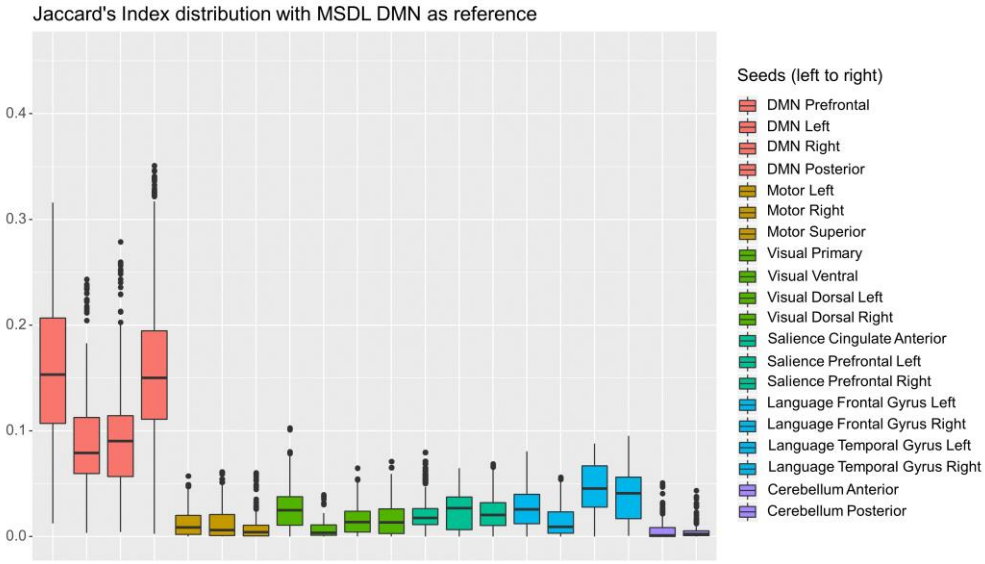

Figure 8.1: Distribution of Jaccard's index for the MSDL DMN

Each boxplot corresponds to one seed and shows the distribution of Jaccard's index between the estimated functional area corresponding to the considered seed on the one hand, and the MSDL DMN reference on the other hand, for all subjects and all durations. The seeds are grouped by color, each corresponding to one of the six functional areas considered. As expected, the seeds located in the expected DMN location (in pink) give the best results.

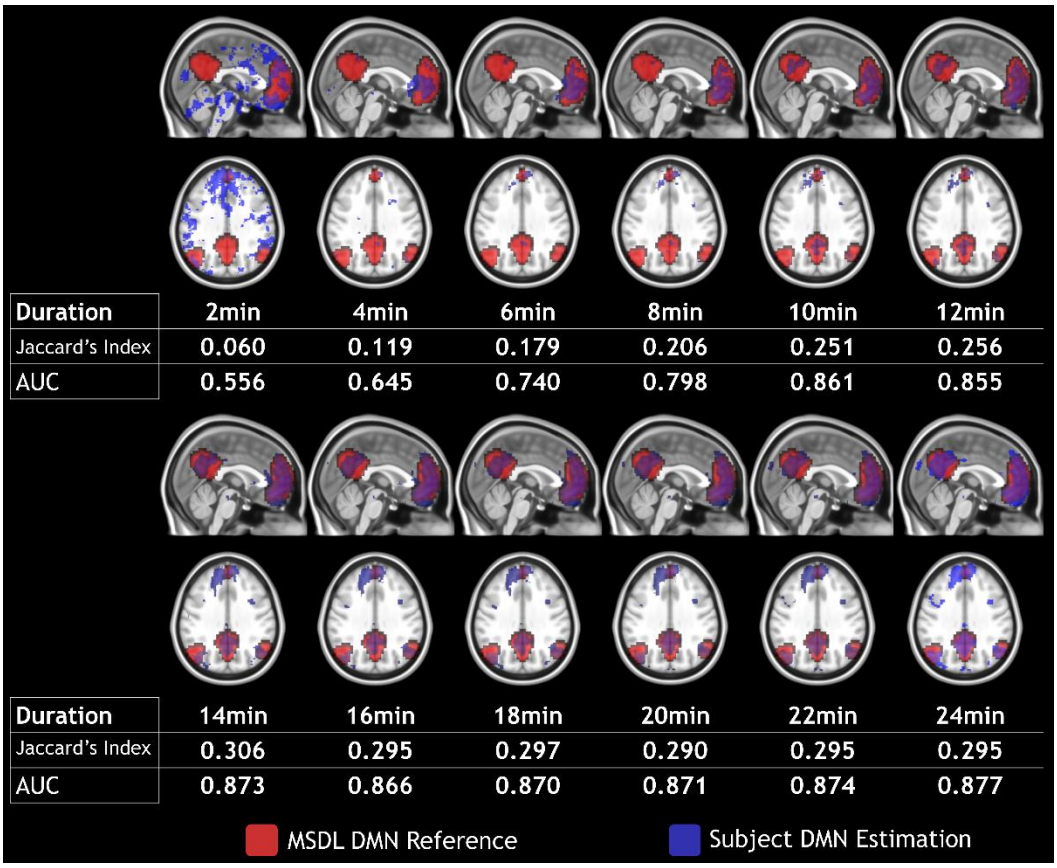

Figure 8.2: Evolution of scores with respect to duration for a DMN estimation

Subject 4 DMN detection (in blue) with prefrontal seed and MDSL DMN reference (in red) over a 2 min to 24 min duration with 2 min steps. Maps are shown in MNI152 space.

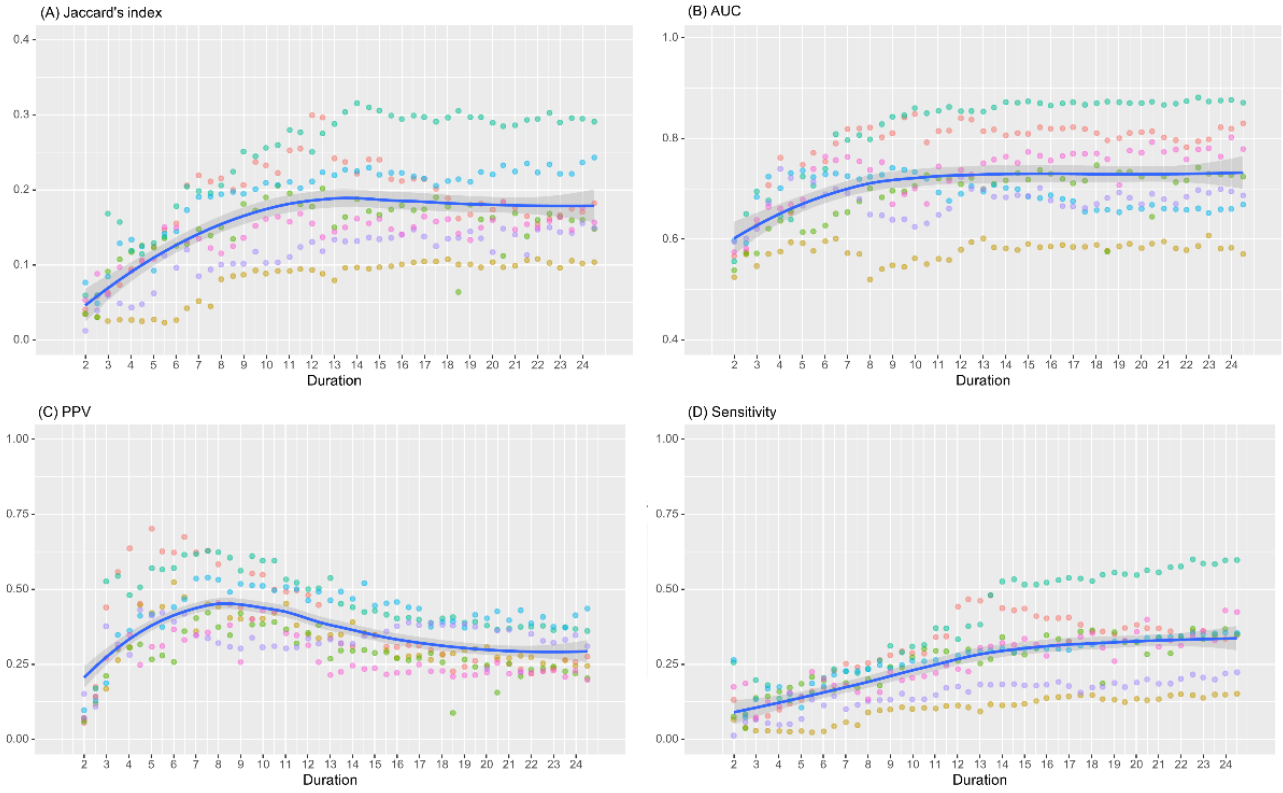

Figure 8.3: Scores evolution with respect to acquisition duration for the DMN

Jaccard's indices (A), AUC (B), Positive Predicted Value (C) and Sensitivity (D) evolution with time with their associated Loess for the seed associated with prefrontal DMN. On all subjects, Jaccard's index increases with duration before 10-12 min, then stabilizes. The AUC shows the same trend with an earlier stabilization, around 9-10 min. PPV grows rapidly, reaches a peak at 8 min, then decreases slowly. Finally, Sensitivity increases with time, but more slowly for longer durations. Subjects show different level of response but globally good correlations between each other.

8.2 How long is enough for all the networks?

8.2.1 Seeds selection

Visual inspection of the acquisition data and of the estimated functional networks estimation is an efficient quality control [Power, 2017]. However, with more than 6000 functional maps generated (20 seeds, 7 subjects, 46 acquisition durations), a visual inspection of all the maps is not practicable. As seen for DMN, many combinations between seeds and references should not be investigated since they are not functionally meaningful and will yield to very low overlapping scores (e.g. prefrontal seed with visual cortex). For Jaccard's index, we selected combinations for which at least 50% of observations have $J \geq 0.1$. For AUC, the median is also considered, with this time a threshold of 0.7. These thresholds on the median values may seem rather low, but let us remember that all the acquisition durations are considered, even the shortest ones. Figure 8.4 shows the median values for all the combinations between seeds and references. The two thresholds lead to an almost identical choice for the selection of combinations. All seeds have their best scores with the expected reference, and each of the six functional networks are considered to be sufficiently well detected with SBA for Jaccard's index in accordance with our selection rules. The AUC suggests as good enough one more seed for cerebellum but consider that salience is not detected well enough with our set of seeds.

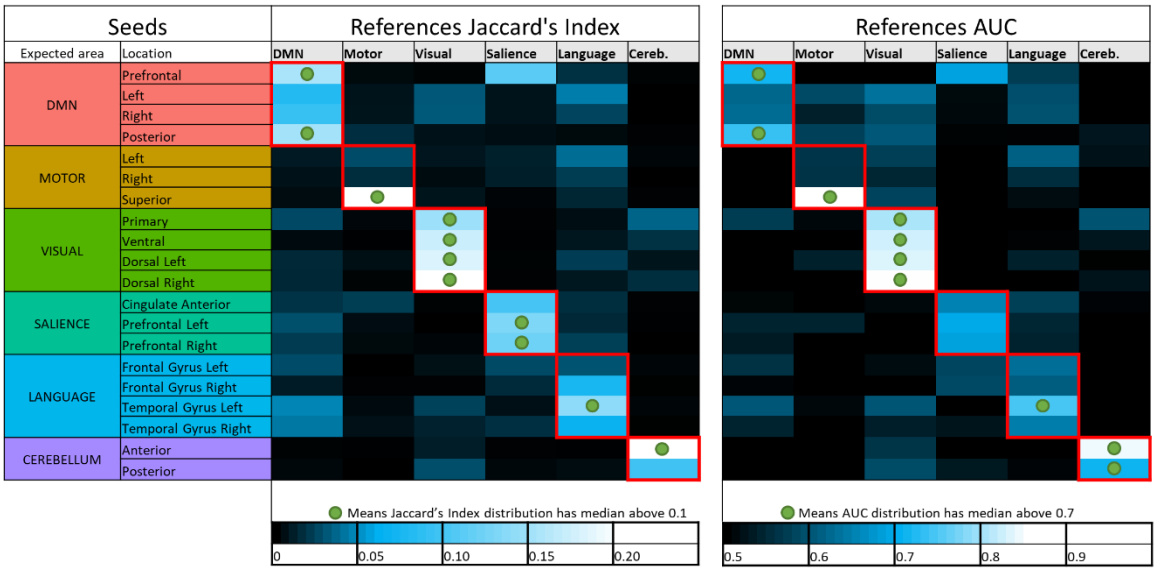

Figure 8.4: Seeds selection

Median values of Jaccard's indices and AUC for all combinations of seeds/references. Green circles show where seeds/reference combinations are selected with respect to our thresholding rules (0.1 for the Jaccard median and 0.7 for the AUC median).

8.2.2 LOESSs colormaps

Figure 8.5 shows the range of durations where scores are not significantly different from their maximum values (5% risk) for each selected reference/seed combination. Colors on heatmap are scaled between minimum and maximum values of the corresponding score and matches with the stages already described for DMN in the previous section. Indeed, for every combination between seeds and references, both scores rapidly increase, and start to stabilize after a certain duration. However, for both measures, the 95% confidence interval around the maximum suggests a later start in the stabilization than suggested directly by the LOESS curve values. While some combinations scores look already stabilized at 12 min, almost all of them are close to their maximum value at 16 min. Figure 8.6 shows a collection of functional areas obtained at a duration of 14 min. While language seed struggles to detect spatial components far from the seeds, all the other ones provide good detection of expected functional networks.

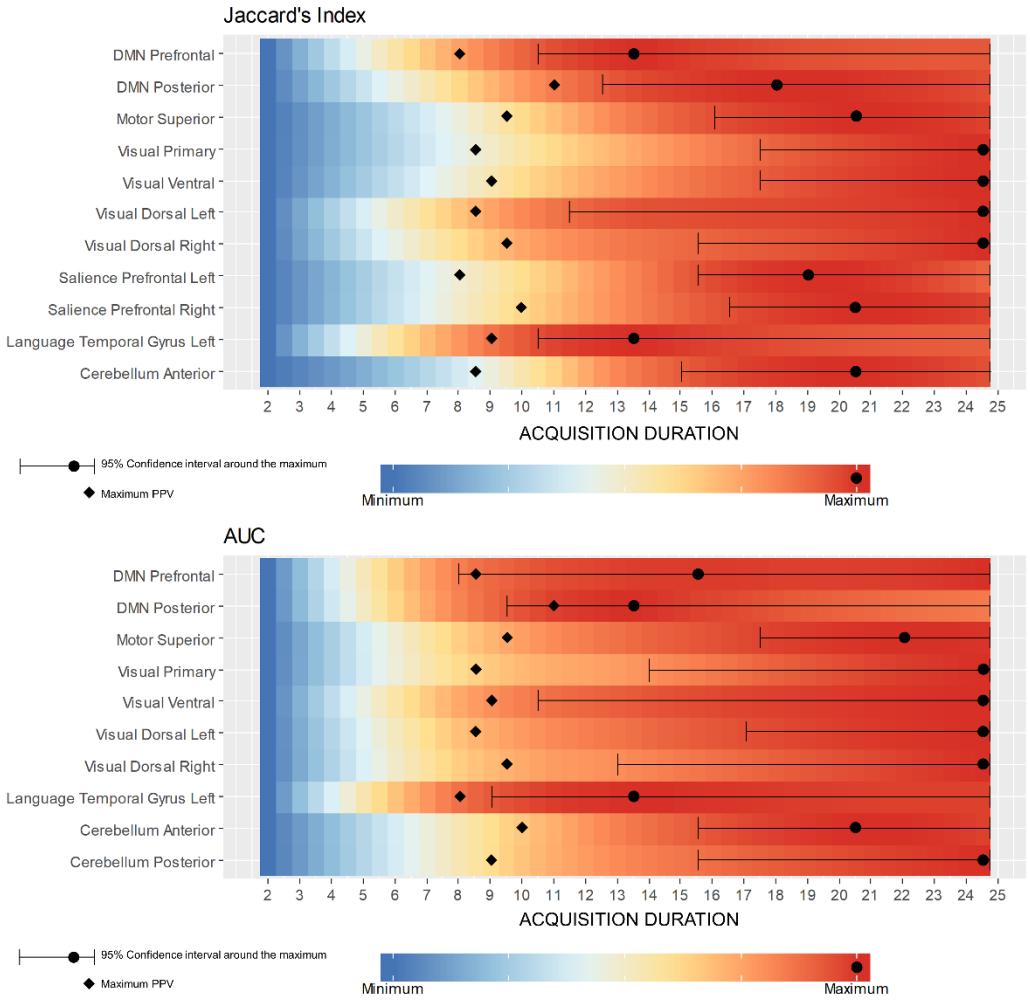

Figure 8.5: LOESSs colormaps for all selected seeds and corresponding references

This figure shows the range of durations where scores are not significantly different from their maximum values (5% risk) for each selected reference/seed combination. Colors on heatmap are scaled between minimum and maximum values of the corresponding score and matches with the stages already described for DMN in the previous section. Indeed, for every combination between seeds and references, both scores rapidly increase, and start to stabilize after a certain duration. However, for both measures, the 95% confidence interval around the maximum suggests a later start in the stabilization than suggested directly by the Loess curve values. While some combinations scores look already stabilized at 12 min, almost all of them are close to their maximum value at 16 min.

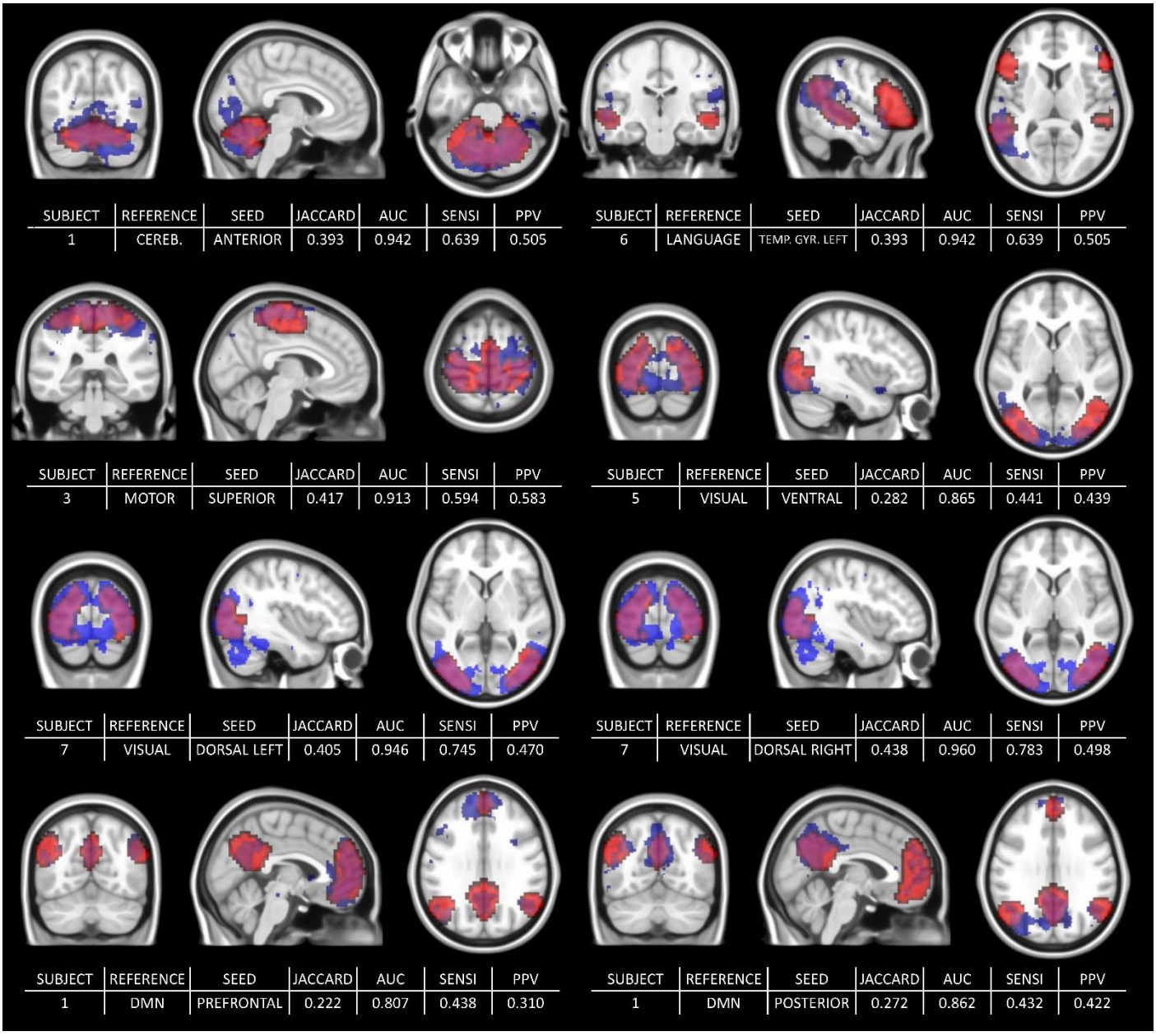

Figure 8.6: Collection of functional areas obtained at 14 min of acquisition

While language seed struggles to detect spatial components far from the seeds, all the other ones provide good detection of expected functional networks. The two bottom rows show the same subjects and the same reference, but estimated through with different seeds. The visual seeds show an extremely good robustness in this case.

Section 9. Discussion and conclusion

9.1 ASL feasibility

Our two objectives were to confirm the feasibility of resting state ASL and to evaluate the influence of the acquisition duration on the estimation of functional areas. Figure 7.1 and Figure 8.6 with corresponding scores in Figure 8.4 and in Figure 8.5 confirm that, even with the basic preprocessing and straightforward methodology we used, ASL is fully viable as a resting-state method.

9.2 Acquisition duration

Regarding the impact of acquisition duration, the most important result is the stabilization of the functional areas representation after a certain duration for both measures, Jaccard's index and AUC, with a strong inter-subjects correlation (i.e. not a mean-effect induced by the LOESS modeling). Since the acquisition should have the shortest duration possible for clinical implementation, the recommended duration eventually corresponds to the start of the stabilization stage. Strict definitions of the stabilization stage lead to longer duration since they would rely heavily on the LOESS maximum by considering as stable just a narrow interval around of the maximum. However, since after 12 min to 14 min the score variations are low, a slight change in preprocessing or in the population could also lead to unstable maximum, without changing the trend. Relaxed definitions would keep optimal duration stability, but they may consider a functional area as good enough when a human investigator would not. Actually, early stages of acquisition are associated with poor representation of functional areas disconnected from the seed. Based on our different results, 14 min seems to be an interesting compromise.

9.2.1 A posteriori definition of stabilization

Since all LOESS share similar tendency, a better definition of the start of the stabilization would basically be the preimage of the maximum curvature point of the LOESS curve. In order to identify it, we suggest a simplified Multiple Adaptative Regression Splines (MARS) model, where the position of the only node of the regression will define the optimal number of volumes.

$$\hat{y} = a.x.\mathbb{1}_{x \leq L}(x) + a.L.\mathbb{1}_{x>L}(x)$$

Equation 9.1: Simple MARS model to estimate optimal number of volumes

For every L, $\hat{y}$ is a least squares estimator since it is a simplified MARS: we just enforce the power of the predictors to 1 and 0. We could build a whip model by allowing the degree of first monomial to be free, and constrain the node to be at least a C^1 junction in order to well-define the curvature of node and hence better modeling the maximum curvature of the LOESS. However, the increasing complexity of the model seems superfluous considered we do not need that much accuracy in the estimation of the optimal number of volumes. In order to select L, we would like to avoid the demanding computation of automatic node selection algorithm such as the Myopic or Fullsearch [Ruppert, 2002]. Since the model is extremely simple and not demanding in computation, we can exhaustively compute the regression for a wise set of L, given a certain precision in number of volumes, let us say between 20 and 50.

9.3 Methodological considerations

In order to estimate functional networks, the two most common methods are SBA and Independent Component Analysis (ICA). We did not work with ICA because the association between independent components and functional areas of the brain is intrinsically tedious, as we mentioned in section 4.8.4 [Cole et al., 2010; McKeown et al., 2003], especially when it comes to comparison between subjects. Moreover, in order to investigate the relationship between quality and duration for all subjects, we must estimate the functional areas in the same way for each subject. Indeed, keeping the same seeds and the same test for SBA is trivial, while keeping the same number of independent components is equivocal, since it should be decided by a goodness of fit criterion.

We chose to report the positive predicted value rather than specificity for two main reasons. On the one hand, true negatives can have multiple definitions in fMRI, since it depends on the voxels considered: the whole volume, only the brain or any smaller ROI like grey matter. Although it is logical to consider only brain voxels for functional activity, this implies an extremely high number of true negatives, since the volume of a functional network is ten to a hundred times smaller than the one of the whole brains. Therefore, the specificity reaches values too high to provide relevant information on similarity between functional areas. On the other hand, like specificity, PPV plays a similar role with respect to sensitivity: specificity gives a complementary information to sensitivity in the totality of voxels whereas PPV gives a complementary information in the union of the reference and the estimated functional area.

Note that the DMN, the sensori-motor cortex, and the cerebellum have an almost consensual spatial definition among the authors, unlike language, visual and salience, which show a greater spatial variability (see for example http://neurosynth.org/). As we provide an evaluation only with one set of references (from the MSDL), one could have expected this to be a limitation of our work. However, the spatial variability of the areas of interest in atlases is low enough to change only the scores but not the trend observed in this paper.

Preprocessing influence should also be considered as positive: since we use typical and basic preprocessing, more advanced techniques should provide the same or an earlier stabilization, still keeping our suggestion as a sufficient duration. The same is true for ASL readout approach. Using a 3D readout is probably an improvement with respect to our sequence, as it tends to provide higher SNR compared to 2D EPI, but not every investigator has access to 3D sequence [Alsop et al., 2015].

9.3.1 Duration and number of volumes

Since we are studying the influence of acquisition duration for a given set of parameters, the optimal duration of 14 min could be strongly influenced by the sequence parameters. Although the influence of each of them is to be kept in mind, most of them have a specific bibliography that goes well beyond the issue of the optimal acquisition duration, as we see in section 3.1. However, two of them may have a deep impact on our results: post-labeling delay and repetition time (TR). As mentioned in section 6.2, we already have some clues on how the PLD can influence functional networks representation. The critical

parameter in our opinion is repetition time. It defines the sample frequency of the resting-state signal and turning our 14 min suggestion into 240 volumes since we only work numerically on the signal.

Its variation may shift the stabilization step toward a higher/lower number of volumes and hence a longest/shortest duration, without changing the stabilization of the functional networks representation after a certain number of volumes (i.e. same signal but different sampling frequency).

Moreover, in rsASL, TR values are typically between 3 s and 5 s, which is too wide to assume the locally linear dependence between TR and optimal duration. As a preliminary work on optimal duration in rsASL, we focus more on the modeling rather than investigating the influence of the TR. However, a specific study on the relationship between repetition time, number of volumes and quality of acquisition as [Wu et al., 2014] did for BOLD, would be, in our opinion, highly beneficial to better define the optimal duration and also would be useful when an investigator sets up a sequence.

9.3.2 Influence of internal parameters

Last, we work on a homogeneous sample of subjects. While it greatly limits the influence of variables related to the population description and not included in our modeling, it also narrows the population represented by our sample of subjects. Hence, a natural perspective is to include new subjects in order to extend the population represented and checks if the influence of variables like gender, age, laterality could be excluded from the population variability. It should be noted that geriatric, pediatric and pathologic populations should be treated separately rather than included. Indeed, these populations can show extreme differences in average (or local) perfusion, which possibly hinders the functional networks estimation, and hence, when the stabilization starts.

9.4 Conclusion

We model and process data in order to get results as close as an investigator would do. All the considered functional areas were well detected by rsASL. Our results show a quality stabilization after a certain number of volume/duration for both scores in all but one combination between seeds and references: very long sequences should not hence be considered. While we can suggest, for our set of sequence parameters, the optimal number of volumes of 240 / optimal duration of 14 min, any methods that improves the detection of functional networks are likely to provide an earlier stabilization start, i.e. optimal number of volume/duration. Since we use a basic and typical sequence, preprocessing and estimation, 240 volumes / 14 min even if not optimal should be enough for most rsASL usage. Last, the exploration of the impact of the TR and PLD on the optimal acquisition duration was beyond the scope of this article but would be highly beneficial for sequence implementation, since we forecast they are the two parameters that may be able to shift the stabilization start toward higher number of volumes.

Chapter III.
Resting-state ASL performance compared to resting-state BOLD

Section 10. Motivations and problematic

10.1 Motivation

In the previous chapter, we focused on a dual objective: confirming ASL as a viable method to detect functional networks in resting-state and investigating the effect of scan duration. As mentioned in the state of the art, ASL remains mostly an academic research field. As BOLD is the gold-standard technique for functional MRI, assessment of ASL performance involves a comparison with BOLD at some point. The objective of this part of the manuscript is to perform this comparison. Firstly, we benefit from the methodological framework we developed when investigating ASL alone, and adapt it to rsBOLD data. In a second stage, we will discard the third-party atlas used in this framework as a reference for functional networks and directly compare rsASL and rsBOLD data through various scores.

10.2 Methodological consideration

Before going any further, we would like to point out some considerations regarding the comparison between rsASL to rsBOLD. From a statistical point of view, each functional network estimation is an individual of a big dataset. On these individuals, we want to investigate the influence of factors on quantitative variables, for instance if the variable "diseased" has an effect on a score measured on the functional networks. In the last chapter, we discussed issues in regards to the comparison of ICA-based functional networks between subjects. What was appropriate for comparing subjects is still valid when comparing the two modalities. Since we want now to consider the modalities, we simply add to our dataset the functional networks estimated from BOLD, and a new categorical variable with two levels: ASL and BOLD. The question that actually stands is: what is the influence of the factor "modality"?

In order to capture the influence of the factor "modality", the idea is to limit at best the influence of other potential confounding factors, source of uncontrolled variability. The standard method is to work on the same cohort of subjects, as it greatly reduces the inter-subject variability. In order to at least ease the comparison ASL and BOLD, and at best avoid influence of external factors, the most important method is probably to use the exact same method of functional networks estimation. Under methods, we include preprocessing steps and parameters associated to preprocessing as we have seen in section 4.8.2. We also include functional connectivity modeling, and parameters associated, especially those that are used as threshold. For instance, Figure 10.1 illustrates how the significance level of a statistical test and the multiple comparison correction have a deep impact on the size and consequently the shape of estimated functional networks. Besides the obvious impact on the size of functional networks, it also shows, by extension, how confusing the comparison of functional networks can be, when they have not been estimated through the same method. While the lack of multiple comparisons correction (case [A] in the figure) would actually be a terrible mistake, Eklund et al. report that 40 % of fMRI studies do not even report using one [Eklund et al., 2016]. We will give careful attention to these considerations in our comparison between ASL and BOLD.

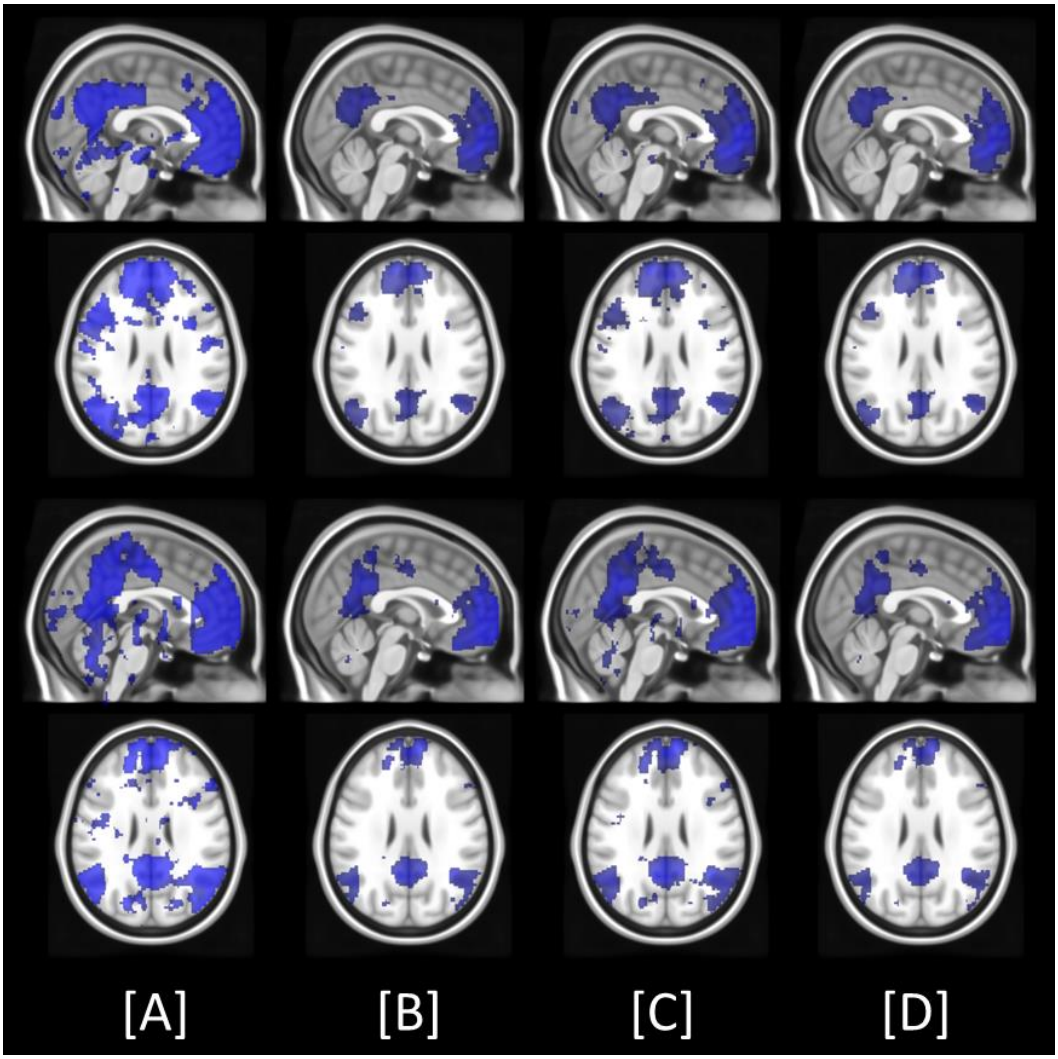

Figure 10.1: DMN estimation through different statistical test parameters

All estimations are made on the same subject with 274 volumes (16 min of ASL, 6 min 23 s of BOLD) through SBA with the seed in the prefrontal cortex. The top two rows show ASL estimations of the DMN and the bottom two rows show BOLD estimations. Each column shows estimations computed with different test parameters for a canonical test of correlation, such as:

[A] $\alpha = 1\%$ with no multiple comparison correction

[B] $\alpha = 5\%$ with FWER correction

[C] $\alpha = 1\%$ with FDR correction

[D] $\alpha = 1\%$ with FWER correction

It shows how even the usual statistical testing can deeply impact the estimation of functional networks, and by the way, how difficult it can be to compare networks.

Section 11. Comparing ASL and BOLD using MSDL references

The first comparison of ASL and BOLD can naturally be made using the methodological framework we developed in Chapter II. Its application on rsBOLD data is quite straightforward as, beside the ASL volumes subtraction, each processing step can be shared between ASL and BOLD. We first investigate an optimal scan duration for BOLD, in number of volumes or in minutes.

11.1 Material and methods

11.1.1 MR acquisition

The rsBOLD acquisition were performed on the same cohort of 7 subjects, with the same 3.0T scanner from Neurinfo MRI research facility. The acquisitions were performed right after the rsASL one with the exact same resting-state instruction: eyes closed, without moving, and without performing particular cognitive task.

11.1.2 Resting-state BOLD sequence

The resting-state BOLD imaging was performed using a 2D EPI sequence with following parameters: FoV = 192 x 192 mm^2, TE = 30 ms, TR = 1400 ms. Volumes were made of 24 slices of 64x64 voxels, with 4 mm slice thickness and 50% gap for a total resolution of 3x3x6 mm^3. The MRI sequence is given in full in appendix. The number of volumes is 514 for a total duration of 11’48 min.

11.1.3 Data preprocessing

As we mention in previous section 10.2, in order to limit sources of variability in the comparison between ASL and BOLD, we must apply as close as possible preprocessing to rsBOLD data as rsASL ones. Fortunately, besides the ASL volumes subtraction, the preprocess of rsASL and BOLD can be shared, as we detailed in section 4.2. Figure 11.1 below details the preprocessing we use. As rsASL data, the raw rsBOLD data are divided into sub-series before any preprocessing. One first set contains 21 sub-series of duration ranges from the closest possible to 2 min (88 volumes) to 11 min 48 s (514 volumes) with a time step of 30 s. The second set contains 23 sub-series with number of volumes equal to the number of volumes of rsASL sub-series that corresponds to each minute between 2 min and 24 min of rsASL. E.g. 10 min of rsASL corresponds to 171 rsASL volumes, hence the second set of rsBOLD has a sub-series of 171 volumes.

11.1.4 Networks detection

In order to detect the functional networks, we implemented a common form of SBA for rsASL. As for preprocessing, our SBA trivially adapts to rsBOLD: we use the exact same set of twenty seeds, the linear correlation as similarity measure and statistically test whether the signal between the seed and a candidate voxel is positively correlated with a risk of 1 % FWER-corrected.

11.1.5 Evaluation scores and modeling

We keep the same overlap scores, Jaccard's index and AUC, and the MSDL atlas is also used as a set of functional networks reference. In order to discard seeds that are not able to effectively detect their corresponding network, we use the same empirical criterion: for Jaccard's index, we select combinations between seeds and MSDL for which at least 50% of observations have a Jaccard's index above 0.1, and for AUC above 0.7. In order to model the evolution of scores with respect to the scan duration, we also use the non-parametric local regression LOESS with second order polynomial and a span equal to 0.8.

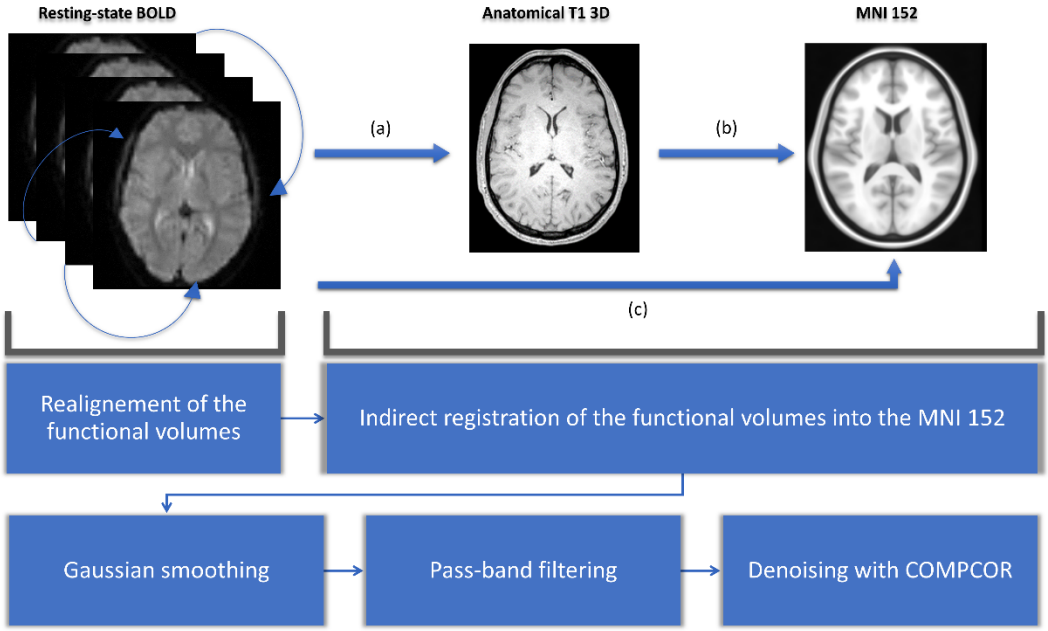

Figure 11.1: Preprocessing steps of the rsBOLD images

Besides the subtraction of ASL volumes, we used the same preprocessing as for rsASL. It starts with the realignment of the volumes to the first one. The second step is the indirect normalization of the functional volumes. It starts with the registration of the functional data on the anatomical 3D T1 (a). Then the anatomical image is registered on the MNI 152 template (b). The transformations of (a) and (b) are composed to register functional data on the MNI template (c). We then used Gaussian smoothing with the same 6 mm FWHM radius as ASL and the same pass-band filtering with a range from 0.005 Hz to 0.1 Hz. Final denoising was made using COMPCOR [Behzadi et al., 2007], with the same parameters as for ASL.

11.2 Results for BOLD only

Both set of rsBOLD sub-series are used in this section to investigate the effect of scan duration on rsBOLD data. On the set of twenty seeds used, two are discarded by the both Jaccard's index and AUC criterion: the language frontal gyrus right seed and the language temporal gyrus right seeds. The criterion on Jaccard's index discard the cerebral posterior seed, and the criterion on AUC discard the salience prefrontal left seed. Figure 11.2 shows heatmaps of scaled values of Jaccard's index and AUC LOESS between minimum and maximum, with respect to the seeds considered effective by both criteria. Figure 11.2 also shows the range of durations where scores are not significantly different from their maximum values (5% risk) for each selected reference/seed combination.

Globally, both scores have a fast increase at start until 3 min of acquisition duration, and most reach stabilization after a certain duration. However, Jaccard's index and AUC start behave differently just after 3 min. Most Jaccard's index LOESSs reach close value to the maximum value earlier than AUC, where LOESSs after 3 min keeps increasing very slowly. Providing an optimal duration in BOLD depends a lot on the definition of stabilization. First, Jaccard's index suggest earlier values than AUC, and with strict definition of stabilization, AUC stability is harder to assess as maximum LOESSs values are reached close to the maximum duration.

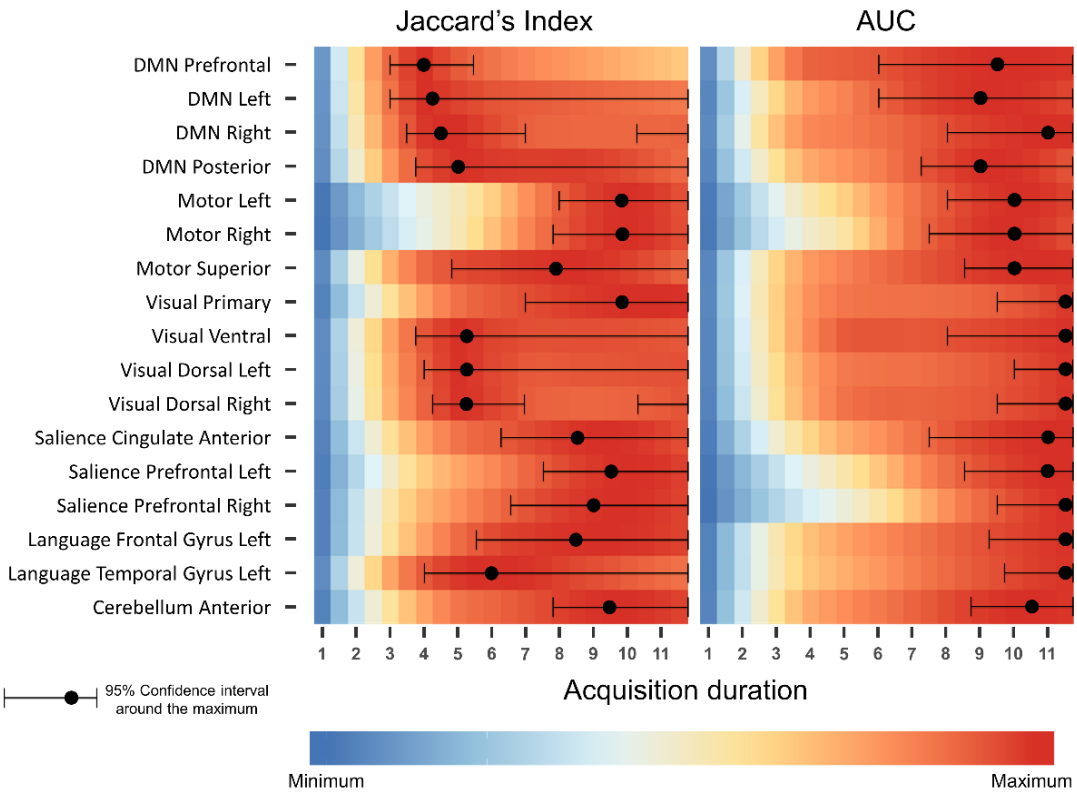

Figure 11.2: LOESSs colormaps for all selected seeds and corresponding references for rsBOLD data

Colors on heatmap are scaled between minimum and maximum values of the corresponding score. Almost all combinations have an early fast-increasing score. While variations of score behave quite similarly between AUC and Jaccard's index, AUC LOESSs have slower increasing scores compared to Jaccard's index after 3 min.

11.3 Comparison of ASL and BOLD

To best extract the influence of the modality factor, we have to compare functional networks with as many variables as possible in the same state. One of these variables is actually critical: the size of the sample of data used to estimate the functional networks. In rsfMRI context, the sample size for functional networks estimation is the number of volumes and not the acquisition duration. Even though comparing images with the same acquisition duration is appealing, mostly because we want eventually to conclude on an optimal duration in minutes, a direct and careless comparison is actually a methodological pitfall. To illustrate this point, let us consider an estimation A made with two techniques 1 and 2, and name them A1 and A2. If A1 is better than A2, but A1 has been estimated with a larger sample size than A2, one cannot assume the technique 1 is better than 2. From this section onwards, we will compare ASL and BOLD in terms of the number of volumes.

11.3.1 Boxplots – Seeds response

A first assessment can be made through the distribution of overlap scores with MSDL references of each modality with respect to the seeds and the scores. To his end, we simply constructed boxplots in our rsASL investigations (Figure 8.1). One boxplot was associated with a combination of one seed with one MSDL reference network, and showed the distribution of the score for all subjects and all number of volumes for this combination. Figure 11.3 and Figure 11.4 extend the construction and add a dependence to the modality. Hence, for each combination of seed and reference we have now a pair of boxplots, noted A for ASL and B for BOLD. Figure 11.3 and Figure 11.4 show first that according to our seed selection criterion (a median above the black dotted lines), more seeds are considered to be able to provide an effective detection of the corresponding expected networks (17 for BOLD vs 11 for ASL). Besides cerebellum seeds, ASL shows slightly lower Jaccard's index than BOLD. The stars and N.S correspond to the result of a Mann-Whitney test, such as the p-value is below 0.001% for three stars, below 0.01% for two stars, below 0.05% for one star, above 0.05% for N.S. The boxplots corresponding to AUC are given in appendix, and lead to the same conclusion: ASL is more likely to fail to detect the expected networks and provides slightly lower overlapping scores with MSDL atlas. Censoring the data by removing the acquisitions with low number of volumes (likely corresponding to failed detections) increases globally the scores, but the results remain the same: detections of functional networks seems easier in BOLD.

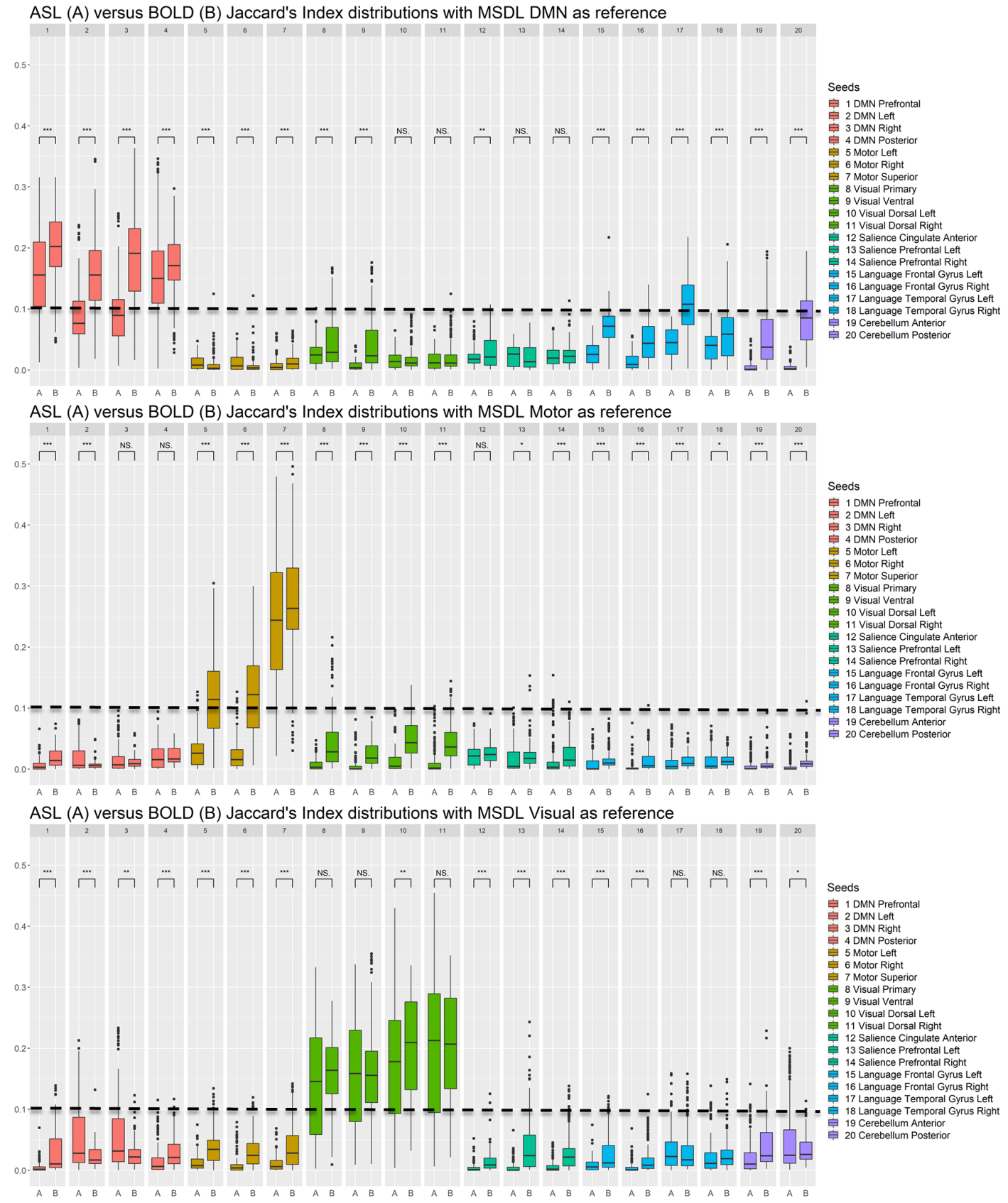

Figure 11.3: Distribution of Jaccard's index with respect to the MSDL reference, the seeds and the modality, 1st part

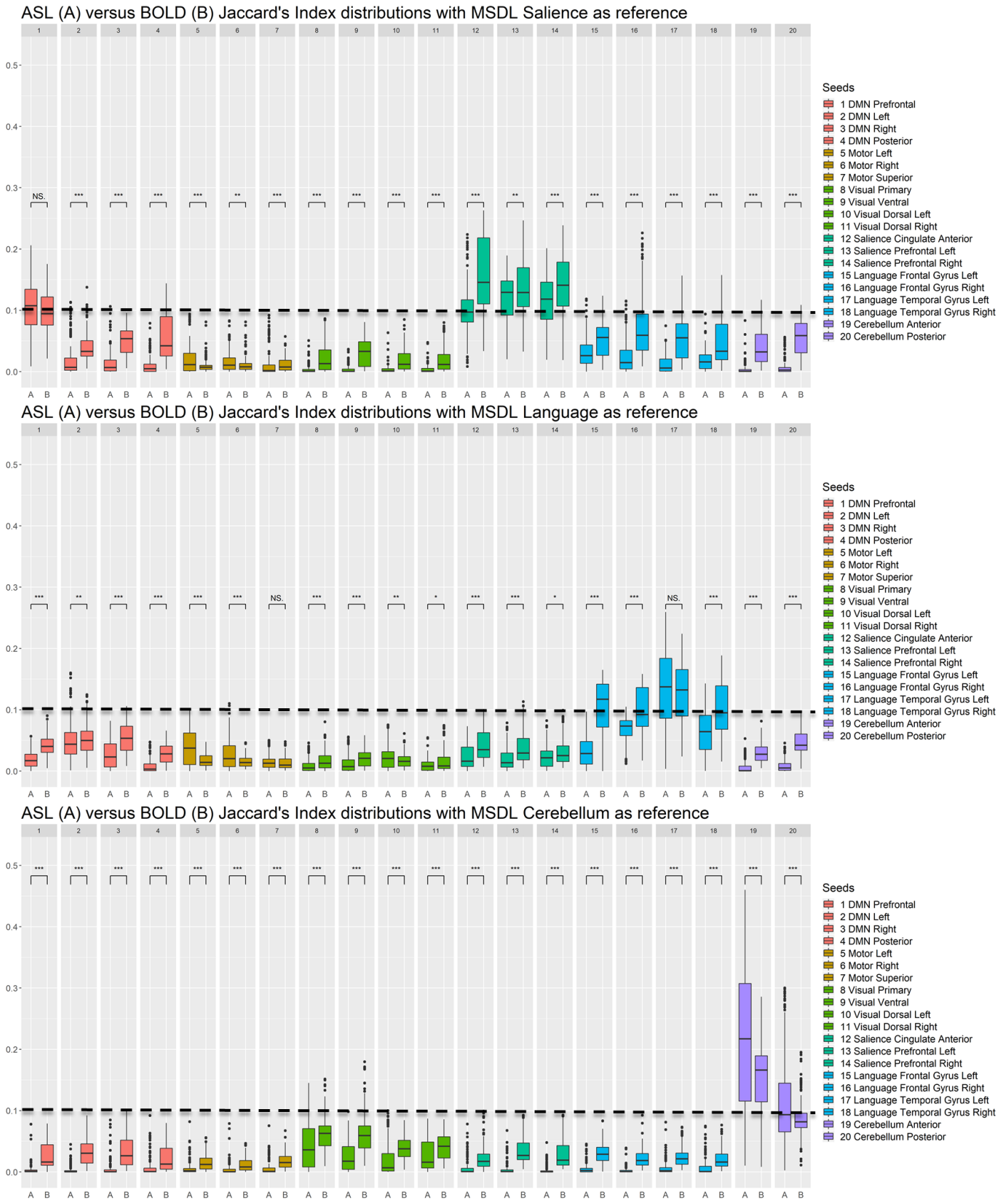

Figure 11.4: Distribution of Jaccard's index with respect to the MSDL reference, the seeds and the modality, 2nd part

11.3.2 LOESSs Colormaps

Figure 11.6: Color maps of Jaccard's index LOESS values with respect to the number of volumes for all reference/seed combination. Figure 11.5 and Figure 11.6 below are extended version of the color maps shown in section 11.2 dedicated to BOLD and in section 8.2 dedicated to ASL. In these figures, the colormaps are shown with respect to the number of volumes (the sample size) and scale scores values between minimum and maximum values. Uncolored lines show seeds that are considered to not have been able to detect their corresponding expected network, according to our criterions.

The key result is actually, as Figure 11.5 and Figure 11.6. show, that the colormaps are quite homogeneous, whether between scores as we see in previous sections or more importantly between modalities. Indeed, in most seeds the scores reach 50% of their maximum values before 100 volumes, and all before 125. Then, for most seeds, AUC and Jaccard's index keep growing slowly, and after 250 volumes, scores barely change.

11.3.3 Conclusion

Overall, the detection of networks seems easier in BOLD as more seeds manage to provide satisfactory estimation of functional networks. Both MSDL overlap scores (Jaccard's index and AUC) are slightly better in BOLD than in ASL. However, as MSDL is an atlas built from rsBOLD data, it could bias the overlap scores of rsBOLD. A stabilization stage can also be observed with BOLD. However, the variance of rsBOLD results are larger: LOESSs are less correlated between and within scores compared to rsASL results. Consequently, it is harder in BOLD to precisely define a start of the stabilization stage as AUC clearly suggest a higher number of volumes, no matter the definition of stabilization considered. If we use the same considerations as in ASL that leads to 240 volumes, the range of value for stabilization start are for BOLD between 250 and 290 volumes. Converted to minutes with ASL TR = 3.5s and BOLD TR = 1.4s, it suggests 14 min for ASL and 6-7 min for BOLD. As we discuss with ASL, these values depend a lot on where to consider that the stabilization have started.

Regarding the rsBOLD, others studies have suggested different values for duration/number of volumes: 6 min/60 vol. [Van Dijk et al., 2010], 10 min/250 vol. [Bouix et al., 2017], 12 min/275 vol. [Birn et al., 2013], 25 min/750 vol. [Anderson et al., 2011], and 100 min/2700 vol. [Laumann et al., 2015]. [Termenon et al., 2016] focus on the tradeoff that can be made between duration and number of subjects in a group study. They give as reliable configuration from 14 min/1200 vol. for 40 subjects to 7 min/580 vol. for 100 subjects. Each paper assesses the effect of acquisition duration in rsBOLD differently: comparison to networks obtained from longest acquisition [Bouix et al., 2017], connectivity between region of interest [Birn et al., 2013], reproducibility [Anderson et al., 2011; Laumann et al., 2015], scoring on graph properties [Termenon et al., 2016]. Hence, because of the different modeling, it is hard to say either our suggestion is in line with literature or not, notwithstanding the different sequence and preprocessing. The different quality assessments are not a drawback however, as each paper and our work explore different aspects of the impact of the number of volumes.

As discussed for rsASL, the conversion of number of volumes into minutes, through the TR parameter, seems to be of prime importance as a further area of investigation. In rsBOLD the TR has already been shown to be able to impact estimation considering a fixed number of volumes [Wu et al., 2011], but for rsASL a specific investigation of TR in combination with the number of volumes in rsfMRI would be highly valuable in the topic.

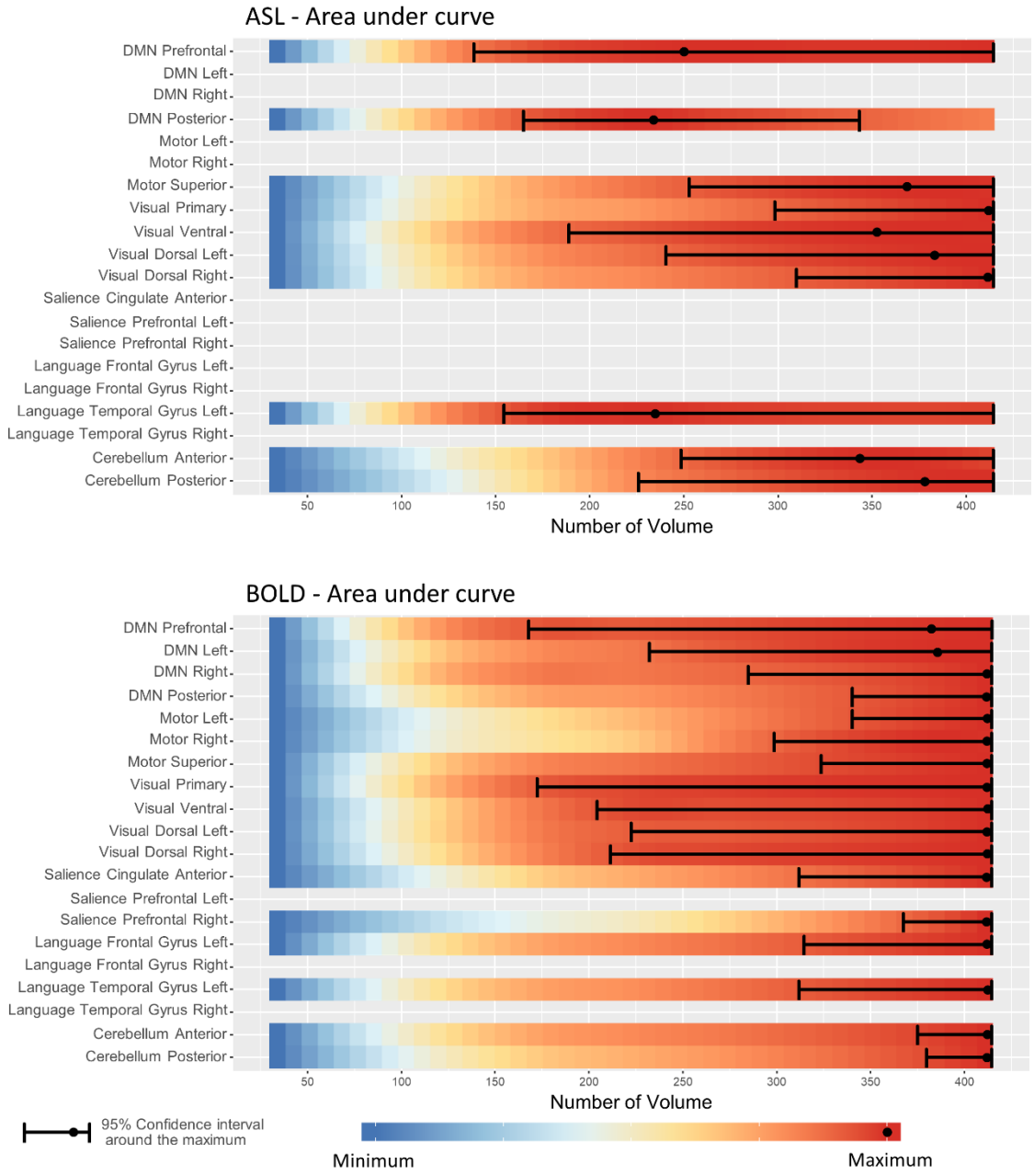

Figure 11.5: Color maps of AUC LOESS values with respect to the number of volumes for all reference/seed combination.

Top figure is built with ASL data, and bottom with BOLD. The absence of color for a seed denotes a failed detection, according to the criterion median of AUC above 0.7.

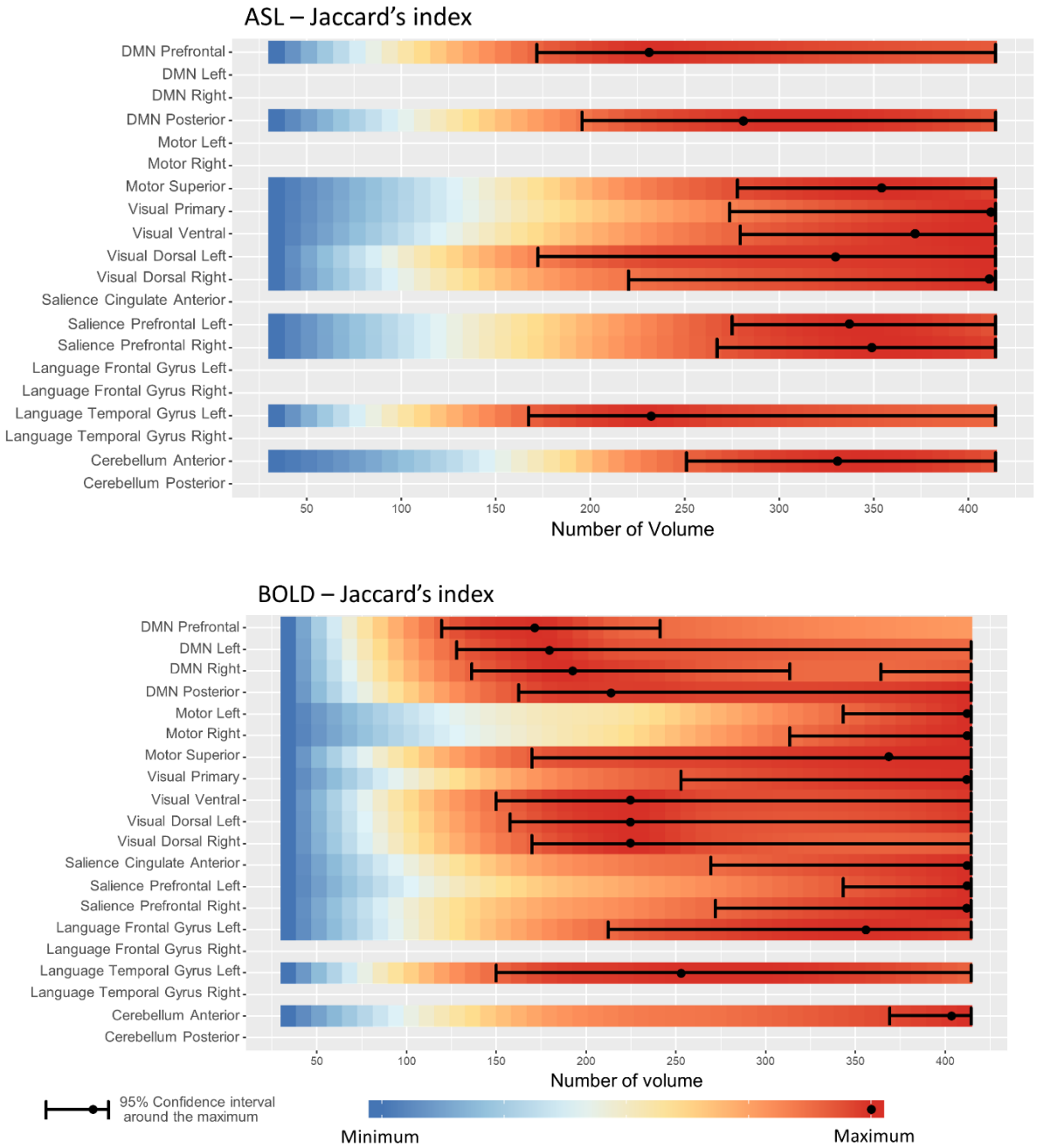

Figure 11.6: Color maps of Jaccard's index LOESS values with respect to the number of volumes for all reference/seed combination.

Top figure is built with ASL data, and bottom with BOLD. The absence of color map for a seed denote a failed detection, according to the criterion median of Jaccard's index.

Section 12. Comparing ASL and BOLD without a reference

12.1 Foreword

Most of the work in this section has been made during an international mobility of the author in the Brainnetome center of the Institute of Automation in Beijing. The author is deeply grateful towards Pr. Yu and his colleagues whose insightful comments and encouragement made possible to conduct this research.

12.2 Motivation

In the previous sections, comparisons were made using the MSDL references. Our ansatz was to use a gold-standard beforehand in order to propose a model close to visual investigation of resting-state data. Using the MSDL instead of another atlas seems to have a limited impact when assessing the start of functional networks stabilization. However, BOLD scores (Jaccard's index and AUC) are slightly better than ASL, despite a higher within-variance of the scores. An obvious hypothesis is that since MSDL atlas comes from BOLD data, it may give BOLD a decisive advantage in the comparison. To check this assumption properly, one should test if BOLD still provides with better scores when compared with different atlases that come either from BOLD and ASL data, notwithstanding the hypothesis that ASL and BOLD functional networks are different. However, there is no resting-state ASL atlas of functional networks to the best of our knowledge. Last, we want to directly compare ASL and BOLD without using a third-party dataset of references because besides the assumption of references neutrality toward modalities, it also obviously limits the ways to compare ASL and BOLD to the scoring of overlaps with such references. In the next sections, we compare the rsASL data and the rsBOLD data without third-party atlas on the basis of 4 criteria: the number of active voxels, the functional networks tissue distribution, their intrinsic functional connectivity and last, the spatial correlation between corresponding rsASL and rsBOLD networks.

12.3 Number of active voxels

12.3.1 Preliminary remarks

The number of active voxels is defined as the number of voxels that are part of an estimated functional networks. This is a straightforward measurement of the size of functional networks. However, this measure should be used carefully when comparing ASL to BOLD, especially if we do not check some conditions beforehand.

First of all, ASL and BOLD functional networks should be expressed in the exact same voxel space, which is our case (MNI 152). Secondly, number of active voxels should be computed only for successful detection of functional networks. We will keep the criterion we used for Jaccard's index in section 7.1 to select which estimation should be kept. Thirdly, in order to compare number of active voxels, estimation of functional maps must be estimated through comparable methods. This is a typical case where analysis using a statistical test should be built carefully: number of active voxels is critically dependent on the threshold used to build the functional network from the functional connectivity map (threshold on the map of correlation with a seed in our case). This threshold is almost every time defined by a statistical test using a risk corrected for multiple comparison testing, which is itself dependent on the sample size (the number of volumes in our context). Comparing ASL and BOLD functional networks estimated through different test, sample size, threshold etc. is arguable since the difference could be explained mostly by the methods used and not by the acquisition modality as we see in Figure 10.1. The key idea is basically to avoid introducing the strong influence of new factors we can control easily into the assessment of the comparison, in order to be able to exhibit as well as possible the only influence of the factor of interest. In our case, we have fortunately been able to check all these conditions.

Final point, the number of active voxels seems a not very relevant score, as just comparing size of networks without additional information seems pointless. However, it can be useful for discussing other measurements on functional networks. Moreover, in fMRI, ASL is known to be more "specific" than BOLD, and BOLD more "sensitive" than ASL [Barker et al., 2013]. It is then expected that BOLD will provide higher number of active voxels. Even if by the visual inspections we made we already confirm our functional networks check this proposition, we can also quantify this difference, and above all, check how the difference of the number of active voxels between ASL and BOLD evolves with respect to the number of volumes.

12.3.2 Results

Figure 12.1 shows evolution of the number of active voxels for both modalities with respect to the number of volumes. We show only the two most extreme cases in term of difference between ASL and BOLD number of active voxels as the influence of the seed is actually pretty limited. Moreover, we are more interested in the relative difference between ASL and BOLD rather than the absolute values. As expected, BOLD has a higher number of active voxels compared to ASL. This seems less obvious below fifty volumes, but let us remember that with such low numbers of volume, functional networks estimation has most likely failed. We can note that even if with higher number of volumes,

the difference between ASL and BOLD is almost stable, the ratio is decreasing since both ASL and BOLD have higher number of active voxels. These results are similar to [Zhang et al., 2018], who also used number of active voxels in order to compare resting-state ASL to BOLD with 130 volumes acquisitions. We can also note that the size of the functional network estimation can greatly increase with number of volumes (almost double between 150 and 300 volumes).

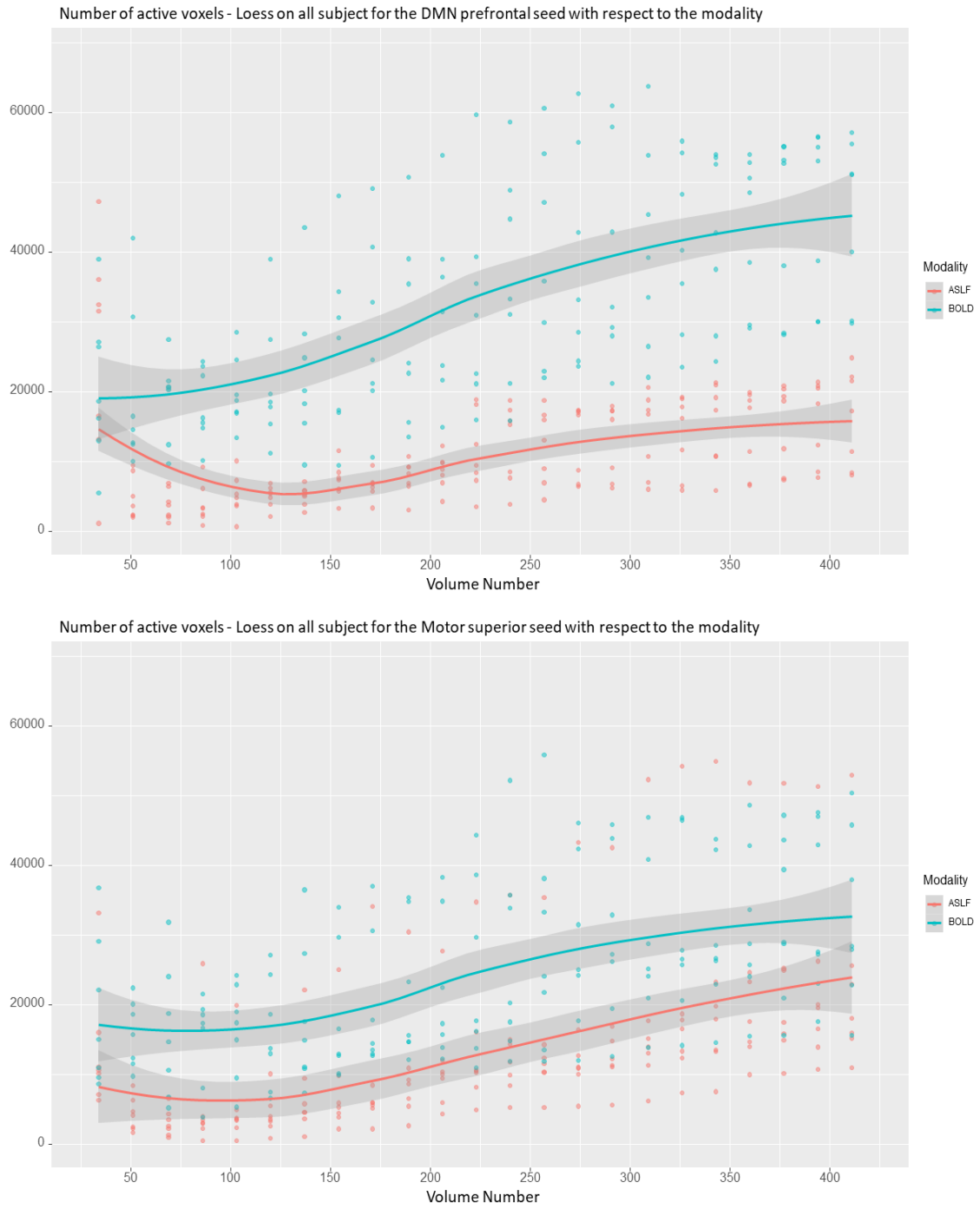

Figure 12.1: Extreme cases for the number of active voxels

Both graphs show LOESS estimation of the evolution of the number of active voxels with respect to the number of volumes. Each dot corresponds with one subject's functional network estimation. The grey area is the 95% confidence interval of the LOESS. Top figure shows the results for the seed in prefrontal DMN, where the difference of number of active voxels between ASL and BOLD is maximum, and bottom figure shows the results for the motor superior seed where the difference is minimum. In both extreme cases BOLD has always more active voxels. Since the difference is pretty stable after 150 volumes, the ratio is decreasing with higher volumes number.

12.4 Functional networks tissues distribution

12.4.1 Motivation

In section 11.3, regarding the overlap with MSDL references, we show that even if ASL and BOLD functional networks spatial extent share similar behavior with respect to the number of volumes, there was still a difference regarding both overlap scores (Jaccard's index & AUC). The large difference between ASL and BOLD sensitivity, actually suggest a strong difference in functional networks shape (volume) between ASL and BOLD. The investigation on number of active voxels in previous section shows that estimated BOLD networks can be three times bigger compared to ASL networks. With such wide differences, it is natural to investigate next the functional networks composition between the three major brain components: grey matter (GM), white matter (WM) and cerebrospinal fluid (CSF). Indeed, functional brain activity is mostly located in the cerebral cortex. Hence it is envisioned for our estimated functional networks to be mostly composed of GM to be considered as a satisfying detection [Logothetis et al., 2001]. While voxels in CSF should be obviously considered as real false-positive, it is not the case for WM. Indeed, WM may have some functional role, as some study have exhibited white matter specific networks [Gawryluk et al., 2014; Peer et al., 2017].

12.4.2 Results

Figure 12.2 shows the detailed composition of the functional networks. Figure 12.3 shows some descriptive values on the mean composition of functional networks. Results are both interesting and not. Mainly, no matter if this is GM, WM or CSF, the percentage distributions are globally extremely homogeneous with respect to three aspects of interest: the modalities, the seeds, the volumes number. Firstly, even if most modalities pairs of estimated networks with respect to the seeds show a statistical significative difference, this is purely informative as the difference is not large enough to clearly discriminate ASL and BOLD functional networks. Secondly, Figure 12.2 shows the composition of functional networks is independent from the seed, expect maybe for the motor area (GM, WM, CSF) and Cerebellum (GM). Their difference in composition between ASL and BOLD is a bit more obvious, but with a median difference still below 10%. Last, BOLD interquartile range is smaller than ASL. However, the interquartile range is still below 5% for almost every boxplot. Since we include every estimation, it also shows that the impact of the number of volumes is purely anecdotal.

It is a bit surprising that even with such huge difference in size between low/high number of volumes and between modalities, the composition of estimated functional networks remains very stable. Regarding estimation that have most likely succeed, i.e. with enough volumes, the composition was expected, may be not with that much similarity. However, for estimation that have most likely failed, i.e. with low number of volumes, it seems that the signal of the seeds (located in GM) do not correlate with pure random noise as the composition is still the same. If the composition we found characterize functional spontaneous activation, then low volumes estimations could also match with the clustering of tiny regions having spontaneous activation happening at the same time. However, since the time range is narrow, only few have happened. Hence, while it matches with functional connectivity definition, the limited number of spontaneous

activations is not sufficient to define a consistent functional network. As we point in section 4.1.3 spontaneous activation is easier to detect around a frequency of 10^{-2} Hz. Hence, with low number of volumes (<80), if we assume the SBA exhibit a functional signal because of the tissue distribution, the correlation with the seeds probably only rely on very few activations. Since these activations are random, the few volumes estimations are not repeatable, invalidating this way the status of functional networks. The functional connectivity demands similar neural activation *pattern*, and pattern require a certain number of simultaneous activations.

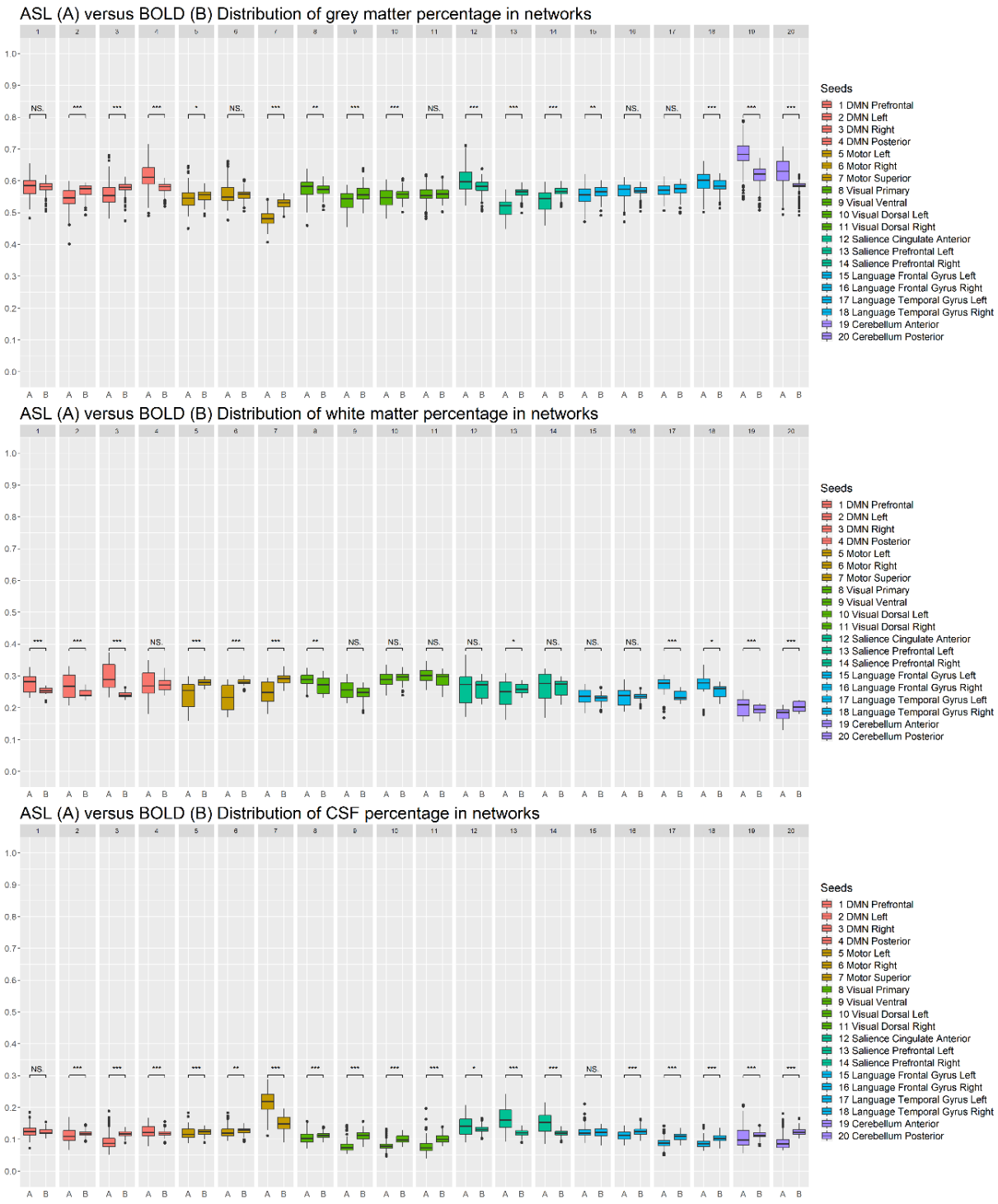

Figure 12.2: Distributions of functional networks composition

Boxplots showing GM, WM and CSF percentage distribution of estimated functional networks with respect to the modality (A stands for ASL, B for BOLD) and with respect to the seed (top numbers). The decomposition is extremely homogeneous, whether it is with respect to the seed or the modalities. Even if statistical testing shows numerous significative differences, this is purely anecdotal since differences are too narrow to discriminate the modalities given a functional networks tissues distribution.

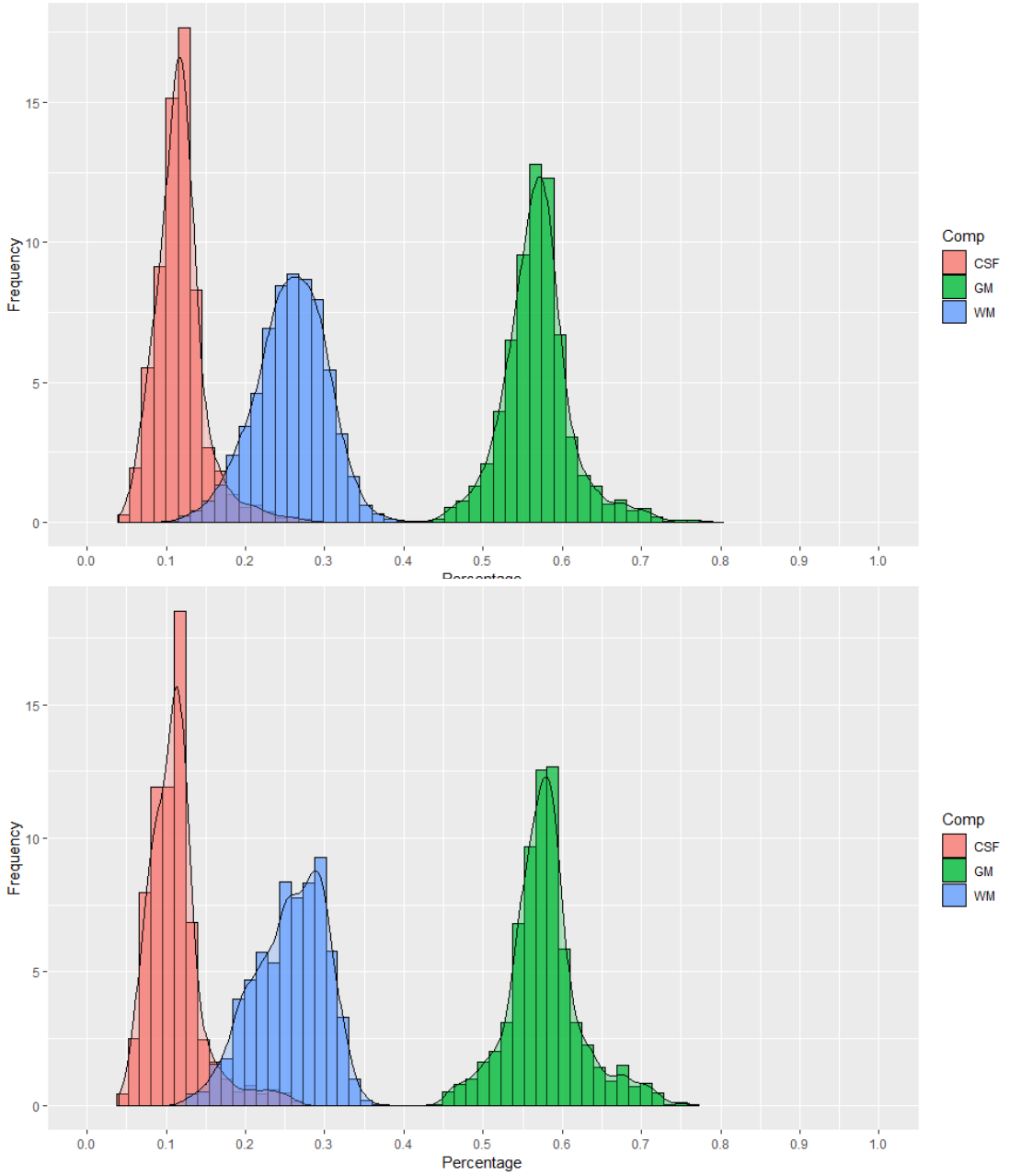

Figure 12.3: Histograms and estimated probability density function of composition percentage

Top shows the average distribution for all estimated networks. Bottom shows the distribution for the same subset define by the Jaccard's index criterion. The difference is barely noticeable, showing that even if we consider only the best detection, the composition of estimated network is not improved (less CSF, more GM). The mean composition is roughly 58 % of GM, 27 % WM, 12 % CSF in both cases.

12.5 Intrinsic functional connectivity of the functional networks

12.5.1 Introduction

As we mention in section 4.8.5, we can interpret the construction of functional networks as a statistical clustering, which exhibit the issue of functional networks scaling: a balance has to be found between minimizing the variance within clusters (small networks) and the variance between clusters (few networks). Since we are not partitioning the brain by working on a set of 6 typical networks, we can compare the estimated rsASL and rsBOLD networks with their variance within. To this end, we focus on networks intrinsic functional connectivity (IFC): the distribution of the linear correlation between voxels signal inside networks.

12.5.2 Results

We consider only the seeds that provide successful detection for both ASL and BOLD according our criterion in section 8.2.1. Figure 12.4 and Figure 12.5 show four mean distribution of linear correlation for all functional networks corresponding to a valid seed, for all subjects, and estimated with four different number of volumes, respectively: 51, 154, 257, 360. It corresponds to durations in rsASL of 3, 9, 15, 21 min, and in rsBOLD of 1’11, 2’24, 6, 8’24 min. Table 12.1: shows mean of networks IFC with respect to the seeds for estimation made with 257 volumes. The role of the seeds seems limited. The BOLD intrinsic connectivity is always weaker than ASL. While it is difficult to qualify the nature of the signal that seeds gather at low number of volumes, the intrinsic connectivity there has still an extreme discriminative power. With higher number of volumes ASL and BOLD the difference is less strong.

We show in previous section 12.4 that the tissues distribution of the functional networks is extremely homogeneous between modalities. Hence, the difference in intrinsic connectivity cannot be explained this way. We know with section 12.3, that BOLD functional networks volume is roughly twice higher compared to ASL. Moreover voxels can belong to multiple functional networks and functional networks as units are not independent from each other, as a consequence of their small-world organization in graph theory [Liang et al., 2014; Wang et al., 2010]. Even using tough conservative statistical testing [Carp, 2012; Eklund et al., 2016], the high sensitivity of BOLD compared to ASL is probably still prone to gather voxels that show an intermediate functional connectivity with two different functional networks in both of these networks. In other words, BOLD high sensitivity limits its discriminative power. Some literature also suggest that typical functional networks such as the DMN can also be subdivided into more sub-specialized functional units [Bzdok et al., 2015; Kernbach et al., 2018; Leech et al., 2011]. As BOLD captures more of this sub-specialized units compared to ASL, if we assume that ASL functional networks are roughly included in BOLD one, then it is natural that the within variance (hence the intrinsic connectivity) of ASL networks can only be similar in worst case, or better in general case than the BOLD ones. This case is a cluster pruning issue we describe in section 4.8.5 about scaling: we can improve the within variability of BOLD clusters at the cost of the model complexity, for the sub-division of actual networks make sense functionally speaking. However, we already use tough conservative parameter in our modeling, and moreover, we use the exact same modeling for ASL.

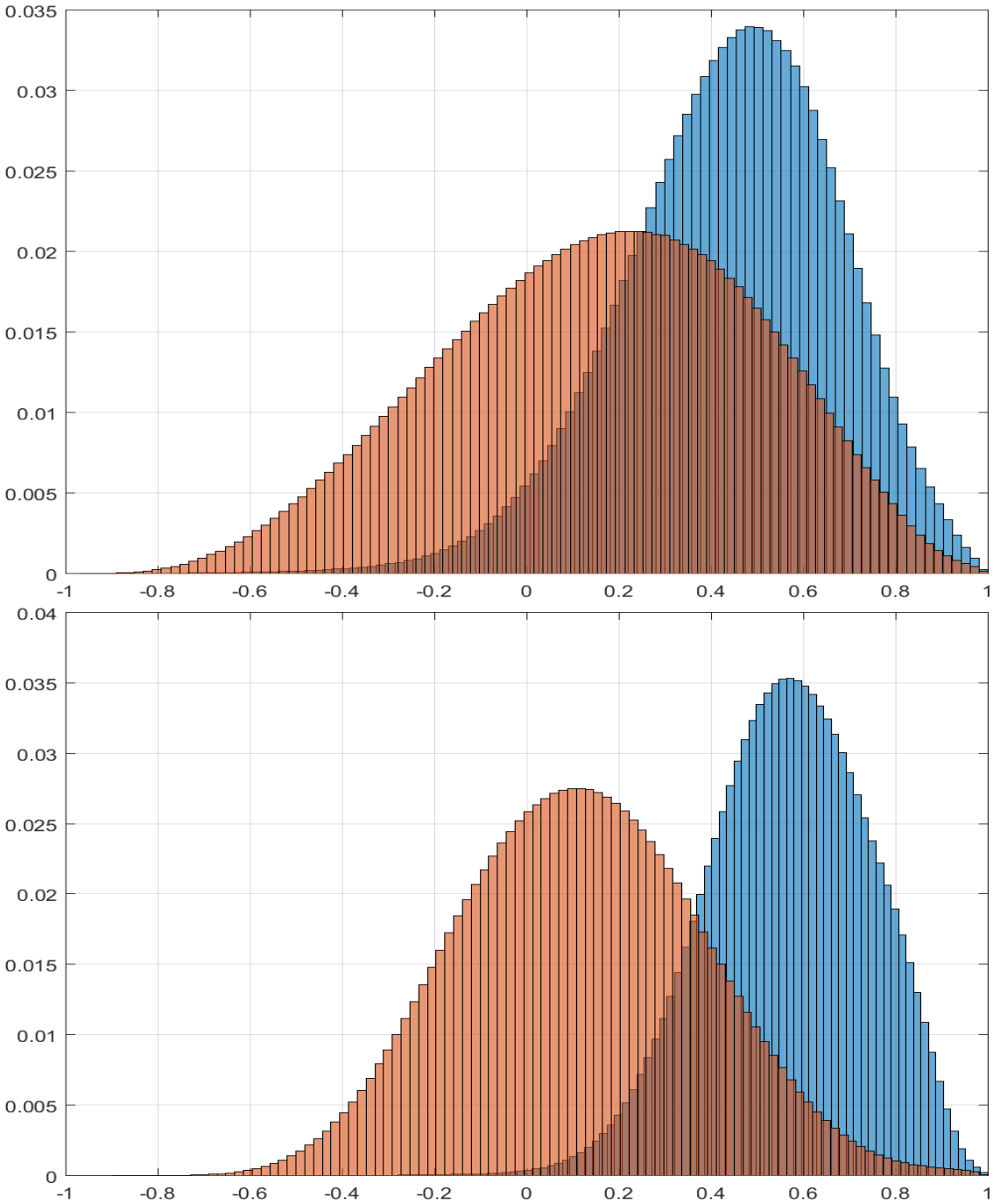

Figure 12.4: Estimations of the normalized mean distribution of IFC of ASL and BOLD networks

Top figure considers the functional networks estimated with 51 volumes and bottom 154 volumes. ASL IFC is shown in blue and BOLD in orange. The mean distribution of correlation is estimated with at most 10^9 pairs of voxels per subject per functional networks and is weighted in consequently in the mean before the normalization.

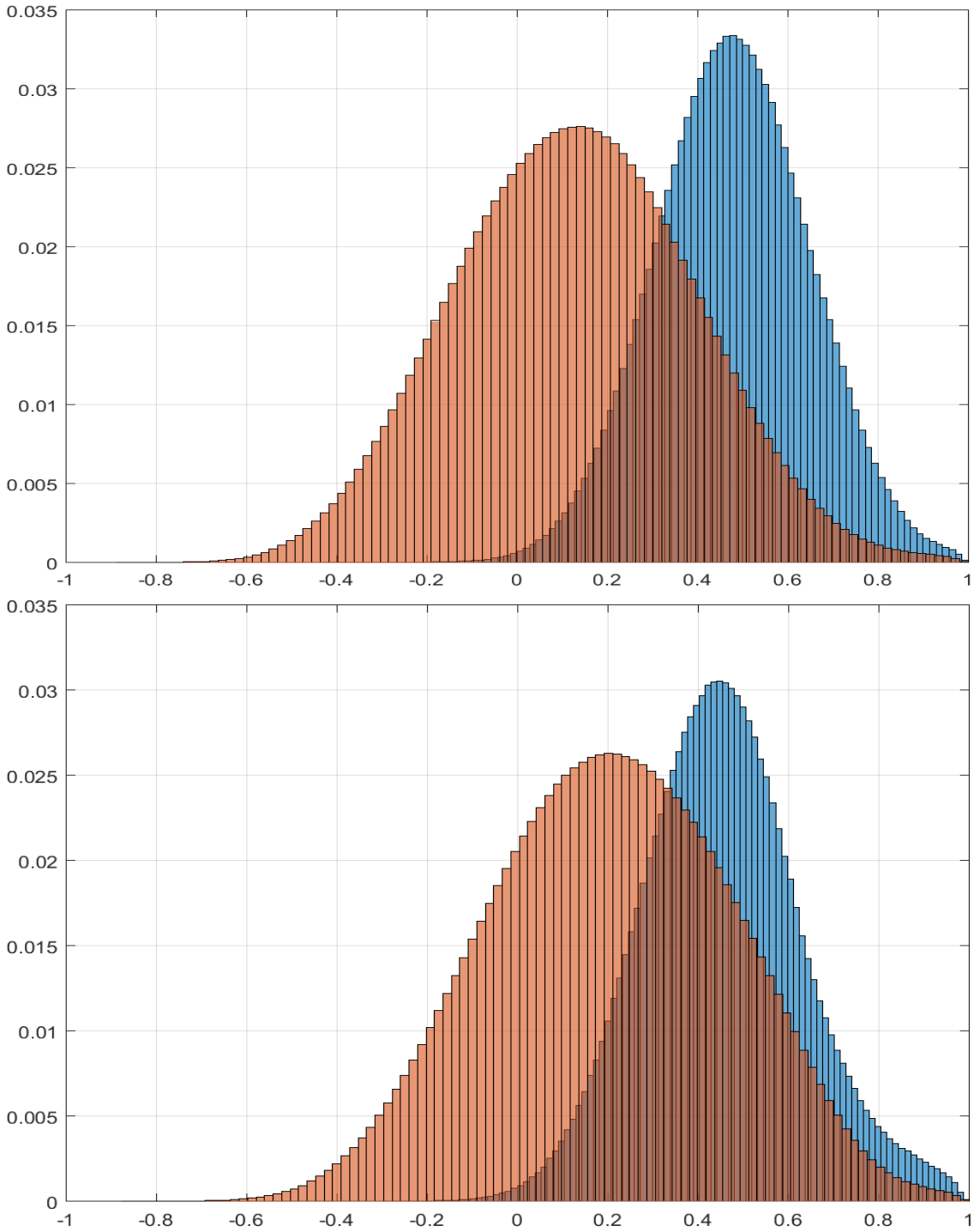

Figure 12.5: Estimations of the normalized mean distribution of IFC of ASL and BOLD networks

Top figure considers the functional networks estimated with 257 volumes and bottom 360 volumes. ASL IFC is shown in blue and BOLD in orange. The mean distribution of correlation is estimated with at most 10^9 pairs of voxels per subject per functional networks and is weighted in consequently in the mean before the normalization.

SEED	AVERAGE IFC - ASL	AVERAGE IFC – BOLD
DMN PREFRONTAL	0.180	0.091
DMN POSTERIOR	0.267	0.076
MOTOR SUPERIOR	0.208	0.084
VISUAL POSTERIOR	0.244	0.081
VISUAL VENTRAL	0.267	0.095
VISUAL DORSAL LEFT	0.224	0.083
VISUAL DORSAL RIGHT	0.212	0.090
LANGUAGE FRONTAL GYRUS LEFT	0.320	0.176
CEREBELLUM ANTERIOR	0.179	0.108

Table 12.1: Mean value of networks IFC with respect to the seed

12.6 Spatial concordance between ASL and BOLD

12.6.1 Motivation

Even though we already know ASL and BOLD estimated functional networks differ by their size and agree by their tissue composition, we would like to investigate how the modalities spatial layout concordance evolves with respect to the number of volumes. With the LOESSs and MSDL, we have interpreted the stabilization of the Jaccard's index and of the AUC of the estimated functional networks with the MSDL, as a sign of spatial stabilization of the estimation, in accordance with some visual inspection. Indeed, if we consider Jaccard's index and AUC as distances between the MSDL references and the estimated functional networks, a stabilization in scores can translate stabilization in spatial extent. However, estimations could be orbiting around references. Even if visual inspection seems to invalidate this hypothesis, or at least showing oscillations as a marginal phenomenon, we did not investigate every estimated functional network and we have no assumption on what happens before scores stabilization. By investigating the Pearson's ϕ coefficient (spatial correlation, detailed below) between ASL and BOLD, i.e. a distance between ASL and BOLD estimated functional networks, we can either strengthen the confirmation of estimation spatial stabilization or detecting some oscillation around the references. Indeed, we can argue that a functional networks estimation can oscillate around its reference, and then, a stabilization in the score does not totally translate a stabilization in spatial layout. However, the case where a functional network estimation oscillates around a MSDL reference with respect to Jaccard's index, and also oscillate around the reference with respect to the AUC, and also oscillate around its corresponding networks in the other modality seems unachievable. By directly comparing ASL and BOLD, we get rid of the reference dependence of the scores. Even if the phenomenon of stabilization is unlikely to be impacted by the references, using a BOLD set of references raises questions about the height of the scores, as discussed in section 12.3.2, since BOLD is likely to benefit from this bias.

Using our former definition of a, b, c, d from section 7.2, the Pearson's ϕ coefficient, often called spatial correlation is:

$$\phi := \frac{ad - bc}{\sqrt{(a+b)(a+c)(b+d)(c+d)}}$$

Equation 12.1: Pearson's ϕ coefficient – Spatial correlation

The two binary variables are here the ASL and BOLD estimated functional networks binary mask computed on voxels: a is the cardinal of the positive matches between ASL and BOLD, d cardinal of the negative matches, b corresponds to cases where ASL estimation suggests a voxel belong to a functional network where BOLD do not, and c the opposite in the modalities. It should be noted the Pearson's ϕ coefficient is exactly the Bravais-Pearson linear correlation given our definition of the two variable [Cramér, 1947], hence the name of spatial correlation. Since the definition matches, it is also interesting to note that in consequence ϕ is related to a square root of a chi-squared statistic, modulo a sample size factor. This unlock more advanced statistical analysis, but we will not need them.

12.6.2 Results

Figure 12.6 shows a collection of spatial correlation heatmaps related to a seed used to the corresponding functional networks maps. The colors of correlation values are normalized between correlation minimum and maximum values with respect to each seed. Correlation values (colors) are the average value over the subjects. The chosen seeds are considered to provide successful detection of the related functional networks in both modalities, regarding our selection criterion. However, even seeds that failed to detect their corresponding functional networks still provide very similar heatmaps of correlation. This similarity may mean that these seeds actually detects real functional networks, unlike at low number of volumes for instance as we discuss in section 12.4.2. These potential real functional networks are however difficult to interpret, since they do not look like functional structure already well-established. Whichever the seed, maximum correlation values are not very high: this was expected since ASL estimated functional networks are usually twice to three times smaller than BOLD one. Heatmaps shows almost a line symmetry around the first bisector. It is interesting to notice the evolution of the spatial correlation between ASL and BOLD is close to the LOESS modeling. Firstly, the correlation increases rapidly at low number of volumes ($\leq$100). Secondly, spatial correlations show a slower increase with intermediate number of volumes. Eventually, correlations stabilize after a certain number of volumes. This value obviously depends on the definition of stabilization, exactly as the issue we discuss for the LOESS modeling. If we consider a threshold of spatial correlation between 80% and 90% of the maximum, the satisfactory number of volumes to achieve is close to the value we find for ASL and BOLD with the LOESSs in section 11.3.2. Note that the area of correlation stability is not totally symmetrical with respect to the first bisector. While there is an overall symmetrical behavior of the spatial correlation with respect to the modalities, the area of stability can start with a difference up to 60 volumes between ASL and BOLD (90% + DMN: 120 BOLD / 180 ASL). This difference tends to disappear with relaxed definition of stabilization (like 80%).

The combined results for spatial correlation and LOESS modeling tend to confirm a posteriori the spatial stabilization was not dependent from the reference. Indeed, without any visual inspection, spatial correlation never indicates whether estimated functional networks achieve satisfactory spatial layout or not, i.e. if SBA manage to detect the functional network in our case. Moreover, the ASL and BOLD could have spatially evolved the same way without impacting spatial correlation a lot. However, with the previous work made with the MSDL reference, we know which functional networks estimation can be considered as successful, and also when they globally achieve spatial stability. With LOESSs and MSDL, the atlas used as a set of references may have an impact, but mostly on scores height and not on stabilization phenomenon. By getting rid of atlases with spatial correlation, and in combination with the prior knowledge from LOESSs and MSDL, we can say that after a certain number of volumes, ASL and BOLD provide their best estimation of functional network, this estimation is stable, and also that ASL and BOLD agree the most on estimation at this point.

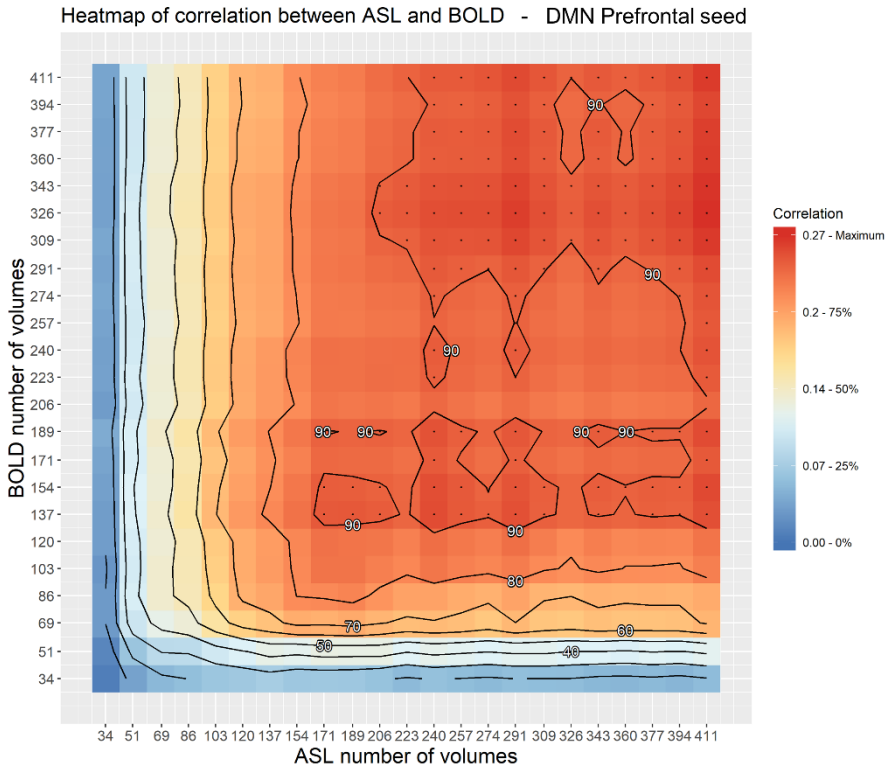
Heatmap of correlation between ASL and BOLD - DMN Prefrontal seed
BOLD number of volumes
411 394 377 360 343 326 309 291 274 257 240 223 206 189 171 154 137 120 103 86 69 51 34
ASL number of volumes
34 51 69 86 103 120 137 154 171 189 206 223 240 257 274 291 309 326 343 360 377 394 411
Correlation
0.27 - Maximum
0.2 - 75%
0.14 - 50%
0.07 - 25%
0.00 - 0%

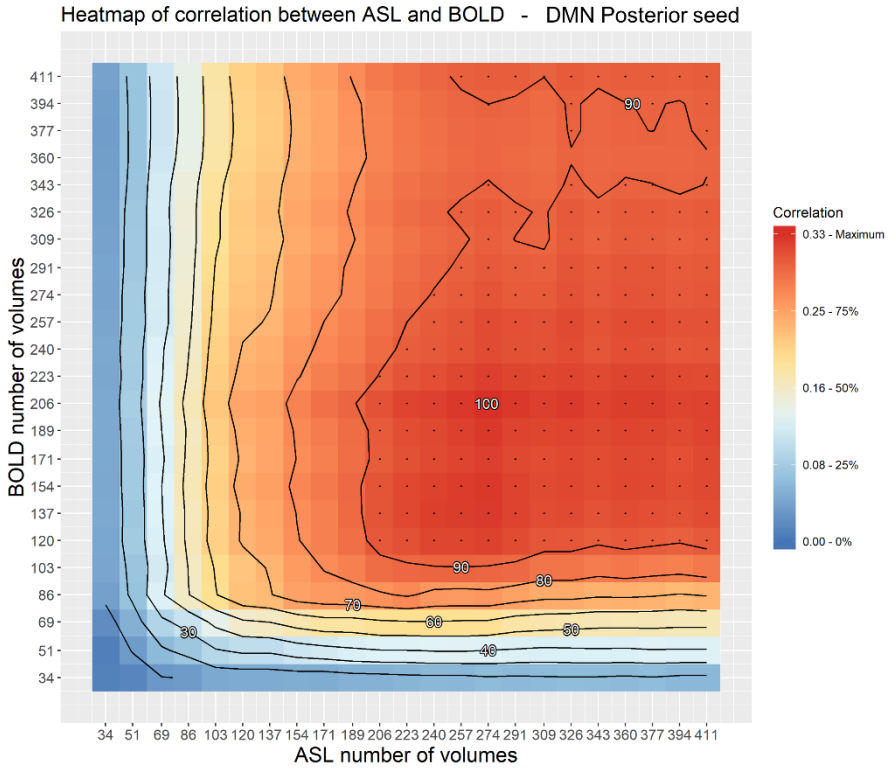
Heatmap of correlation between ASL and BOLD - DMN Posterior seed
BOLD number of volumes
411 394 377 360 343 326 309 291 274 257 240 223 206 189 171 154 137 120 103 86 69 51 34
ASL number of volumes
34 51 69 86 103 120 137 154 171 189 206 223 240 257 274 291 309 326 343 360 377 394 411
Correlation
0.33 - Maximum
0.25 - 75%
0.16 - 50%
0.08 - 25%
0.00 - 0%

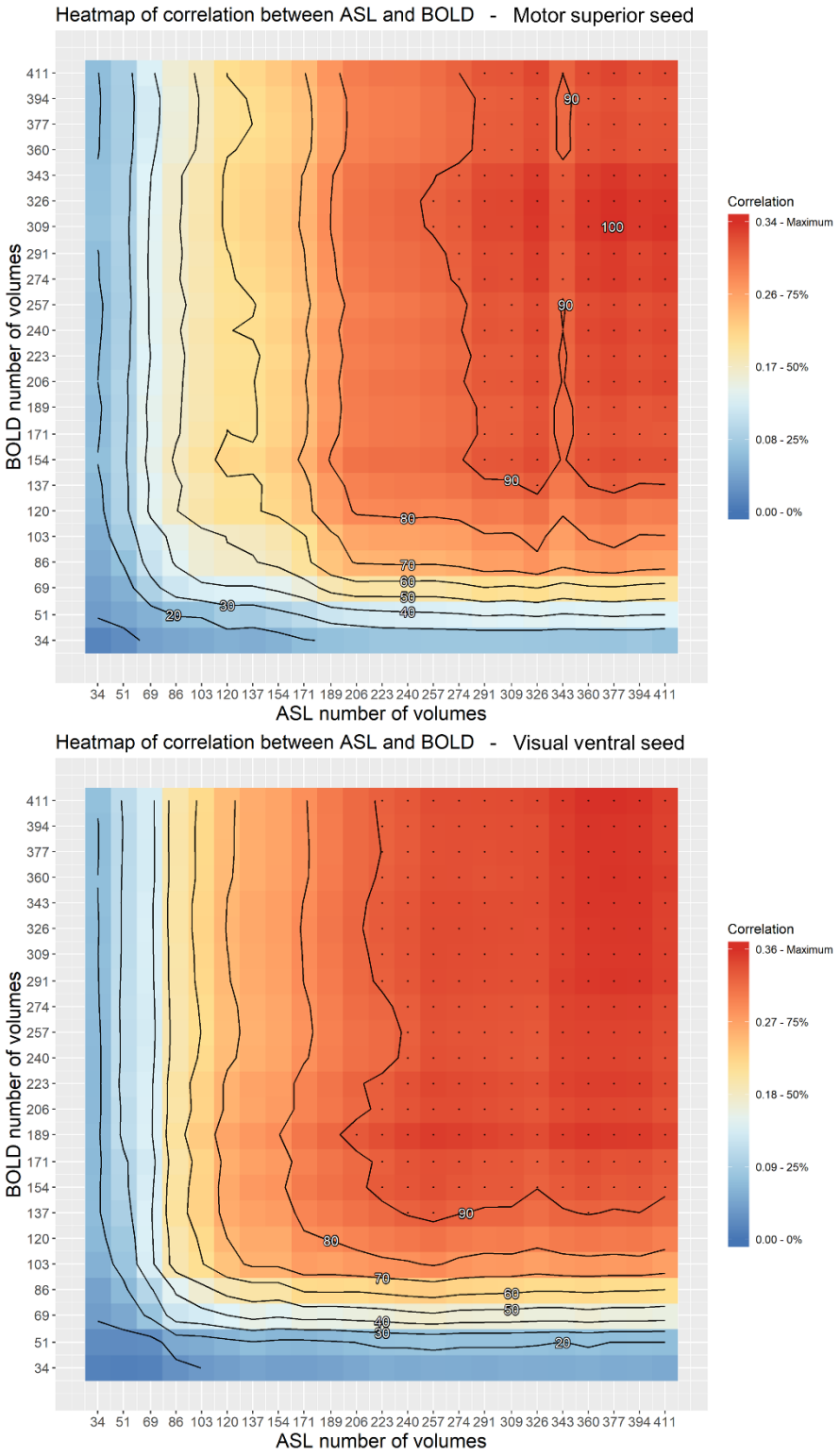

Figure 12.6: Collection of heatmaps of spatial correlation between ASL and BOLD

Correlation values (colors) are normalized between minimum and maximum values for each seed. Contour lines shows every 10% step of increase. The spatial correlation behaves symmetrically around the first bisector: a fast increase before 100 volumes, a slower increase between 100 and roughly 200 volumes, and finally a stabilization plateau with values close to the maximum. As suggested by contour lines, the plateau size depends a lot on which percentage of the maximum value is considered to be the edge.

12.7 Conclusion

We first showed that the number of active voxels is a discriminant variable for the modality. Indeed, no matter the seed, ASL estimated functional networks always have a smaller size compared to BOLD. This result matches similar investigations in the literature [Zhang et al., 2018]. We showed that this result is also true with respect to the number of volumes, even if the size ratio is smaller with higher number of volumes. In the previous section, we investigated the composition in terms of GM, WM and CSF of the estimated functional networks. Interestingly, this composition is extremely homogeneous, whether it is with respect to the seed, with respect to the number of volumes, or more importantly, with respect to the modality.

Secondly, we investigate in section 12.4 the tissues distribution of estimated functional networks. Indeed, our functional networks of interest are expected to have most of their voxels located in grey matter, few in white matter, and none in cerebrospinal fluid. Even with the large difference in size, the tissue distribution of estimated functional networks is actually extremely homogeneous between ASL and BOLD. No matter the seed, the subject, the number of volumes, the modality, the tissue distribution is for almost every estimation is as follow: 55-60% in grey matter, 25-30% in white matter, 10-15% in cerebrospinal fluid. In other words, given a tissue distribution, it is not possible to guess to which modality it corresponds: the tissue distribution has no discriminative power.

Thirdly, we investigate the intrinsic functional connectivity of estimated functional networks. We address the issue of functional networks scaling in the first part of the manuscript in section: interpreted as the result of a statistical clustering, an estimation of a functional network, i.e. a cluster, is wanted to have a minimal intra-variance, i.e. a maximal intrinsic functional connectivity. We show that no matter the seeds, the successfully estimated functional networks have a better intrinsic functional connectivity in rsASL than in rsBOLD.

We end the comparison by investigating the spatial correlation between rsASL and rsBOLD estimations. We only consider seeds that are able to effectively detect a functional network. For every seed, the spatial correlation interestingly behaves like its corresponding LOESS in previous modeling: a low number of volumes is associated with a low spatial correlation, and interestingly, after a number of volumes close to the range where we detected stability with the MSDL, the spatial correlation between rsASL and rsBOLD functional maps reaches its highest values and stays stable with bigger number of volumes. It confirms that the impact of using an atlas is extremely limited in the exhibition of the stabilization phenomenon, and this way, definitely confirm the spatial stabilization of functional networks.

Conclusion

This manuscript had three main objectives. The first one was to confirm ASL as a viable resting-state fMRI technique. The second one was to address the effect of scan duration on the functional networks estimation. The third one was to test rsASL performance against rsBOLD with respect to the scan duration.

We first investigated the effect of scan duration in rsASL with classic methods which model what a rsfMRI investigator would experience. We used a standard pCASL sequence, typical preprocessing and simple estimation methods at the subject scale, as we wanted to show that ASL is fully viable as a rsfMRI technique even with the simplest techniques. An estimation of a functional network is validated by an expert if it is close to what the expert expects the functional network to look like. We mimicked this process by scoring the overlap of the estimated functional networks with a set of reference networks from a resting-state atlas. We then modeled the evolution of scores with respect to the scan duration/the number of volumes. The spatial representation of functional networks stabilized after a certain acquisition duration for the six common functional networks we focused on. While the start of the stabilization is depending on the functional network considered and, more importantly, on the definition of stabilization, 14 minutes duration/240 volumes is suggested as most likely sufficient for resting-state ASL. Indeed, we used a typical sequence, preprocessing and modeling. Hence any method that improves the detection of functional networks is likely to provide an earlier stabilization start, i.e. smaller optimal number of volumes/shorter duration. As we were able to detect every functional networks of interest, we also confirm the viability of ASL as a rsfMRI technique.

We integrated rsBOLD data in our study. The first step was to investigate the impact of the number of volumes in resting-state BOLD. We addressed this question by applying the methodological framework we developed for the ASL data to the BOLD data. It seems that, as in rsASL, functional networks estimation in rsBOLD also stabilizes after acquiring a certain number of volumes. However, rsBOLD results were more heterogeneous: the start of the stabilization is harder to define precisely compared to rsASL. The higher variance of BOLD could, though, be explained by the relatively small number of subjects. An interesting result is that the evolution of functional networks with respect to the number of volumes is similar. The range of number of volumes where stabilization starts for both modalities are close: 240 volumes for rsASL, 250 to 290 volumes for rsBOLD.

The comparison between ASL and BOLD used a third-party atlas. As the atlas is built with rsBOLD data, the second step was to compare the modality without the atlas. We focused on four measures: the number of active voxels, the tissue distribution, the intrinsic functional connectivity and the spatial correlation.

The investigation of the number of active voxels showed that the size of BOLD functional networks is always half to three times bigger than ASL, no matter the number of volumes considered. Regarding the tissue distribution, results were extremely homogeneous. In other words, given a tissue distribution, it is not possible to discriminate seeds, subjects, number of volumes and most importantly, ASL and BOLD. The investigation of intrinsic functional connectivity exhibited a better performance of rsASL than rsBOLD. For all successful seeds and number of volumes, rsASL networks intrinsic connectivity is better

than rsBOLD. Last measure investigated was the spatial correlation between rsASL and rsBOLD. The correlation was maximal and stable when both BOLD and ASL data reach at least 200-250 volumes. Since this is also the range of volumes for which most functional networks are starting to stabilize and reach their best estimation, we can add that this is also when BOLD and ASL most agree on functional networks estimation. This also tends to strengthen, a posteriori, the proposition stating that the stabilization of Jaccard's index and of AUC (computed by comparison to an atlas) was reflecting the stabilization of spatial representation of functional networks.

We addressed the effect of scan duration mostly through methodological considerations. As we worked under a single given set of parameters, the suggested duration of 14 min could be strongly influenced by the preprocessing and sequence parameters. Although the influence of each of them must be kept in mind, most of them have a specific bibliography that goes well beyond the issue of the optimal acquisition duration. Regarding rsASL, however, two parameters may have a deep impact on our results: post-labeling delay (PLD) and repetition time (TR). Indeed, shorter PLD tend to gives better functional networks representation but worse estimation of CBF. As the principal advantage of ASL over BOLD is CBF quantification, we kept a quite long PLD, compared to classical values in use in the resting-state literature. Hence, an investigator focusing on a better functional estimation could use a shorter PLD, and, while tempting, we cannot assume that shorter PLD comes along with an earlier stabilization.

In our opinion, the critical parameter is the repetition time (TR). It defines the sample frequency of the resting-state signal and turns the 14 min suggestion into 240 volumes. Its variation may shift the stabilization step toward a higher/lower number of volumes and hence a longest/shortest duration, without changing the stabilization phenomenon of the functional networks representation after a certain number of volumes (i.e. same signal but different sampling frequency). As a pioneer work on the effect of scan duration in rsASL, we focused more on the modeling rather than investigating the influence of the TR. However, a specific study on the relationship between repetition time, number of volumes and quality of functional network estimation would be highly beneficial to better define the optimal duration and also would be useful when an investigator sets up a sequence.

Regarding acquisition protocols, we try to use the most generic sequences in use for both rsASL and rsBOLD in order to suggest a sufficient number of volumes to use, as more advanced sequences are expected to provide same or earlier stabilization start. We discard subjects variability by using the same subjects for both sequences, but yet, each MRI modality is not acquired at the same time. An interesting approach, in order to better seize the cross effect of scan duration and MRI modality, would be to acquire both ASL and BOLD at the same time, by using a dual-echo sequence [Cohen et al., 2018]. An alternative implementation can be made even by only using a standard ASL sequence. Indeed, in ASL, the control image contains only BOLD signal, called concurrent BOLD which can be compared to the subtraction control/label, i.e. the ASL signal [Zhu et al., 2013].

As mentioned in the first chapter, functional connectivity has various modeling. Here, we choose to model functional connectivity with linear correlation and construct functional networks with SBA, as it was well-adapted to compare rsASL with rsBOLD regarding methodological considerations. As ICA is also widely used, an investigation of the functional networks spatial stabilization using the definition of functional connectivity through statistical independence should be beneficial. Indeed, it is not guaranteed that statistical independence and linear correlation provide a similar stabilization phenomenon.

We focused our investigation on the construction of functional networks in order to assess the feasibility of ASL as a method for resting-state fMRI. We showed that ASL is able to reconstruct the functional networks. The next step would be to investigate the interactions between these functional networks and the investigation of the small-world architecture with respect to the number of volumes, similarly to the work done in BOLD on the topic [Birn et al., 2013; Termenon et al., 2016].

As we wanted to confirm the efficiency of ASL in resting-state fMRI, we naturally focused on a subject scale study. While general conclusions at the subject scale are still valid at the group scale, e.g. stabilization of functional networks after a certain duration, a specific group scale comparison would answer unresolved issues. First, do ASL and BOLD require the same number of subjects to define reliable networks at group scale? Such work was carried out by [Termenon et al., 2016] for BOLD. Secondly, the effect of scan duration could be assessed by comparing the individual maps at a certain number of volumes to a group-made reference, similarly to the work of [Bouix et al., 2017].

As an exploratory study, we have considered a large range of number of volumes with a relatively high temporal resolution. The consequence is that even with only 7 subjects, more than 12 000 functional network maps have been generated and analyzed. Given the knowledge produced by the work, further studies could diminish the temporal resolution and narrow the range of number of volumes to investigate in order to include far more subjects without increasing the computational time. We have indeed limited sources of variability by considering a homogeneous population, and a larger population should be considered regarding the rsASL optimal scan duration issue in order to assess population factors influence, in particular the age.

In a nutshell, we showed that rsBOLD outperforms rsASL on numerous aspects (temporal and spatial resolution, SNR, practicability, easier detection of networks), but not on every aspect, such as the intrinsic functional connectivity. When considering the number of volumes, ASL can even compete with BOLD: ASL showed less variability with the LOESSs and MSDL modeling, same functional networks tissue distribution, and similar number of volumes to get the best estimation of functional networks. With the ability to quantify CBF, unlike BOLD, we believe that the results of this manuscript have shown that rsASL in particular and ASL general deserve an increasing exposure.

Appendix

Resting-state ASL sequence parameters

SIEMENS MAGNETOM Verio syngo MR B17

\\USER\RECHERCHE\NEURO - ASL\EPARS OSS IRM\BOLD RESTING STATE - TR1400

TA: 12:07 PAT: 2 Taille voxel: 3.0×3.0×4.0 mm S/b rel.: 1.00 SIEMENS: ep2d_bold

Propriétés

Prio Recon	Désactivé
Avant la mesure	
Après la mesure	
Load to viewer	Activé
Inline movie	Désactivé
Auto store images	Activé
Load to stamp segments	Désactivé
Charger images dans segments graph.	Désactivé
Auto open inline display	Désactivé
Start measurement without further preparation	Activé
En attente d'une action utilisateur pour démarrer	Activé
Start measurements	single

Routine

Groupe coupes 1	
Coupes	24
Fac. distance	50 %
Position	L2.4 P24.8 H43.4
Orientation	T > C-13.8
Dir. codage phase	A >> P
Rotation	0.00 deg
Suréchantil. phase	0 %
FoV	192 mm
Phase FoV	100.0 %
Epaiss. coupe	4.0 mm
TR	1400 ms
TE	30 ms
Nb. d'excitations	1
Concaténations	1
Filtre	Filtre brut, Pré-acq. normalisée
Elém. antenne	HEA;HEP

Contraste

MTC	Désactivé
Angle de basc.	70 deg
Suppression graisse	Sat. graisse
Mode moyenne	Long terme
Reconstruction	Magnitude
Répétitions	514
Retard en TR	0 ms
Séries multiples	Désactivé

Résolution

Résolution base	64
Résolution phase	100 %
Phase Fourier partiel	Désactivé
Interpolation	Désactivé
Mode PAT	GRAPPA
Facteur d'accél. PE	2
Lignes réf. PE	24
Mode antenne Matrix	Dual
Mode scan de référence	Séparé
Corr. Distortion	Désactivé
Images non filtrées	Désactivé
Pré-acq. normalisée	Activé
Filtre brut	Activé
Intensité	Faible
Pente	25
Filtre elliptique	Désactivé
Hamming	Désactivé

Géométrie

Mode multicoupe	Entrelacé
Série	Entrelacé
Spécial sat.	Néant

Système

Body	Désactivé
HEP	Activé
HEA	Activé
SP4	Désactivé
SP2	Désactivé
SP8	Désactivé
SP6	Désactivé
SP3	Désactivé
SP1	Désactivé
SP7	Désactivé
SP5	Désactivé
Mode positionnement	REF
Position table	H
Position table	0 mm
MSMA	S - C - T
Sagittal	R >> L
Coronal	A >> P
Transversal	F >> H
Mode combinaison antenne	Somme des carrés
Sélection d'antenne automatique	Défaut
Mode shim	Standard
Ajus. avec ant. corps	Désactivé
Confirmer le réglage de fréq.	Désactivé
Présence silicone	Désactivé
? Amplitude réf. 1H	0.000 V
Tolérance d'ajustement	Auto
Volume d'ajustement	
Position	L2.4 P24.8 H43.4
Orientation	T > C-13.8
Rotation	0.00 deg
R >> L	192 mm
A >> P	192 mm
F >> H	112 mm

Physio

1er signal/mode	Néant

BOLD

Statistiques GLM	Désactivé
Cartes t dynamiques	Activé
Ignorer val. démarrage	0
Ignorer après transition	0
Modèles états trans.	Activé
Filtre temp. passe-haut	Activé
Seuil	4.00
Taille paradigme	3
Mes[1]	Ligne base
Mes[2]	Ligne base
Mes[3]	Actif
Correc. mouvement	Activé
Interpolation	3D-K-space
Filtre spatial	Désactivé

Séquence

Introduction	Activé

SIEMENS MAGNETOM Verio syngo MR B17

Largeur de bande	2232 Hz/Px
Ecart écho libre	Désactivé
Ecart écho	0.53 ms
Facteur EPI	64
Type impulsion RF	Normal
Mode gradients	Rapide

Resting-state BOLD sequence parameters

SIEMENS MAGNETOM Verio syngo MR B17

\\USER\RECHERCHE\NEURO - ASL\EPARS OSS IRM\PCASL LD 1500 PLD 1250 TR 3500MS 420 REPET
TA: 25:02 PAT: 2 Taille voxel: 3.5×3.5×5.0 mm S/b rel.: 1.00 USER: ep2d_pcasl_UI_PHC

Propriétés	
Prio Recon	Désactivé
Avant la mesure	
Après la mesure	
Load to viewer	Activé
Inline movie	Désactivé
Auto store images	Activé
Load to stamp segments	Désactivé
Charger images dans segments graph.	Désactivé
Auto open inline display	Désactivé
Start measurement without further preparation	Activé
En attente d'une action utilisateur pour démarrer	Activé
Start measurements	single

Routine	
Groupe coupes 1	
Coupes	24
Fac. distance	20 %
Position	R3.7 P21.1 H18.7
Orientation	T > C-5.7
Dir. codage phase	P >> A
Rotation	180.00 deg
Suréchantil. phase	0 %
FoV	224 mm
Phase FoV	100.0 %
Epaiss. coupe	5.0 mm
TR	3500 ms
TE	12 ms
Nb. d'excitations	1
Concaténations	1
Filtre	Filtre brut, Pré-acq. normalisée
Elém. antenne	HEA;HEP

Contraste	
MTC	Désactivé
Angle de basc.	90 deg
Suppression graisse	Sat. graisse
Mode moyenne	Long terme
Reconstruction	Magnitude
Répétitions	426
Retard en TR	0 ms
Séries multiples	Désactivé

Résolution	
Résolution base	64
Résolution phase	100 %
Phase Fourier partiel	Désactivé
Interpolation	Désactivé
Mode PAT	mSENSE
Facteur d'accél. PE	2
Lignes réf. PE	24
Mode antenne Matrix	Auto (Triple)
Mode scan de référence	Séparé
Corr. Distortion	Désactivé
Images non filtrées	Désactivé
Pré-acq. normalisée	Activé
Filtre brut	Activé
Intensité	Faible
Pente	25
Filtre elliptique	Désactivé
Hamming	Désactivé

Géométrie	
Mode multicoupe	Entrelacé
Série	Croissant
Spécial sat.	Néant

Système	
Body	Désactivé
HEP	Activé
HEA	Activé
SP4	Désactivé
SP2	Désactivé
SP8	Désactivé
SP6	Désactivé
SP3	Désactivé
SP1	Désactivé
SP7	Désactivé
SP5	Désactivé
Mode positionnement	FIX
Position table	H
Position table	0 mm
MSMA	S - C - T
Sagittal	R >> L
Coronal	A >> P
Transversal	F >> H
Mode combinaison antenne	Somme des carrés
Sélection d'antenne automatique	Défaut
Mode shim	Standard
Ajus. avec ant. corps	Désactivé
Confirmer le réglage de fréq.	Désactivé
Présence silicone	Désactivé
? Amplitude réf. 1H	0.000 V
Tolérance d'ajustement	Auto
Volume d'ajustement	
Position	R3.7 P21.1 H18.7
Orientation	T > C-5.7
Rotation	180.00 deg
R >> L	224 mm
A >> P	224 mm
F >> H	119 mm

Physio	
1er signal/mode	Néant

BOLD	
Statistiques GLM	Activé
Cartes t dynamiques	Désactivé
Ignorer val. démarrage	0
Ignorer après transition	0
Modèles états trans.	Activé
Filtre temp. passe-haut	Activé
Seuil	4.00
Taille paradigme	16
Mes[1]	Ligne base
Mes[2]	Ligne base
Mes[3]	Ligne base
Mes[4]	Ligne base
Mes[5]	Ligne base
Mes[6]	Ligne base
Mes[7]	Ligne base
Mes[8]	Ligne base

SIEMENS MAGNETOM Verio syngo MR B17

Mes[9]	Actif
Mes[10]	Actif
Mes[11]	Actif
Mes[12]	Actif
Mes[13]	Actif
Mes[14]	Actif
Mes[15]	Actif
Mes[16]	Actif
Correc. mouvement	Activé
Interpolation	3D-K-space
Filtre spatial	Désactivé

Séquence

Introduction	Désactivé
Largeur de bande	2442 Hz/Px
Ecart écho libre	Désactivé
Ecart écho	0.5 ms
Facteur EPI	64
Type impulsion RF	Normal
Mode gradients	Rapide
CASL Method	Multi-slice
Label Offset	90 mm
Post Label Delay	125000 us
Num RF Blocks	82
RF GAP	360 us
Crusher Gradient	0 s/mm2
mean Gz x10	6 mT/m
phi adjust	100 percent

Seeds Location in MNI152 coordinates

Expected Networks	**Seed**	**Location in MNI152**
DMN	Prefrontal	(1,55,-3)
DMN	Left	(-39,-77,33)
DMN	Right	(47,-67,29)
DMN	Posterior	(1,-61,38)
Motor	Left	(-55,-12,29)
Motor	Right	(56,-10,29)
Motor	Superior	(0,-31,67)
Visual	Primary	(2,-79,12)
Visual	Ventral	(0,-93,-4)
Visual	Dorsal Left	(-37,-79,10)
Visual	Dorsal Right	(38,-72,13)
Salience	Cingulate Anterior	(0,22,35)
Salience	Prefrontal Left	(-32,45,27)
Salience	Prefrontal Right	(32,46,27)
Language	Frontal Gyrus Left	(-51,26,2)
Language	Frontal Gyrus Right	(54,28,1)
Language	Temporal Gyrus Left	(-57,-47,15)
Language	Temporal Gyrus Right	(59,-42,13)
Cerebellum	Anterior	(0,-63,-30)
Cerebellum	Posterior	(0,-79,-32)

Boxplots of AUC distribution

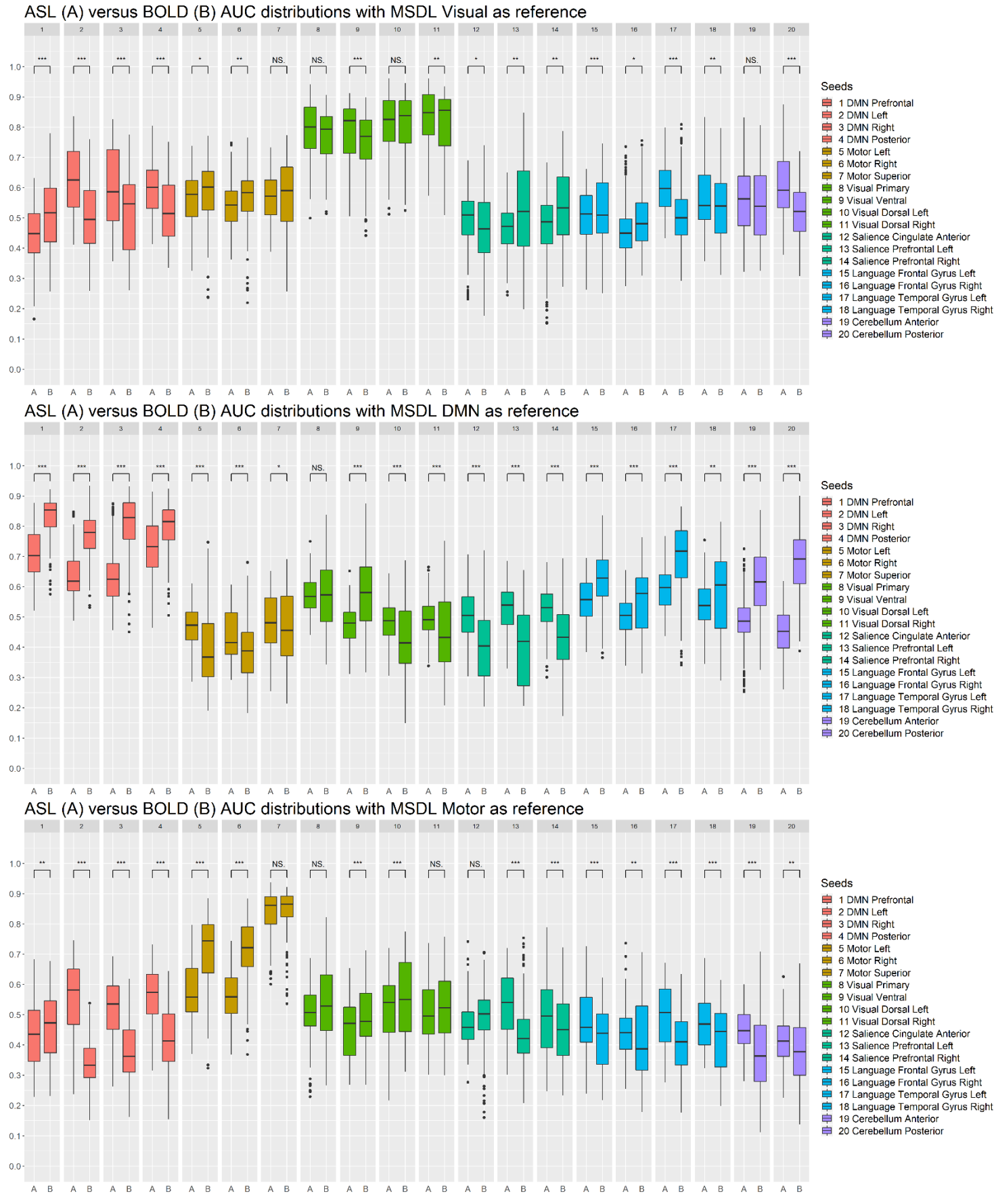

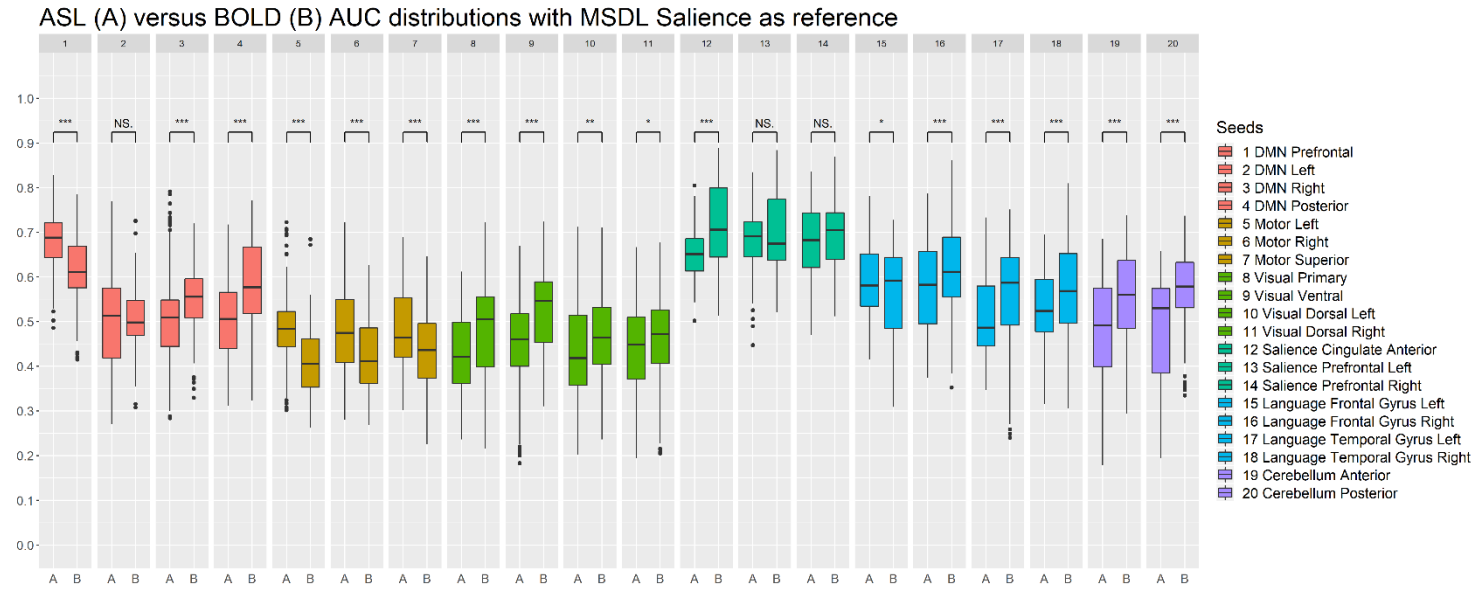
ASL (A) versus BOLD (B) AUC distributions with MSDL Salience as reference
Seeds
1 DMN Prefrontal
2 DMN Left
3 DMN Right
4 DMN Posterior
5 Motor Left
6 Motor Right
7 Motor Superior
8 Visual Primary
9 Visual Ventral
10 Visual Dorsal Left
11 Visual Dorsal Right
12 Salience Cingulate Anterior
13 Salience Prefrontal Left
14 Salience Prefrontal Right
15 Language Frontal Gyrus Left
16 Language Frontal Gyrus Right
17 Language Temporal Gyrus Left
18 Language Temporal Gyrus Right
19 Cerebellum Anterior
20 Cerebellum Posterior

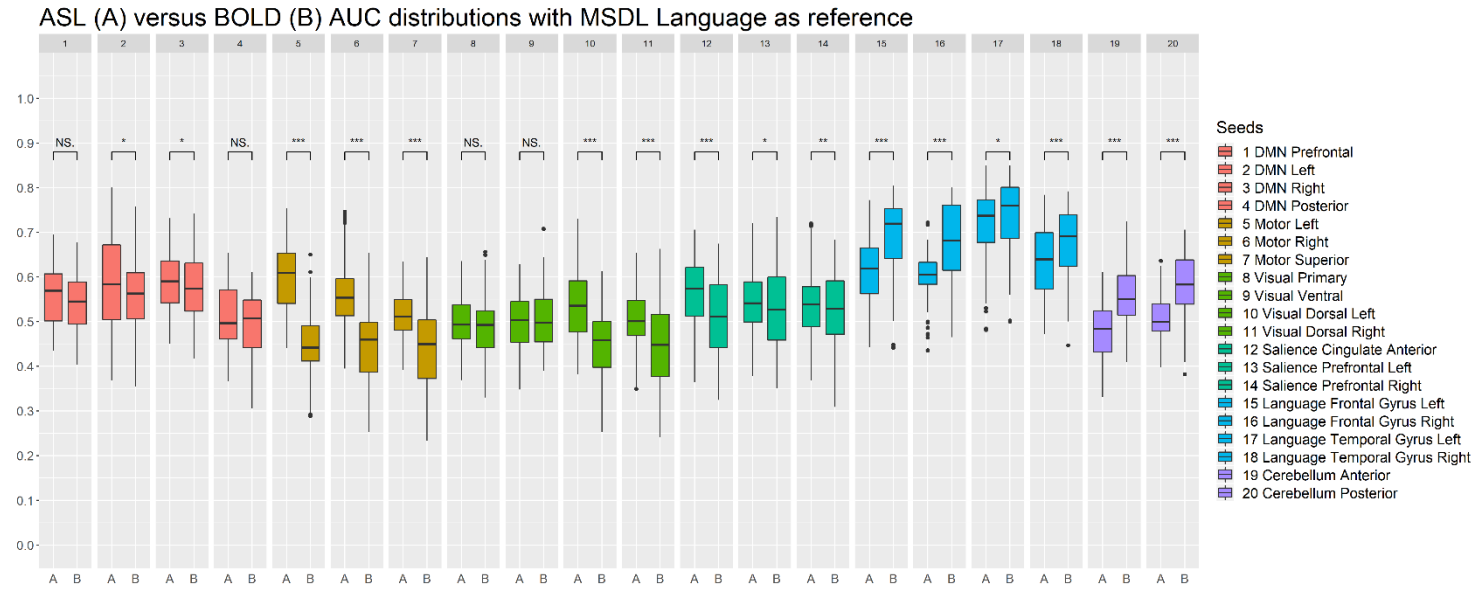
ASL (A) versus BOLD (B) AUC distributions with MSDL Language as reference
Seeds
1 DMN Prefrontal
2 DMN Left
3 DMN Right
4 DMN Posterior
5 Motor Left
6 Motor Right
7 Motor Superior
8 Visual Primary
9 Visual Ventral
10 Visual Dorsal Left
11 Visual Dorsal Right
12 Salience Cingulate Anterior
13 Salience Prefrontal Left
14 Salience Prefrontal Right
15 Language Frontal Gyrus Left
16 Language Frontal Gyrus Right
17 Language Temporal Gyrus Left
18 Language Temporal Gyrus Right
19 Cerebellum Anterior
20 Cerebellum Posterior

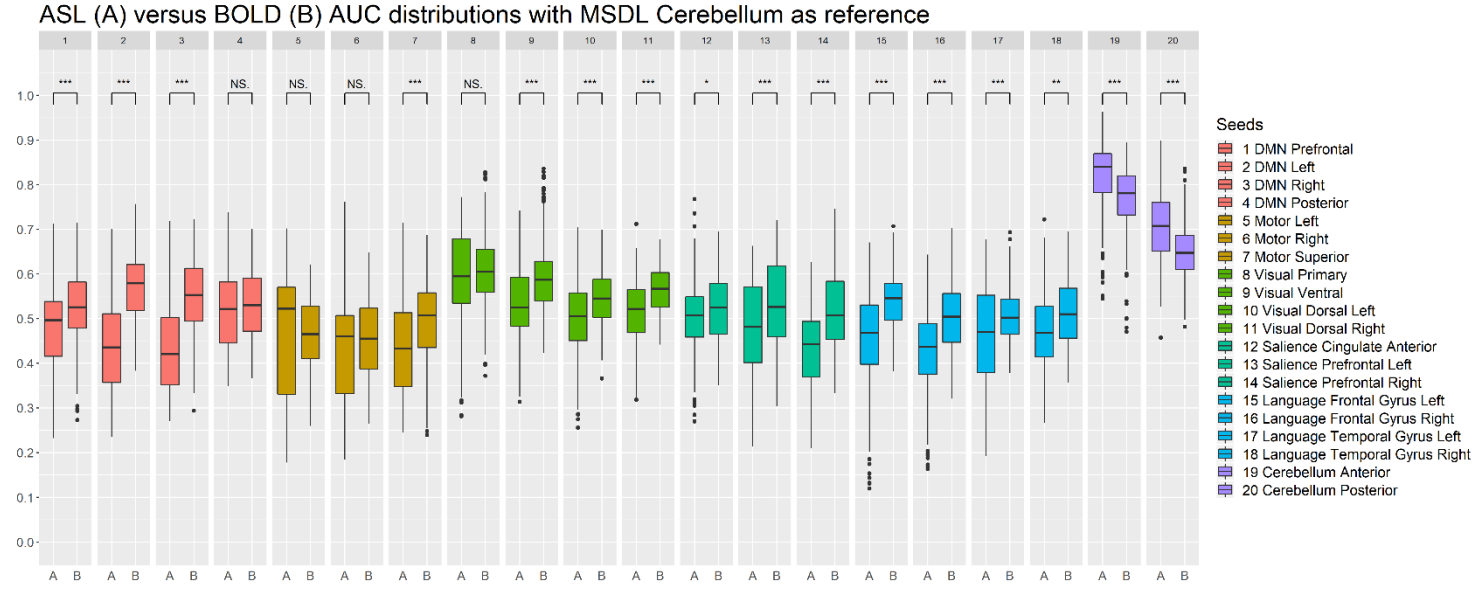
ASL (A) versus BOLD (B) AUC distributions with MSDL Cerebellum as reference
Seeds
1 DMN Prefrontal
2 DMN Left
3 DMN Right
4 DMN Posterior
5 Motor Left
6 Motor Right
7 Motor Superior
8 Visual Primary
9 Visual Ventral
10 Visual Dorsal Left
11 Visual Dorsal Right
12 Salience Cingulate Anterior
13 Salience Prefrontal Left
14 Salience Prefrontal Right
15 Language Frontal Gyrus Left
16 Language Frontal Gyrus Right
17 Language Temporal Gyrus Left
18 Language Temporal Gyrus Right
19 Cerebellum Anterior
20 Cerebellum Posterior

List of Figures

List of tables

List of equations

Bibliography

Abreu, R., Leal, A., Figueiredo, P., 2018. EEG-informed fMRI: A review of data analysis methods. Front. Hum. Neurosci. 12, 1–23. https://doi.org/10.3389/fnhum.2018.00029

Achard, S., Bullmore, E., 2007. Efficiency and cost of economical brain functional networks. PLoS Comput. Biol. 3, 0174–0183. https://doi.org/10.1371/journal.pcbi.0030017

Aertsen, A.M.H.J., Gerstein, G.L., Habib, M.K., Palm, G., 1989. Dynamics of neuronal firing correlation: Modulation of "effective connectivity." J. Neurophysiol. 61. https://doi.org/10.1152/jn.1989.61.5.900

Agosta, F., Pievani, M., Geroldi, C., Copetti, M., Frisoni, G.B., Filippi, M., 2012. Resting state fMRI in Alzheimer's disease: Beyond the default mode network. Neurobiol. Aging 33, 1564–1578. https://doi.org/10.1016/j.neurobiolaging.2011.06.007

Aguirre, G., Zarahn, E., D'Esposito, M., 1998. The variability of human, BOLD hemodynamic responses. Neuroimage 8, 360–9. https://doi.org/10.1006/nimg.1998.0369

Aguirre, G.K., Detre, J.A., Zarahn, E., Alsop, D.C., 2002. Experimental design and the relative sensitivity of BOLD and perfusion fMRI. Neuroimage 15, 488–500. https://doi.org/10.1006/nimg.2001.0990

Alakörkkö, T., Saarimäki, H., Glerean, E., Saramäki, J., Korhonen, O., 2017. Effects of spatial smoothing on functional brain networks. Eur. J. Neurosci. 46, 2471–2480. https://doi.org/10.1111/ejn.13717

Alsop, D., Dai, W., Grossman, M., Detre, J., 2010. Arterial Spin Labeling Blood Flow MRI: Its Role in the Early Characterization of Alzheimer's Disease. J. Alzheimer's Dis. 20, 871–880. https://doi.org/10.3233/JAD-2010-091699

Alsop, D., Detre, J., Golay, X., Günther, M., Hendrikse, J., Hernandez-Garcia, L., Lu, H., Macintosh, B., Parkes, L., Smits, M., Van Osch, M., Wang, D., Wong, E., Zaharchuk, G., 2015. Recommended implementation of arterial spin-labeled Perfusion mri for clinical applications: A consensus of the ISMRM Perfusion Study group and the European consortium for ASL in dementia. Magn. Reson. Med. 73, 102–116. https://doi.org/10.1002/mrm.25197

Anderson, J.S., Ferguson, M.A., Lopez-Larson, M., Yurgelun-Todd, D., 2011. Reproducibility of single-subject functional connectivity measurements. Am. J. Neuroradiol. 32, 548–555. https://doi.org/10.3174/ajnr.A2330

Aurich, N.K., Filho, J.O.A., da Silva, A.M.M., Franco, A.R., 2015. Evaluating the reliability of different preprocessing steps to estimate graph theoretical measures in resting state fMRI data. Front. Neurosci. 9, 1–10. https://doi.org/10.3389/fnins.2015.00048

Barker, P., Golay, X., Zaharchuk, G., 2013. Clinical perfusion MRI: techniques and applications. Cambridge University Press, Cambridge.

Barrat, A., Weigt, M., 2000. On the properties of small-world network models. Eur. Phys. J. B. https://doi.org/10.1007/s100510050067

Bassett, D., Bullmore, E., 2017. Small-World Brain Networks Revisited. Neuroscientist 23, 499–516. https://doi.org/10.1177/1073858416667720

Behzadi, Y., Restom, K., Liau, J., Liu, T., 2007. A component based noise correction method (CompCor) for BOLD and perfusion based fMRI. Neuroimage 37, 90–101. https://doi.org/10.1016/j.neuroimage.2007.04.042

Belliveau, J., Kennedy, D., McKinstry, R., Buchbinder, B., Weisskoff, R., Cohen, M., Vevea, J., Brady, T., Rosen, B., 1991. Functional mapping of the human visual cortex by magnetic resonance imaging. Science (80-.). 254, 716–719. https://doi.org/10.1126/science.1948051

Bennett, C.M., Miller, M.B., 2010. How reliable are the results from functional magnetic resonance imaging? Ann. N. Y. Acad. Sci. https://doi.org/10.1111/j.1749-6632.2010.05446.x

Bießmann, F., Plis, S., Meinecke, F., Eichele, T., Müller, K., 2011. Analysis of multimodal neuroimaging data. IEEE Rev. Biomed. Eng. 4, 26–58. https://doi.org/10.1109/RBME.2011.2170675

Birn, R., Molloy, E., Patriat, R., Parker, T., Meier, T., Kirk, G., Nair, V., Meyerand, E., Prabhakaran, V., 2013. The effect of scan length on the reliability of resting-state fMRI connectivity estimates. Neuroimage. https://doi.org/10.1016/j.neuroimage.2013.05.099

Birn, R., Murphy, K., Bandettini, P., 2008. The effect of respiration variations on independent component analysis results of resting state functional connectivity. Hum. Brain Mapp. 29, 740–750. https://doi.org/10.1002/hbm.20577

Biswal, B., Yetkin, Z., Haughton, V., Hyde, J., 1995. Functional connectivity in the motor cortex of resting human brain using echo-planar MRI. Magn. Reson. Med. 34, 537–41. https://doi.org/10.1002/mrm.1910340409

Boissoneault, J., Letzen, J., Lai, S., O'Shea, A., Craggs, J., Robinson, M., Staud, R., 2016. Abnormal resting state functional connectivity in patients with chronic fatigue syndrome: An arterial spin-labeling fMRI study. Magn. Reson. Imaging 34, 603–608. https://doi.org/10.1016/j.mri.2015.12.008

Borogovac, A., Asllani, I., 2012. Arterial spin labeling (ASL) fMRI: Advantages, theoretical constrains and experimental challenges in neurosciences. Int. J. Biomed. Imaging 2012. https://doi.org/10.1155/2012/818456

Bouix, S., Swago, S., West, J.D., Pasternak, O., Breier, A., Shenton, M.E., 2017. "Evaluating acquisition time of rfmri in the human connectome project for early psychosis. How much is enough?," in: Lecture Notes in Computer Science (Including Subseries Lecture Notes in Artificial Intelligence and Lecture Notes in Bioinformatics). pp. 108–115. https://doi.org/10.1007/978-3-319-67159-8_13

Braun, U., Plichta, M.M., Esslinger, C., Sauer, C., Haddad, L., Grimm, O., Mier, D., Mohnke, S., Heinz, A., Erk, S., Walter, H., Seiferth, N., Kirsch, P., Meyer-Lindenberg, A., 2012. Test–retest reliability of resting-state connectivity network characteristics using fMRI and graph theoretical measures. Neuroimage 59, 1404–1412. https://doi.org/10.1016/j.neuroimage.2011.08.044

Breasted, J., 1930. The Edwin smith surgical papyrus, FACSIMILE AND HIEROGLYPHIC TRANSLITERATION WITH TRANSLATION AND COMMENTARY IN TWO VOLUMES. THE UNIVERSITY OF CHICAGO PRESS CHICAGO, ILLINOIS.

Brett, M., Johnsrude, I.S., Owen, A.M., 2002. The problem of functional localization in the human brain. Nat. Rev. Neurosci. https://doi.org/10.1038/nrn756

Broyd, S.J., Demanuele, C., Debener, S., Helps, S.K., James, C.J., Sonuga-Barke, E.J.S., 2009. Default-mode brain dysfunction in mental disorders: A systematic review. Neurosci. Biobehav. Rev. https://doi.org/10.1016/j.neubiorev.2008.09.002

Bruce Fye, W., 1995. Julien Jean César Legallois. Clin. Cardiol. https://doi.org/10.1002/clc.4960181015

Buckner, R., Carroll, D., 2007. Self-projection and the brain. Trends Cogn. Sci. 11, 49–57. https://doi.org/10.1016/j.tics.2006.11.004

Bullmore, E., Sporns, O., 2009. Complex brain networks: Graph theoretical analysis of structural and functional systems. Nat. Rev. Neurosci. https://doi.org/10.1038/nrn2575

Butler, E., Chin, M., Aneman, A., 2017. Peripheral Near-Infrared Spectroscopy: Methodologic Aspects and a Systematic Review in Post-Cardiac Surgical Patients. J. Cardiothorac. Vasc. Anesth. 31, 1407–1416. https://doi.org/10.1053/j.jvca.2016.07.035

Buxton, R., 2005. Quantifying CBF with arterial spin labeling. J. Magn. Reson. Imaging 22, 723–726. https://doi.org/10.1002/jmri.20462

Buxton, R., Frank, L., Wong, E., Siewert, B., Warach, S., Edelman, R., 1998. A general kinetic model for quantitative perfusion imaging with arterial spin labeling.

Mag. Res. Med. 40, 383–396.

Buxton, R.B., 2001. The elusive initial dip. Neuroimage 13, 953–958. https://doi.org/10.1006/nimg.2001.0814

Bzdok, D., Heeger, A., Langner, R., Laird, A.R., Fox, P.T., Palomero-Gallagher, N., Vogt, B.A., Zilles, K., Eickhoff, S.B., 2015. Subspecialization in the human posterior medial cortex. Neuroimage 106, 55–71. https://doi.org/10.1016/j.neuroimage.2014.11.009

Calhoun, V.D., Adali, T., Pearlson, G.D., Pekar, J.J., 2001. A method for making group inferences from functional MRI data using independent component analysis. Hum. Brain Mapp. 14, 140–151. https://doi.org/10.1002/hbm.1048

Carp, J., 2012. On the Plurality of (Methodological) Worlds: Estimating the Analytic Flexibility of fMRI Experiments. Front. Neurosci. 6, 1–13. https://doi.org/10.3389/fnins.2012.00149

Chen, J., Jann, K., Wang, D., 2015. Characterizing Resting-State Brain Function Using Arterial Spin Labeling. Brain Connect. 5, 527–542. https://doi.org/10.1089/brain.2015.0344

Chen, J.E., Glover, G.H., 2015. BOLD fractional contribution to resting-state functional connectivity above 0.1Hz. Neuroimage. https://doi.org/10.1016/j.neuroimage.2014.12.012

Chuang, K., Van Gelderen, P., Merkle, H., Bodurka, J., Ikonomidou, V., Koretsky, A., Duyn, J., Talagala, L., 2009. Mapping resting-state functional connectivity using perfusion MRI. Neuroimage 40, 1595–1605. https://doi.org/10.1016/j.neuroimage.2008.01.006

Cleveland, W., Devlin, S., 1988. Locally Weighted Regression: An Approach to Regression Analysis by Local Fitting. J. Am. Stat. Assoc. 83, 596. https://doi.org/10.2307/2289282

Cohen, A.D., Nencka, A.S., Wang, Y., 2018. Multiband multi-echo simultaneous ASL/ BOLD for task-induced functional MRI. PLoS One 13, 1–21. https://doi.org/10.1371/journal.pone.0190427

Cole, D., Smith, S., Beckmann, C., 2010. Advances and pitfalls in the analysis and interpretation of resting-state FMRI data. Front. Syst. Neurosci. 4, 8. https://doi.org/10.3389/fnsys.2010.00008

Comon, P., 1994. Independent component analysis, A new concept? Signal Processing 36, 287–314. https://doi.org/10.1016/0165-1684(94)90029-9

Cordes, D., Haughton, V., Carew, J., Arfanakis, K., Maravilla, K., 2002. Hierarchical clustering to measure connectivity in fMRI resting-state data. Magn. Reson. Imaging 20, 305–317. https://doi.org/10.1016/S0730-725X(02)00503-9

Cramér, H., 1947. Mathematical Methods of Statistics. Biometrika 34, 374. https://doi.org/10.2307/2332454

Cruz-Gómez, Á.J., Ventura-Campos, N., Belenguer, A., Ávila, C., Forn, C., 2014. The link between resting-state functional connectivity and cognition in MS patients. Mult. Scler. J. https://doi.org/10.1177/1352458513495584

D'haeseleer, M., Cambron, M., Vanopdenbosch, L., De Keyser, J., 2011. Vascular aspects of multiple sclerosis. Lancet Neurol. 10, 657–666. https://doi.org/10.1016/S1474-4422(11)70105-3

Dai, W., Garcia, D., De Bazelaire, C., Alsop, D.C., 2008. Continuous flow-driven inversion for arterial spin labeling using pulsed radio frequency and gradient fields. Magn. Reson. Med. 60, 1488–1497. https://doi.org/10.1002/mrm.21790

Dai, W., Varma, G., Scheidegger, R., Alsop, D., 2016. Quantifying fluctuations of resting state networks using arterial spin labeling perfusion MRI. J. Cereb. Blood Flow Metab. 36, 463–473. https://doi.org/10.1177/0271678X15615339

Dale, A.M., Buckner, R.L., 1997. Selective averaging of individual trials using fMRI. Neuroimage 5, 329–340.

Damoiseaux, J.S., Rombouts, S.A.R.B., Barkhof, F., Scheltens, P., Stam, C.J., Smith, S.M., Beckmann, C.F., 2006. Consistent resting-state networks across healthy subjects. Proc. Natl. Acad. Sci. U. S. A. 103, 13848–13853. https://doi.org/10.1073/pnas.0601417103

De Luca, M., Beckmann, C., De Stefano, N., Matthews, P.M., Smith, S.M., 2006. fMRI resting state networks define distinct modes of long-distance interactions in the human brain. Neuroimage 29, 1359–1367. https://doi.org/10.1016/j.neuroimage.2005.08.035

De Luca, M., Smith, S., De Stefano, N., Federico, A., Matthews, P.M., 2005. Blood oxygenation level dependent contrast resting state networks are relevant to functional activity in the neocortical sensorimotor system. Exp. Brain Res. 167, 587–594. https://doi.org/10.1007/s00221-005-0059-1

Detre, J.A., Leigh, J.S., Williams, D.S., Koretsky, A.P., 1992. Perfusion imaging. Magn. Reson. Med. 23, 37–45. https://doi.org/10.1002/mrm.1910230106

Detre, J.A., Wang, J., 2002. Technical aspects and utility of fMRI using BOLD and ASL. Clin. Neurophysiol. 113, 621–634. https://doi.org/10.1016/S1388-2457(02)00038-X

Duong, T.Q., Kim, D.S., Uğurbil, K., Kim, S.G., 2001. Localized cerebral blood flow response at submillimeter columnar resolution. Proc. Natl. Acad. Sci. U. S. A. 98, 10904–10909. https://doi.org/10.1073/pnas.191101098

Eklund, A., Nichols, T., Knutsson, H., 2016. Cluster failure: Why fMRI inferences for spatial extent have inflated false-positive rates. Proc. Natl. Acad. Sci. 113, E4929–E4929. https://doi.org/10.1073/pnas.1612033113

Essig, M., Shiroishi, M.S., Nguyen, T.B., Saake, M., Provenzale, J.M., Enterline, D., Anzalone, N., Dörfler, A., Rovira, À., Wintermark, M., Law, M., 2013. Perfusion MRI: The Five Most Frequently Asked Technical Questions. Am. J. Roentgenol. 200, 24–34. https://doi.org/10.2214/AJR.12.9543

Faivre, A., Rico, A., Zaaraoui, W., Crespy, L., Reuter, F., Wybrecht, D., Soulier, E., Malikova, I., Confort-Gouny, S., Cozzone, P.J., Pelletier, J., Ranjeva, J.P., Audoin, B., 2012. Assessing brain connectivity at rest is clinically relevant in

early multiple sclerosis. Mult. Scler. J. https://doi.org/10.1177/1352458511435930

Fan, L., Li, H., Zhuo, J., Zhang, Y., Wang, J., Chen, L., Yang, Z., Chu, C., Xie, S., Laird, A.R., Fox, P.T., Eickhoff, S.B., Yu, C., Jiang, T., 2016. The Human Brainnetome Atlas: A New Brain Atlas Based on Connectional Architecture. Cereb. Cortex 26, 3508–3526. https://doi.org/10.1093/cercor/bhw157

Filippi, M., Agosta, F., Spinelli, E.G., Rocca, M.A., 2013. Imaging resting state brain function in multiple sclerosis. J. Neurol. https://doi.org/10.1007/s00415-012-6695-z

Fox, M., Raichle, M., 2007. Spontaneous fluctuations in brain activity observed with functional magnetic resonance imaging. Nat Rev Neurosci 8, 700–711. https://doi.org/10.1038/nrn2201

Francis, S.T., Bowtell, R., Gowland, P.A., 2008. Modeling and optimization of look-locker spin labeling for measuring perfusion and transit time changes in activation studies taking into account arterial blood volume. Magn. Reson. Med. 59, 316–325. https://doi.org/10.1002/mrm.21442

Friston, K.J., Ashburner, J., Frith, C.D., Poline, J. -B, Heather, J.D., Frackowiak, R.S.J., 1995. Spatial registration and normalization of images. Hum. Brain Mapp. https://doi.org/10.1002/hbm.460030303

Friston, K.J., Frith, C.D., Liddle, P.F., Frackowiak, R.S.J., 1993. Functional connectivity: The principal-component analysis of large (PET) data sets. J. Cereb. Blood Flow Metab. 13, 5–14. https://doi.org/10.1038/jcbfm.1993.4

Gai, N.D., Butman, J.A., 2019. Determining the optimal postlabeling delay for arterial spin labeling using subject-specific estimates of blood velocity in the carotid artery. J. Magn. Reson. Imaging 50, 951–960. https://doi.org/10.1002/jmri.26670

Gargouri, F., Kallel, F., Delphine, S., Hamida, A. Ben, Lehéricy, S., Valabregue, R., 2018. The influence of preprocessing steps on graph theory measures derived from resting state fMRI. Front. Comput. Neurosci. 12. https://doi.org/10.3389/fncom.2018.00008

Gawryluk, J.R., Mazerolle, E.L., D'Arcy, R.C.N., 2014. Does functional MRI detect activation in white matter? A review of emerging evidence, issues, and future directions. Front. Neurosci. 8, 1–12. https://doi.org/10.3389/fnins.2014.00239

Gholipour, A., Kehtarnavaz, N., Briggs, R., Devous, M., Gopinath, K., 2007. Brain Functional Localization: A Survey of Image Registration Techniques. IEEE Trans. Med. Imaging 26, 427–451. https://doi.org/10.1109/TMI.2007.892508

Glover, G., Tie-Qiang, L., David, R., 2000. Image-Based Method for Retrospective Correction of Physiological Motion Effects in fMRI : RETROICOR. Magn. Reson. Med. 167, 162–167.

Golay, X., Stuber, M., Pruessmann, K.P., Meier, D., Boesiger, P., 1999. Transfer insensitive labeling technique (TILT): Application to multislice functional perfusion imaging. J. Magn. Reson. Imaging 9, 454–461.

https://doi.org/10.1002/(SICI)1522-2586(199903)9:3<454::AID-JMRI14>3.0.CO;2-B

Gordon, Y., Partovi, S., Müller-Eschner, M., Amarteifio, E., Bäuerle, T., Weber, M.-A., Kauczor, H.-U., Rengier, F., 2014. Dynamic contrast-enhanced magnetic resonance imaging: fundamentals and application to the evaluation of the peripheral perfusion. Cardiovasc. Diagn. Ther. 4, 147–14764. https://doi.org/10.3978/j.issn.2223-3652.2014.03.01

Grade, M., Hernandez Tamames, J.A., Pizzini, F., Achten, E., Golay, X., Smits, M., 2015. A neuroradiologist's guide to arterial spin labeling MRI in clinical practice. Neuroradiology 57, 1181–1202. https://doi.org/10.1007/s00234-015-1571-z

Greicius, M., 2008. Resting-state functional connectivity in neuropsychiatric disorders. Curr. Opin. Neurol. https://doi.org/10.1097/wco.0b013e328306f2c5

Greicius, M., Supekar, K., Menon, V., Dougherty, R., 2009. Resting-state functional connectivity reflects structural connectivity in the default mode network. Cereb. Cortex 19, 72–78. https://doi.org/10.1093/cercor/bhn059

Gross, C.G., 1987. Early History of Neuroscience. Encycl. Neurosci.

Hahn, E.L., 1950. Spin echoes. Phys. Rev. https://doi.org/10.1103/PhysRev.80.580

Hämäläinen, M., Hari, R., Ilmoniemi, R.J., Knuutila, J., Lounasmaa, O. V., 1993. Magnetoencephalography theory, instrumentation, and applications to noninvasive studies of the working human brain. Rev. Mod. Phys. 65, 413–497. https://doi.org/10.1103/RevModPhys.65.413

Harms, M.P., Melcher, J.R., 2002. Sound repetition rate in the human auditory pathway: Representations in the waveshape and amplitude of fMRI activation. J. Neurophysiol. 88, 1433–1450. https://doi.org/10.1152/jn.2002.88.3.1433

Hayasaka, S., Laurienti, P., 2011. Comparison of Characteristics between Region- and Voxel-Based Network Analyses in Resting-State fMRI Data. Neuroimage 18, 499–508. https://doi.org/10.1016/j.str.2010.08.012.Structure

Henry, J.C., 2006. Electroencephalography: Basic Principles, Clinical Applications, and Related Fields, Fifth Edition. Neurology. https://doi.org/10.1212/01.wnl.0000243257.85592.9a

Henson, R., Büchel, C., Josephs, O., Fristen, K., 1999. The slice-timing problem in event-related fMRI. Neuroimage.

Himberg, J., Hyvärinen, A., 2003. ICASSO: Software for investigating the reliability of ICA estimates by clustering and visualization. Neural Networks Signal Process. - Proc. IEEE Work. 2003-Janua, 259–268. https://doi.org/10.1109/NNSP.2003.1318025

Hirsch, J., 2012. Brain mapping for neurosurgery and cognitive neuroscience. Funct. Neuroradiol. Princ. Clin. Appl. 513–543. https://doi.org/10.1007/978-1-4419-0345-7_27

Hirsch, J., 2006. Brain Mapping for Neurosurgery and Cognitive Neuroscience, in:

Functional MRI. Springer New York, New York, NY, pp. 139–182. https://doi.org/10.1007/0-387-34665-1_7

Horwitz, B., McIntosh, A.R., Haxby, J. V., Grady, C.L., 1995. Network analysis of brain cognitive function using metabolic and blood flow data. Behav. Brain Res. 66, 187–193. https://doi.org/10.1016/0166-4328(94)00139-7

Huneau, C., Benali, H., Chabriat, H., 2015. Investigating human neurovascular coupling using functional neuroimaging: A critical review of dynamic models. Front. Neurosci. 9, 1–12. https://doi.org/10.3389/fnins.2015.00467

Hyvärinen, A., 1999a. Survey on Independent Component Analysis Aapo 94–128.

Hyvärinen, A., 1999b. Fast and robust fixed-point algorithms for independent component analysis. IEEE Trans. Neural Networks 10, 626–634. https://doi.org/10.1109/72.761722

Iraji, A., Calhoun, V., Wiseman, N., Davoodi-Bojd, E., Avanaki, M., Haacke, M., Kou, Z., 2016. The connectivity domain: Analyzing resting state fMRI data using feature-based data-driven and model-based methods. Neuroimage 134, 494–507. https://doi.org/10.1016/j.neuroimage.2016.04.006

Jahng, G.H., Zhu, X.P., Matson, G.B., Weiner, M.W., Schuff, N., 2003. Improved perfusion-weighted MRI by a novel double inversion with proximal labeling of both tagged and control acquisitions. Magn. Reson. Med. 49, 307–314. https://doi.org/10.1002/mrm.10339

Jann, K., Gee, D., Kilroy, E., Schwab, S., Smith, R., Cannon, T., Wang, D., 2015. Functional connectivity in BOLD and CBF data: SIMILARITY and reliability of resting brain networks. Neuroimage 106, 111–122. https://doi.org/10.1016/j.neuroimage.2014.11.028

Jutten, C., Karhunen, J., 2004. Advances in blind source separation (BSS) and independent component analysis (ICA) for nonlinear mixtures. Int. J. Neural Syst. 14, 267–292. https://doi.org/10.1142/S012906570400208X

Kemeny, S., Ye, F.Q., Birn, R., Braun, A.R., 2005. Comparison of continuous overt speech fMRI using BOLD and arterial spin labeling. Hum. Brain Mapp. 24, 173–183. https://doi.org/10.1002/hbm.20078

Kernbach, J.M., Thomas Yeo, B.T., Smallwood, J., Margulies, D.S., De Schotten, M.T., Walter, H., Sabuncu, M.R., Holmes, A.J., Gramfort, A., Varoquaux, G., Thirion, B., Bzdok, D., 2018. Subspecialization within default mode nodes characterized in 10,000 UK Biobank participants. Proc. Natl. Acad. Sci. U. S. A. 115, 12295–12300. https://doi.org/10.1073/pnas.1804876115

Kim, S.G., Bandettini, P.A., 2006. Principles of functional MRI, in: Functional MRI: Basic Principles and Clinical Applications. https://doi.org/10.1007/0-387-34665-1_1

Kim, S.G., Ugurbil, K., 1997. Functional magnetic resonance imaging of the human brain. J. Neurosci. Methods 74, 229–243. https://doi.org/10.1016/S0165-0270(97)02252-8

Kindler, J., Jann, K., Homan, P., Hauf, M., Walther, S., Strik, W., Dierks, T., Hubl, D.,

2015. Static and dynamic characteristics of cerebral blood flow during the resting state in schizophrenia. Schizophr. Bull. 41, 163–170. https://doi.org/10.1093/schbul/sbt180

Kiviniemi, V., Kantola, J.H., Jauhiainen, J., Hyvärinen, A., Tervonen, O., 2003. Independent component analysis of nondeterministic fMRI signal sources. Neuroimage. https://doi.org/10.1016/S1053-8119(03)00097-1

Laumann, T.O., Gordon, E.M., Adeyemo, B., Snyder, A.Z., Joo, S.J., Chen, M.Y., Gilmore, A.W., McDermott, K.B., Nelson, S.M., Dosenbach, N.U.F., Schlaggar, B.L., Mumford, J.A., Poldrack, R.A., Petersen, S.E., 2015. Functional System and Areal Organization of a Highly Sampled Individual Human Brain. Neuron 87, 657–670. https://doi.org/10.1016/j.neuron.2015.06.037

Lee, H.L., Zahneisen, B., Hugger, T., LeVan, P., Hennig, J., 2013. Tracking dynamic resting-state networks at higher frequencies using MR-encephalography. Neuroimage. https://doi.org/10.1016/j.neuroimage.2012.10.015

Lee, M., Smyser, Shimony, 2013. Resting-state fMRI: A review of methods and clinical applications. Am. J. Neuroradiol. 34, 1866–1872. https://doi.org/10.3174/ajnr.A3263

Leech, R., Kamourieh, S., Beckmann, C.F., Sharp, D.J., 2011. Fractionating the default mode network: Distinct contributions of the ventral and dorsal posterior cingulate cortex to cognitive control. J. Neurosci. 31, 3217–3224. https://doi.org/10.1523/JNEUROSCI.5626-10.2011

Leontiev, O., Buxton, R.B., 2007. Reproducibility of BOLD, perfusion, and CMRO2 measurements with calibrated-BOLD fMRI. Neuroimage 35, 175–184. https://doi.org/10.1016/j.neuroimage.2006.10.044

Leskovec, J., Horvitz, E., 2008. Planetary-scale views on a large instant-messaging network, in: Proceeding of the 17th International Conference on World Wide Web 2008, WWW'08. https://doi.org/10.1145/1367497.1367620

Li, W., Antuono, P., Xie, C., Chen, G., Jones, J., Ward, D., Franczak, M., Goveas, J., Li, S., 2012. Changes in regional cerebral blood flow and functional connectivity in the cholinergic pathway associated with cognitive performance in subjects with mild Alzheimer's disease after 12-week donepezil treatment. Neuroimage 60, 1083–1091. https://doi.org/10.1016/j.neuroimage.2011.12.077.Changes

Liang, X., Connelly, A., Calamante, F., 2014. Graph analysis of resting-state ASL perfusion MRI data: Nonlinear correlations among CBF and network metrics. Neuroimage 87, 265–275. https://doi.org/10.1016/j.neuroimage.2013.11.013

Liang, X., Wang, J., Yan, C., Shu, N., Xu, K., Gong, G., He, Y., 2012. Effects of different correlation metrics and preprocessing factors on small-world brain functional networks: A resting-state functional MRI study. PLoS One. https://doi.org/10.1371/journal.pone.0032766

Liang, X., Zou, Q., He, Y., Yang, Y., 2013. Coupling of functional connectivity and regional cerebral blood flow reveals a physiological basis for network hubs of

the human brain. Proc Natl Acad Sci U S A 110, 1929–1934. https://doi.org/10.1073/pnas.1214900110

Liu, T., Brown, G., 2007. Measurement of cerebral perfusion with arterial spin labeling: Part 1. Methods. J. Int. Neuropsychol. Soc. 13, 517–525. https://doi.org/10.1017/s1355617707070646

Liu, T., Wong, E., 2005. A signal processing model for arterial spin labeling functional MRI. Neuroimage 24, 207–215. https://doi.org/10.1016/j.neuroimage.2004.09.047

Logothetis, N.K., Pauls, J., Augath, M., Trinath, T., Oeltermann, A., 2001. Neurophysiological investigation of the basis of the fMRI signal. Nature 412, 150–157. https://doi.org/10.1038/35084005

Lopes da Silva, F., 2013. EEG and MEG: Relevance to neuroscience. Neuron 80, 1112–1128. https://doi.org/10.1016/j.neuron.2013.10.017

Lowe, M.J., Mock, B.J., Sorenson, J.A., 1998. Functional connectivity in single and multislice echoplanar imaging. Neuroimage 7, 119–132.

Luh, W.M., Wong, E., Bandettini, P., Ward, D., Hyde, J., 2000. Comparison of simultaneously measured perfusion and bold signal increases during brain activation with T1-based tissue identification. Magn. Reson. Med. 44, 137–143. https://doi.org/10.1002/1522-2594(200007)44:1<137::AID-MRM20>3.0.CO;2-R

Lynall, M.-E., Bassett, D., Kerwin, R., McKenna, P.J., Kitzbichler, M., Muller, U., Bullmore, E., 2010. Functional Connectivity and Brain Networks in Schizophrenia. J. Neurosci. 30, 9477–9487. https://doi.org/10.1523/JNEUROSCI.0333-10.2010

Marcus, C., Mena, E., Subramaniam, R.M., 2014. Brain PET in the diagnosis of Alzheimer's disease. Clin. Nucl. Med. 39, e413–e426. https://doi.org/10.1097/RLU.0000000000000547

McKeown, M., Hansen, L., Sejnowski, T., 2003. Independent component analysis of functional MRI: What is signal and what is noise? Curr. Opin. Neurobiol. 13, 620–629. https://doi.org/10.1016/j.conb.2003.09.012

Mitra, A., Snyder, A.Z., Hacker, C.D., Raichle, M.E., 2014. Lag structure in resting-state fMRI. J. Neurophysiol. 111, 2374–2391. https://doi.org/10.1152/jn.00804.2013

Mohammadi, B., Kollewe, K., Samii, A., Krampfl, K., Dengler, R., Münte, T.F., 2009. Changes of resting state brain networks in amyotrophic lateral sclerosis. Exp. Neurol. https://doi.org/10.1016/j.expneurol.2009.01.025

Mulders, P., van Eijndhoven, P., Schene, A., Beckmann, C., Tendolkar, I., 2015. Resting-state functional connectivity in major depressive disorder: A review. Neurosci. Biobehav. Rev. 56, 330–344. https://doi.org/10.1016/j.neubiorev.2015.07.014

Muraskin, J., Ooi, M.B., Goldman, R.I., Krueger, S., Thomas, W.J., Sajda, P., Brown, T.R., 2013. Prospective active marker motion correction improves statistical

power in BOLD fMRI. Neuroimage. https://doi.org/10.1016/j.neuroimage.2012.11.052

Mutsaerts, H., Nordhøy, W., Pizzini, F., van Osch, M., Zelaya, F., Hendrikse, J., Wastling, S., Petersen, E.T., Günther, M., Wang, Y., Geier, O., Fernandez-Seara, M., Golay, X., Wang, D., Fallatah, S., Nederveen, A., Groote, I., Bjørnerud, A., 2015. Multi-vendor reliability of arterial spin labeling perfusion MRI using a near-identical sequence: Implications for multi-center studies. Neuroimage 113, 143–152. https://doi.org/10.1016/j.neuroimage.2015.03.043

Nordin, L.E., Li, T.Q., Brogren, J., Johansson, P., Sjögren, N., Hannesdottir, K., Björk, C., Segerdahl, M., Wang, D.J.J., Julin, P., 2013. Cortical responses to amphetamine exposure studied by pCASL MRI and pharmacokinetic/pharmacodynamic dose modeling. Neuroimage. https://doi.org/10.1016/j.neuroimage.2012.11.035

Ogawa, S., Tank, D.W., Menon, R., Ellermann, J.M., Kim, S.G., Merkle, H., Ugurbil, K., 1992. Intrinsic signal changes accompanying sensory stimulation: Functional brain mapping with magnetic resonance imaging. Proc. Natl. Acad. Sci. U. S. A. 89, 5951–5955. https://doi.org/10.1073/pnas.89.13.5951

Olafsson, V., Kundu, P., Wong, E., Bandettini, P., Liu, T., 2015. Enhanced identification of BOLD-like components with multi-echo simultaneous multi-slice (MESMS) fMRI and multi-echo ICA. Neuroimage 112, 43–51. https://doi.org/10.1016/j.neuroimage.2015.02.052

Østergaard, L., 2005. Principles of cerebral perfusion imaging by bolus tracking. J. Magn. Reson. Imaging 22, 710–717. https://doi.org/10.1002/jmri.20460

Pajula, J., Tohka, J., 2014. Effects of spatial smoothing on inter-subject correlation based analysis of FMRI. Magn. Reson. Imaging. https://doi.org/10.1016/j.mri.2014.06.001

Parker, D., Liu, X., Razlighi, Q.R., 2017. Optimal slice timing correction and its interaction with fMRI parameters and artifacts. Med. Image Anal. 35, 434–445. https://doi.org/10.1016/j.media.2016.08.006

Parker, D.B., Razlighi, Q.R., 2019. The benefit of slice timing correction in common fMRI preprocessing pipelines. Front. Neurosci. 13. https://doi.org/10.3389/fnins.2019.00821

Parkes, L., Detre, J., 2003. ASL: Blood Perfusion Measurements Using Arterial Spin Labelling. Quant. MRI Brain Meas. Chang. Caused by Dis. https://doi.org/10.1002/0470869526.ch13

Parkes, L.M., Tofts, P.S., 2002. Improved accuracy of human cerebral blood perfusion measurements using arterial spin labeling: Accounting for capillary water permeability. Magn. Reson. Med. 48, 27–41. https://doi.org/10.1002/mrm.10180

Patriat, R., Molloy, E., Meier, T., Kirk, G., Nair, V., Meyerand, M., Prabhakaran, V., Birn, R., 2013. The effect of resting condition on resting-state fMRI reliability and consistency: A comparison between resting with eyes open, closed, and fixated. Neuroimage 78, 463–473.

https://doi.org/10.1016/j.neuroimage.2013.04.013

Paya, C., Corouge, I., Banniera, E., Gentric, J.-C., Ferré, J.-C., 2018. Pre-neurosurgical detection of cerebral motor areas by functional MRI: Comparison between Blood Oxygenation Level (BOLD) and functional Arterial Spin Labeling (fASL) techniques. J. Neuroradiol. 45, 79. https://doi.org/10.1016/j.neurad.2018.01.040

Peer, M., Nitzan, M., Bick, A., Levin, N., Arzy, S., 2017. Evidence for Functional Networks within the Human Brain's White Matter. J. Neurosci. 37, 6394–6407. https://doi.org/10.1523/JNEUROSCI.3872-16.2017

Pimentel, M.A.F., Vilela, P., Sousa, I., Figueiredo, P., 2013. Localization of the hand motor area by arterial spin labeling and blood oxygen level-dependent functional magnetic resonance imaging. Hum. Brain Mapp. 34, 96–108. https://doi.org/10.1002/hbm.21418

Poldrack, R., Mumford, J., Nichols, T., 2011. Handbook of functional MRI data analysis. Cambridge University Press.

Power, J., 2017. A simple but useful way to assess fMRI scan qualities. Neuroimage 154, 150–158. https://doi.org/10.1016/j.neuroimage.2016.08.009

Power, J.D., Barnes, K.A., Snyder, A.Z., Schlaggar, B.L., Petersen, S.E., 2012. Spurious but systematic correlations in functional connectivity MRI networks arise from subject motion. Neuroimage. https://doi.org/10.1016/j.neuroimage.2011.10.018

Pruim, R., Mennes, M., Buitelaar, J., Beckmann, C., 2015. Evaluation of ICA-AROMA and alternative strategies for motion artifact removal in resting state fMRI. Neuroimage 112, 278–287. https://doi.org/10.1016/j.neuroimage.2015.02.063

Raichle, M., MacLeod, A.-M., Snyder, A., Powers, W., Gusnard, D., Shulman, G., 2001. A default mode of brain function. Proc. Natl. Acad. Sci. U. S. A. 98, 676–82. https://doi.org/10.1073/pnas.98.2.676

Raichle, M.E., Mintun, M.A., 2006. Brain Work and Brain Imaging. Annu. Rev. Neurosci. 29, 449–476. https://doi.org/10.1146/annurev.neuro.29.051605.112819

Raichle, M.E., Shepherd, G.M., 2014. Angelo Mosso's Circulation of Blood in the Human Brain, Angelo Mosso's Circulation of Blood in the Human Brain. https://doi.org/10.1093/med/9780199358984.001.0001

Raoult, H., Petr, J., Bannier, É., Stamm, A., Gauvrit, J.-Y., Barillot, C., Ferré, J.-C., 2011. Arterial spin labeling for motor activation mapping at 3T with a 32-channel coil: Reproducibility and spatial accuracy in comparison with BOLD fMRI. Neuroimage 58, 157–167. https://doi.org/10.1016/j.neuroimage.2011.06.011

Restom, K., Behzadi, Y., Liu, T., 2006. Physiological noise reduction for arterial spin labeling functional MRI. Neuroimage 31, 1104–1115. https://doi.org/10.1016/j.neuroimage.2006.01.026

Roy, C.S., Sherrington, C.S., 1890. On the Regulation of the Blood-supply of the Brain. J. Physiol. 11, 85–158. https://doi.org/10.1113/jphysiol.1890.sp000321

Ruppert, D., 2002. Selecting the number of knots for penalized splines. J. Comput. Graph. Stat. https://doi.org/10.1198/106186002853

Salimi-Khorshidi, G., Douaud, G., Beckmann, C., Glasser, M., Griffanti, L., Smith, S., 2014. Automatic denoising of functional MRI data: Combining independent component analysis and hierarchical fusion of classifiers. Neuroimage 90, 449–468. https://doi.org/10.1016/j.neuroimage.2013.11.046

Salvador, R., Suckling, J., Coleman, M., Pickard, J., Menon, D., Bullmore, E., 2005. Neurophysiological architecture of functional magnetic resonance images of human brain. Cereb. Cortex 15, 1332–2342. https://doi.org/10.1093/cercor/bhi016

Sanz-Arigita, E., Schoonheim, M., Damoiseaux, J., Rombouts, S., Maris, E., Barkhof, F., Scheltens, P., Stam, C., 2010. Loss of "Small-World" Networks in Alzheimer's Disease: Graph Analysis of fMRI Resting-State Functional Connectivity. PLoS One 5. https://doi.org/10.1371/journal.pone.0013788

Sejnowski, T., Bell, A., 1995. Information-Maximization Approach to Blind Separation and Blind Deconvolution. Technology 1159, 1129–1159.

Shehzad, Z., Kelly, A.M.C., Reiss, P.T., Gee, D.G., Gotimer, K., Uddin, L.Q., Lee, S.H., Margulies, D.S., Roy, A.K., Biswal, B.B., Petkova, E., Castellanos, F.X., Milham, M.P., 2009. The Resting Brain: Unconstrained yet Reliable. Cereb. Cortex 19, 2209–2229. https://doi.org/10.1093/cercor/bhn256

Sheth, S.A., Nemoto, M., Guiou, M., Walker, M., Pouratian, N., Toga, A.W., 2004. Linear and nonlinear relationships between neuronal activity, oxygen metabolism, and hemodynamic responses. Neuron 42, 347–355. https://doi.org/10.1016/S0896-6273(04)00221-1

Silva, A.C., Kim, S.G., 1999. Pseudo-continuous arterial spin labeling technique for measuring CBF dynamics with high temporal resolution. Magn. Reson. Med. 42, 425–429. https://doi.org/10.1002/(SICI)1522-2594(199909)42:3<425::AID-MRM3>3.0.CO;2-S

Silvestre, C., Figueiredo, P., Rosa, P., 2010. On the distinguishability of HRF Models in fMRI, in: 2010 Annual International Conference of the IEEE Engineering in Medicine and Biology Society, EMBC'10. https://doi.org/10.1109/IEMBS.2010.5627891

Smith, S., Vidaurre, D., Beckmann, C., Glasser, M., Jenkinson, M., Miller, K., Nichols, T., Robinson, E., Salimi-Khorshidi, G., Woolrich, M., Barch, D., Ugurbil, K., Van Essen, D., 2013. Functional connectomics from resting-state fMRI. Trends Cogn. Sci. 17, 666–682. https://doi.org/10.1016/j.tics.2013.09.016

Stam, C.J., van Straaten, E.C.W., Van Dellen, E., Tewarie, P., Gong, G., Hillebrand, A., Meier, J., Van Mieghem, P., 2016. The relation between structural and functional connectivity patterns in complex brain networks. Int. J. Psychophysiol. https://doi.org/10.1016/j.ijpsycho.2015.02.011

Steketee, R.M.E., Mutsaerts, H.J.M.M., Bron, E.E., Van Osch, M.J.P., Majoie,

C.B.L.M., Van Der Lugt, A., Nederveen, A.J., Smits, M., 2015. Quantitative functional Arterial Spin Labeling (fASL) MRI - Sensitivity and reproducibility of regional CBF changes using pseudo-continuous ASL product sequences. PLoS One 10, 1–17. https://doi.org/10.1371/journal.pone.0132929

Storti, S.F., Formaggio, E., Nordio, R., Manganotti, P., Fiaschi, A., Bertoldo, A., Toffolo, G.M., 2013. Automatic selection of resting-state networks with functional magnetic resonance imaging. Front. Neurosci. 7, 1–10. https://doi.org/10.3389/fnins.2013.00072

Ter-Pogossian, M.M., 1984. Image Reconstruction from Projections, The Fundamentals of Computerized Tomography by G. T. Herman . Med. Phys. https://doi.org/10.1118/1.595466

Termenon, M., Jaillard, A., Delon-Martin, C., Achard, S., 2016. Reliability of graph analysis of resting state fMRI using test-retest dataset from the Human Connectome Project. Neuroimage. https://doi.org/10.1016/j.neuroimage.2016.05.062

Tian, L., Wang, J., Yan, C., He, Y., 2011. Hemisphere- and gender-related differences in small-world brain networks: A resting-state functional MRI study. Neuroimage 54, 191–202. https://doi.org/10.1016/j.neuroimage.2010.07.066

Tjandra, T., Brooks, J.C.W., Figueiredo, P., Wise, R., Matthews, P.M., Tracey, I., 2005. Quantitative assessment of the reproducibility of functional activation measured with BOLD and MR perfusion imaging: Implications for clinical trial design. Neuroimage. https://doi.org/10.1016/j.neuroimage.2005.04.021

Tong, Y., Hocke, L.M., Frederick, B.B., 2019. Low frequency systemic hemodynamic “noise” in resting state BOLD fMRI: Characteristics, causes, implications, mitigation strategies, and applications. Front. Neurosci. 13. https://doi.org/10.3389/fnins.2019.00787

Trapp, C., Vakamudi, K., Posse, S., 2018. On the detection of high frequency correlations in resting state fMRI. Neuroimage 164, 202–213. https://doi.org/10.1016/j.neuroimage.2017.01.059

Trojsi, F., Di Nardo, F., Santangelo, G., Siciliano, M., Femiano, C., Passaniti, C., Caiazzo, G., Fratello, M., Cirillo, M., Monsurrò, M.R., Esposito, F., Tedeschi, G., 2017. Resting state fMRI correlates of Theory of Mind impairment in amyotrophic lateral sclerosis. Cortex. https://doi.org/10.1016/j.cortex.2017.09.016

Tsujikawa, T., Kimura, H., Matsuda, T., Fujiwara, Y., Isozaki, M., Kikuta, K.I., Okazawa, H., 2016. Arterial transit time mapping obtained by pulsed continuous 3D ASL imaging with multiple post-label delay acquisitions: Comparative study with PET-CBF in patients with chronic occlusive cerebrovascular disease. PLoS One 11. https://doi.org/10.1371/journal.pone.0156005

Van den Heuvel, M., Hulshoff Pol, H., 2010. Exploring the brain network: A review on resting-state fMRI functional connectivity. Eur. Neuropsychopharmacol.

20, 519–534. https://doi.org/10.1016/j.euroneuro.2010.03.008

Van den Heuvel, M., Mandl, R., Pol, H., 2008. Normalized cut group clustering of resting-state fMRI data. PLoS One 3. https://doi.org/10.1371/journal.pone.0002001

van den Heuvel, M.P., Stam, C.J., Boersma, M., Hulshoff Pol, H.E., 2008. Small-world and scale-free organization of voxel-based resting-state functional connectivity in the human brain. Neuroimage. https://doi.org/10.1016/j.neuroimage.2008.08.010

Van Dijk, K.R.A., Hedden, T., Venkataraman, A., Evans, K.C., Lazar, S.W., Buckner, R.L., 2010. Intrinsic Functional Connectivity As a Tool For Human Connectomics: Theory, Properties, and Optimization. J. Neurophysiol. 103, 297–321. https://doi.org/10.1152/jn.00783.2009

Vaquero, J.J., Kinahan, P., 2015. Positron Emission Tomography: Current Challenges and Opportunities for Technological Advances in Clinical and Preclinical Imaging Systems. Annu. Rev. Biomed. Eng. 17, 385–414. https://doi.org/10.1146/annurev-bioeng-071114-040723

Varoquaux, G., Craddock, C., 2013. Learning and comparing functional connectomes across subjects. Neuroimage 80, 405–415. https://doi.org/10.1016/j.neuroimage.2013.04.007

Varoquaux, G., Gramfort, A., Pedregosa, F., Michel, V., Thirion, B., 2011. Multi-subject dictionary learning to segment an atlas of brain spontaneous activity. Lect. Notes Comput. Sci. (including Subser. Lect. Notes Artif. Intell. Lect. Notes Bioinformatics) 6801 LNCS, 562–573. https://doi.org/10.1007/978-3-642-22092-0_46

Varoquaux, G., Sadaghiani, S., Pinel, P., Kleinschmidt, A., Poline, J.-B., Thirion, B., 2010. A group model for stable multi-subject ICA on fMRI datasets. Neuroimage 51, 288–299. https://doi.org/10.1016/j.neuroimage.2010.02.010

Vidorreta, M., Wang, Z., Rodriguez, I., Pastor, M., Detre, J., Fernandez-Seara, M., 2013. Comparison of 2D and 3D single-shot ASL perfusion fMRI sequences. Neuroimage 66, 662–671. https://doi.org/10.1016/j.neuroimage.2012.10.087

Viviani, R., Messina, I., Walter, M., 2011. Resting state functional connectivity in perfusion imaging: Correlation maps with Bold connectivity and resting state perfusion. PLoS One 6. https://doi.org/10.1371/journal.pone.0027050

Wager, T.D., Vazquez, A., Hernandez, L., Noll, D.C., 2005. Accounting for nonlinear BOLD effects in fMRI: Parameter estimates and a model for prediction in rapid event-related studies. Neuroimage 25, 206–218. https://doi.org/10.1016/j.neuroimage.2004.11.008

Walther, S., Schäppi, L., Federspiel, A., Bohlhalter, S., Wiest, R., Strik, W., Stegmayer, K., 2016. Resting-State Hyperperfusion of the Supplementary Motor Area in Catatonia. Schizophr. Bull. sbw140. https://doi.org/10.1093/schbul/sbw140

Wang, D., Alger, J., Qiao, J., Hao, Q., Hou, S., Fiaz, R., Gunther, M., Pope, W., Saver, J., Salamon, N., Liebeskind, D., 2012. The value of arterial spin-labeled perfusion imaging in acute ischemic stroke: Comparison with dynamic susceptibility contrast-enhanced MRI. Stroke 43, 1018–1024. https://doi.org/10.1161/STROKEAHA.111.631929

Wang, D.J.J., Chen, Y., Fernández-Seara, M.A., Detre, J.A., 2011. Potentials and challenges for arterial spin labeling in pharmacological magnetic resonance imaging. J. Pharmacol. Exp. Ther. https://doi.org/10.1124/jpet.110.172577

Wang, J., Aguirre, G.K., Kimberg, D.Y., Detre, J.A., 2003. Empirical analyses of null-hypothesis perfusion FMRI data at 1.5 and 4 T. Neuroimage 19, 1449–1462. https://doi.org/10.1016/S1053-8119(03)00255-6

Wang, J., Alsop, D.C., Li, L., Listerud, J., Gonzalez-At, J.B., Schnall, M.D., Detre, J.A., 2002. Comparison of quantitative perfusion imaging using arterial spin labeling at 1.5 and 4.0 Tesla. Magn. Reson. Med. 48, 242–254. https://doi.org/10.1002/mrm.10211

Wang, J., Wang, L., Zang, Y., Yang, H., Tang, H., Gong, Q., Chen, Z., Zhu, C., He, Y., 2009. Parcellation-dependent small-world brain functional networks: A resting-state fMRI study. Hum. Brain Mapp. 30, 1511–1523. https://doi.org/10.1002/hbm.20623

Wang, J., Zuo, X.N., He, Y., 2010. Graph-based network analysis of resting-state functional MRI. Front. Syst. Neurosci. 4, 16. https://doi.org/10.3389/fnsys.2010.00016

Warnock, G., Özbay, P.S., Kuhn, F.P., Nanz, D., Buck, A., Boss, A., Rossi, C., 2018. Reduction of BOLD interference in pseudo-continuous arterial spin labeling: towards quantitative fMRI. J. Cereb. Blood Flow Metab. 38, 847–856. https://doi.org/10.1177/0271678X17704785

Whitfield-Gabrieli, S., Nieto-Castanon, A., 2012. Conn : A Functional Connectivity Toolbox for Correlated and Anticorrelated Brain Networks. Brain Connect. 2, 125–141. https://doi.org/10.1089/brain.2012.0073

Williams, D.S., Grandis, D.J., Zhang, W., Koretsky, A.P., 1993. Magnetic resonance imaging of perfusion in the isolated rat heart using spin inversion of arterial water. Magn. Reson. Med. 30, 361–365. https://doi.org/10.1002/mrm.1910300314

Wolk, D., Detre, J., 2012. Arterial spin labeling MRI. Curr. Opin. Neurol. 25, 421–428. https://doi.org/10.1097/WCO.0b013e328354ff0a

Wong, E., 2005. Quantifying CBF with pulsed ASL: Technical and pulse sequence factors. J. Magn. Reson. Imaging 22, 727–731. https://doi.org/10.1002/jmri.20459

Wong, E., Buxton, R., Frank, L., 1997. Implementation of quantitative perfusion imaging techniques for functional brain mapping using pulsed arterial spin labeling. NMR Biomed. 10, 237–249. https://doi.org/10.1002/(SICI)1099-1492(199706/08)10:4/5<237::AID-NBM475>3.0.CO;2-X

Wong, E.C., Buxton, R.B., Frank, L.R., 1998. Quantitative imaging of perfusion using

a single subtraction (QUIPSS and QUIPSS II). Magn. Reson. Med. 39, 702–708. https://doi.org/10.1002/mrm.1910390506

Wu, B., Lou, X., Wu, X., Ma, L., 2014. Intra- and interscanner reliability and reproducibility of 3D whole-brain pseudo-continuous arterial spin-labeling MR perfusion at 3T. J. Magn. Reson. Imaging 39, 402–409. https://doi.org/10.1002/jmri.24175

Wu, C.W., Chen, C.L., Liu, po yu, Chao, Y.P., Biswal, B.B., Lin, C. po, 2011. Empirical Evaluations of Slice-Timing, Smoothing, and Normalization Effects in Seed-Based, Resting-State Functional Magnetic Resonance Imaging Analyses. Brain Connect. 1, 401–410. https://doi.org/10.1089/brain.2011.0018

Zalesky, A., Fornito, A., Bullmore, E., 2012. On the use of correlation as a measure of network connectivity. Neuroimage. https://doi.org/10.1016/j.neuroimage.2012.02.001

Zhang, K., Huang, D., Shah, J., 2018. Comparison of Resting-State Brain Activation Detected by BOLD, Blood Volume and Blood Flow. Front. Hum. Neurosci. 12, 1–10. https://doi.org/10.3389/fnhum.2018.00443

Zhang, N., Gordon, M., Goldberg, T., 2016. Cerebral blood flow measured by arterial spin labeling MRI at resting state in normal aging and Alzheimer's disease. Neurosci. Biobehav. Rev. 72, 168–175. https://doi.org/10.1016/j.neubiorev.2016.11.023

Zhang, N., Gordon, M.L., Goldberg, T.E., 2017. Cerebral blood flow measured by arterial spin labeling MRI at resting state in normal aging and Alzheimer's disease. Neurosci. Biobehav. Rev. 72, 168–175. https://doi.org/10.1016/j.neubiorev.2016.11.023

Zhou, J., Wilson, D.A., Ulatowski, J.A., Traystman, R.J., Van Zijl, P.C.M., 2001. Two-compartment exchange model for perfusion quantification using arterial spin tagging. J. Cereb. Blood Flow Metab. 21, 440–455. https://doi.org/10.1097/00004647-200104000-00013

Zhu, J., Zhuo, C., Qin, W., Xu, Y., Xu, L., Liu, X., Yu, C., 2015. Altered resting-state cerebral blood flow and its connectivity in schizophrenia. J. Psychiatr. Res. 63, 28–35. https://doi.org/10.1016/j.jpsychires.2015.03.002

Zhu, S., Fang, Z., Hu, S., Wang, Z., Rao, H., 2013. Resting State Brain Function Analysis Using Concurrent BOLD in ASL Perfusion fMRI. PLoS One 8, 4–12. https://doi.org/10.1371/journal.pone.0065884

Publications

INVESTIGATING AN OPTIMAL DURATION OF ACQUISITION IN RESTING-STATE ASL
Corentin Vallée, Pierre Maurel, Isabelle Corouge, Christian Barillot
OHBM 2019 – 25th Annual Meeting of the Organization for Human Brain Mapping, Jun 2019, Rome, Italy. pp.1-3

RESTING-STATE ASL : TOWARD AN OPTIMAL SEQUENCE DURATION
Corentin Vallée, Pierre Maurel, Isabelle Corouge, Christian Barillot
ISMRM 2018 – International Society for Magnetic Resonance in Medicine, Jun 2018, Paris, France. pp.1-2

ACQUISITION DURATION IN RESTING-STATE ARTERIAL SPIN LABELING. HOW LONG IS ENOUGH?
Corentin Vallée, Pierre Maurel, Isabelle Corouge, Christian Barillot
2019, submitted in Frontiers in neurosciences

UNIVERSITÉ DE RENNES 1

Titre : Arterial spin labeling performance in resting-state functional MRI: the effect of scan duration

Mots clés : Arterial spin labeling, resting-state functional MRI, scan duration

Résumé : L'arterial spin labeling en resting-state (rsASL) dans la routine clinique et la recherche universitaire reste confidentiel par rapport à l'état de repos BOLD. Cependant, contrairement au BOLD, l'ASL permet un accès direct au flux sanguin cérébral (CBF), ce qui pourrait conduire à une application clinique importante à l'échelle du sujet, car l'ASL est une mesure non invasive du CBF (suivi des maladies avec déficience du CBF, études longitudinales de sujets sains, etc.). Malgré l'implication croissante de tous les acteurs de l'IRM dans l'ASL au cours de la dernière décennie, la question de la durée d'acquisition (DA) en rsASL semble n'avoir jamais été abordée dans la littérature, malgré ses fortes conséquences pratiques (mise en œuvre clinique et maintien de l'état de repos du sujet) et son impact sur la représentation des réseaux fonctionnels. Dans cette thèse et comme travail préliminaire sur le sujet, nous discuterons tout d'abord de la manière d'étudier le rôle de la DA en rsASL avec des méthodes simples qui modélisent ce qu'un chercheur en rsMRI pourrait expérimenter. Nos résultats montrent que la représentation des réseaux fonctionnels se stabilise après une certaine durée d'acquisition pour des réseaux fonctionnels communs. Dans une deuxième partie, nous étudions les performance de l'ASL en resting-state par rapport au resting-state BOLD, tout en conservant la DA comme paramètre. Nous montrons que le rsBOLD surpasse la rsASL sur la plupart des aspects, mais pas sur tous. La possibilité de quantifier le CBF, contrairement au BOLD, tend à confirmer que le rsASL en particulier et l'ASL en général méritent encore plus d'implication de la part de la communauté de l'IRM fonctionnelle.

Title : Arterial spin labeling performance in resting-state functional MRI: the effect of scan duration

Keywords : Arterial spin labeling, resting-state functional MRI, scan duration

Abstract : Resting-state Arterial Spin Labeling (rsASL) in clinical routine and academic research remains confidential compared to resting-state BOLD. However, unlike BOLD, ASL provides with direct access to cerebral blood flow (CBF). This could lead to significant clinical subject scaled application as ASL is a non-invasive measurement of CBF (disease with CBF impairment follow-up, longitudinal studies of healthy subjects, etc.). Despite the significant increasing involvement of all MRI stakeholders is ASL over the past decade, the question of the acquisition duration (AD) in rsASL seems to have never been addressed in the literature, despite its strong practical consequences and its impact on functional networks representation. In this thesis, and as a preliminary work on the subject, we will first discuss how to study the role of AD in rsASL with simple methods that model what a researcher in rsMRI might experience. Our results show that the representation of functional networks stabilizes after a certain acquisition time for common functional networks. In a second part, we study the performance of the ASL in resting-state compared to the BOLD resting-state, while keeping the AD as a parameter. We show that the rsBOLD outperforms the rsASL on most aspects, but not on all. The ability to quantify the CBF, unlike the BOLD, tends to confirm that rsASL in particular and ASL in general deserve even more involvement from the functional MRI community.